AN ABSTRACT OF THE THESIS OF

Joseph G. Umhoefer for the degree of Doctor of Philosophy in Mathematics
presented on June 4, 2019.
Title: Modeling Flow and Transport at Pore Scale with Obstructions

Abstract approved: _____

Malgorzata S. Peszyńska

In this thesis we study mathematical and computational models for phenomena of flow and transport in porous media in the presence of changing pore scale geometries. The differential equations for the flow and transport models at Darcy scale involve the coefficients of permeability, porosity, and tortuosity which depend on the pore scale geometry. The models we propose help to understand how the presence of obstructions impacts the Darcy scale models. The particular changes in pore scale geometry we consider are due to the formation of obstructions to the flow, and come from two important applications of interest, biofilm clogging and gas hydrate crystal plugging up the pores. The direct simulations or experiments of these processes at pore scale is generally unfeasible or impractical.

We propose two computationally efficient mathematical and computational models to simulate the formation of the obstructions. The first method extends the phase separation model based on the Allen-Cahn equation; in our variant we add volume constraints and additional localization functions. The second method we propose is a Markov Chain Monte Carlo method inspired by the Ising model; here we use heuristics to choose the particular coefficients which guide the formation of obstructions of a particular type.

After we generate independent realizations of the obstructed geometries, we solve flow and transport problems at pore scale. Next we use the technique called upscaling which carries the information to larger scale by averaging, and we are able to derive the

ensemble of Darcy scale properties for a collection of generated pore scale geometries with obstructions. We show how these techniques can be used in synthetic geometries as well as in geometries obtained from imaging. In addition, we see that the permeability coefficient is not merely a function of porosity, but is rather highly dependent on the type of obstruction growing at the pore scale.

©Copyright by Joseph G. Umhoefer
June 4, 2019
All Rights Reserved

Modeling Flow and Transport at Pore Scale with Obstructions

by
Joseph G. Umhoefer

A THESIS

submitted to

Oregon State University

in partial fulfillment of
the requirements for the
degree of

Doctor of Philosophy

Presented June 4, 2019
Commencement June 2020

Doctor of Philosophy thesis of Joseph G. Umhoefer presented on June 4, 2019

APPROVED:

Major Professor, representing Mathematics

Head of the Department of Mathematics

Dean of the Graduate School

I understand that my thesis will become part of the permanent collection of Oregon State University libraries. My signature below authorizes release of my thesis to any reader upon request.

Joseph G. Umhoefer, Author

ACKNOWLEDGEMENTS

I must first thank my advisor, Dr. Małgorzata Peszyńska, whose patience, support, and guidance made this work possible. I would also like to thank my committee members, Dr. Robert Higdon, Dr. Adel Faridani, Dr. Ralph Showalter, and Dr. Henri Jansen. Thank you also to those who served on my committee prior to the final defense, Dr. Lech Muszynski, Dr. Eugene Zhang, and Dr. Juan Restrepo. My committee provided invaluable feedback throughout my graduate education.

I am much obliged to my collaborator Dr. Timothy Costa, who provided advice, support and grounding conversation.

I am indebted to all of my friends within the OSU math community, who added much needed levity to my graduate experience, with special recognition for Dr. Naveen Somasunderam, Dr. Charlie Robson and Dr. Duncan McGregor.

Thank you to my mentors at Lawrence Berkeley National Laboratory, Dr. Hans Johansen and Dr. Dan Martin, who provided tremendous encouragement and support.

Thank you to Solid Modeling Solutions for providing new opportunities, challenges and advice. In particular, thank you to Jim Presti, Dr. George Celniker, Dr. Bill Denker, and Steve Teodosiadis.

The research in this work was partially funded by the National Science Foundation (NSF) as part of two projects. First, project NSF DMS-1522734 "Phase transitions in porous media across multiple scales," (Principal Investigator Malgorzata Peszynska). Second, project NSF DMS-1738014, 2017 "APG: Improve STEM graduate student preparedness for workforce (Internship at LNBL for Joe Umhoefer)," (Principal Investigator Malgorzata Peszynska).

I would also like to acknowledge the lifetime of love and support I've received from my family. From my parents, Chuck and Jackie Umhoefer, from my siblings Charlie (Casey) Umhoefer, Julia (Erik) Schmidt, and Michael Umhoefer, and all of my wonderful nephews and niece.

Finally, thank you to Erin Mitchell for your love and fighting so hard for us all to succeed. And to Finten Umhoefer, to whom this work is dedicated.

TABLE OF CONTENTS

TABLE OF CONTENTS (Continued)

Page

TABLE OF CONTENTS (Continued)

Page

TABLE OF CONTENTS (Continued)

Page

LIST OF FIGURES

LIST OF FIGURES (Continued)

Figure | Page

LIST OF FIGURES (Continued)

Figure Page

Figure Page

For Finten Ian Michael Umhoefer

Modeling Flow and Transport at Pore Scale with Obstructions

1 Introduction

In this thesis we explore mathematical and computational models for phenomena of flow and transport in porous media. In particular, we study how the flow and transport properties change as the porous media geometry changes due to the formation of obstructions to the flow at the pore scale resulting, e.g.. from chemical reactions. Our main objective is to propose computationally efficient tunable mathematical and computational models which support the understanding of these processes across the different length scales.

Porous media. A porous medium is an aggregate of solids, a domain of solid grains and void spaces. The solid grains may be organic, such as particles of skin, agglomerates of flour in bread, bone cells in bone, or rock particles in soils. The grains can be rigid or flexible, and the entire solid skeleton can be considered as rigid or elastic. In this thesis we only consider rigid porous media in which the position of the porous medium skeleton is fixed. In addition, in this thesis we consider only porous media in which the void space is connected, so that some fluid may flow through the medium.

The applications which involve porous media are as diverse as porous media itself, from pharmaceutical delivery in the body to subsurface engineering. Our work focuses on applications in the subsurface. By subsurface, we refer to the porous media below the surface of the earth. The porous media in this regime include aquifers, soils, and oil reservoirs.

The models used to describe flow and transport are dependent on the scale of the problem considered. In this dissertation we consider the pore scale of μm length scale and Darcy scale appropriate at the $cm - m - km$ scales. At the pore scale we recognize

individual grains and the viscous fluid flow which moves in the void space between the grains. At Darcy scale we consider average quantities, where we do not distinguish individual grains and channels of flow, but rather how fluid moves through the porous medium in aggregate. The challenge addressed in this thesis is to model the flow and transport at these two scales and to connect these models together.

Pore scale geometry with obstructions. Darcy scale properties of a porous media, such as permeability, porosity and tortuosity, are highly dependent on the pore scale geometry. We are particularly interested in phenomena which involve clogging of pores due to reactive transport and phase transitions. In particular, we are interested in applications which involve biofilm growth such as in Microbial Enhanced Oil Recovery (MEOR), or the growth of hydrate crystals at the pore scale [56, 10].

As the pore scale geometry changes, so do the aforementioned Darcy scale properties. The pore scale geometry may change due to chemical processes, such as precipitation or dissolution, or biological processes, such as biofilm growth. Changing geometries in particular are crucial to biological clogging of soils [49], methane hydrate formation [10], biocementation [17] and contaminant transport [5].

There are many approaches to finding how the porous media properties change when the geometry changes due to chemical processes. We review these methods below.

(A) First, one can study the problem experimentally, and measure the properties while subjecting the medium to some given chemical process.

(B) Second, one can design an experiment and image the media while the process is ongoing; this provides the measures of the Darcy scale properties properties accompanied by the detailed information about the geometry.

(C) Third, one can study the problem using computations, and conduct direct numerical simulation (DNS) of the process at the pore scale, accompanied by upscaling of the properties to Darcy scale. Such simulations can be carried out using first principle physical models, such at those involving advection, diffusion, and reaction.

Overview of the models proposed in this thesis. In this work we propose the fourth approach (D) of generating multiple realizations of the process using computation

simulations which are not based on first principles. Yet we generate geometries similar to those found by x-ray imaging. The advantage of our approach is that it is fast and does not require calibration or exact coefficients. We propose two methods for generating physically realistic pore scale obstruction in porous media.

One of the advantages of our methods is that they are computationally cheap and easy to run. The methods are designed to quickly find a realistic obstruction representation starting from some initial random configuration. By running them multiple times, we find as many independent realizations as desired.

Furthermore, each of the two methods proposed has a few parameters that can be tuned to account for different obstruction characteristics. Currently, the parameters are set by hand based on heuristics. For example, hydrate crystals seem to "avoid" the solid matrix as seen in the experiments in [56]. Biofilms on the other hand "cling" to the solid matrix as seen in [35]. The methods we propose can easily reproduce these different behaviors.

Last but not least, our models can be iteratively coupled with a flow solver to model how flow changes as hydrates or biofilm aggregate.

We complete several experiments to infer how porous media properties are impacted by geometry changes. By completing these experiments for multiple types of obstructions we see that the permeability is highly dependent on the type of obstruction growing at the pore scale. In particular, we confirm that the permeability is not merely a function of porosity, but is rather highly dependent on how the geometry is changing.

Outline. This work is organized as follows. In Chapter 2 we discuss the mathematical preliminary topics necessary to develop the rest of the thesis. In Chapter 3 we discuss the fundamentals of flow and transport in porous media. This chapter includes a description of models for flow and transport at both pore scale and at Darcy scale. We also include methods for upscaling, the process used to take information from the pore scale to the Darcy scale. Lastly, this chapter describes the numerical methods used to solve flow and transport at pore and Darcy scales, as well as our numerical schemes

for deriving the Darcy scale quantities porosity, permeability and tortuosity.

In Chapter 4 we provide context for our methodology of creating obstructions. We review other current methods for studying changing pore scale geometry. We describe two particular obstructions of interest, those that are pore coating and those that are pore filling. Lastly, we introduce some background material for our Constrained Localized Phase Separation (CLPS) Model.

In Chapter 5 we discuss the first model for generating pore scale obstructions, the CLPS model. This method is an extension of a phase separation model based on the Allen-Cahn equation subject to constraints. This method finds local minima of a functional which is not convex, subject to constraints. These minimizers are reached from different initial conditions. We describe how we find the local minima and discuss adding constraints to minimization problems using linear examples. We then describe how the process works with nonlinear equations and tie the pieces together to describe our method.

In Chapter 6 we discuss the second model for generating pore scale obstructions. This method is a Markov chain Monte Carlo method inspired by the Ising model, which we call the Lattice model. This method is probabilistic and is well known to generate multiple final states. We begin by providing an overview of MCMC methods in general. We next describe the Ising model. Lastly, we describe the Lattice model and provide a few examples.

In Chapter 7 we collect the main results of this thesis. The results we present are from a number of experiments, where we describe (1) permeability distributions in single pore domains, (2) permeability against pore scale breakthrough in many pore domains, (3) tortuosity distributions in many pore domains generated with phase separation simulations and (4) breakthrough curves at pore scale against breakthrough curves at Darcy scale.

2 Preliminaries

In this section we introduce the background mathematical material necessary for the development of our ideas. We begin with notation for basic concepts in Section 2.1. In Section 2.2 we move to intermediate topics, providing definitions and examples. In Section 2.3 we describe one way to constrain minimization problems. In Section 2.4 we describe some of the numerical schemes used.

Many derivations in this thesis will be done with unit coefficients. However, example problems will include constant coefficients that do not meaningfully change the derivations, but add interesting behavior to the examples.

2.1 Notation

Let $D \subsetneq \mathbb{R}^d$, $d = 1, 2, 3$ be an open, bounded, connected domain with boundary ∂D. Denote $x \in \mathbb{R}^d$ as $x = (x_1, \ldots, x_d)$. For elements $x \in D$, we do not distinguish with vector notation between the cases where $d = 1$ and $d = 2, 3$.

Let $D_A,\ D_B \subseteq D$ be open subsets of D. We denote the interface of D_A and D_B as $\Gamma_{A,B} = \partial D_A \cap \partial D_B$. We also let $D_{A,B} = D_A \cup D_B \cup \Gamma_{A,B}$.

Let $f : D \to \mathbb{R}$. For $d = 1$ we may denote continuous derivatives of $f(x)$ as any of the following

$$\frac{df}{dx},\ f_x,\ f_x(x).$$

For $d = 2$ or $d = 3$, we may denote the partial derivatives of f in the direction of x as any of the following

$$\frac{\partial f}{\partial x},\ \partial_x f,\ f_x,\ f_x(x).$$

Context should make clear whether f_x refers to a derivative or partial derivative. Let d-tuple $\alpha \in \mathbb{N}^d$, $\alpha = (\alpha_1, \ldots, \alpha_d)$. For $d = 2$, we denote the partial derivative of order $|\alpha| = \alpha_1 + \alpha_2$ as D^α,

$$D^\alpha = \frac{\partial^{|\alpha|}}{\partial x^{\alpha_1} \partial y^{\alpha_2}}.$$

This extends in the usual way when $d = 3$.

For the gradient operator acting on f when $d = 2$, we may use any of the following

$$\nabla f,\ \nabla_x f,\ \nabla_{x,y} f,\ \ (\partial_x f, \partial_y f)\,.$$

We extend the operator in the usual way when $d = 3$, and restrict the operator in the usual way when $d = 1$.

We denote the gradient in the normal direction along a boundary of a set as the following

$$\frac{\partial f}{\partial n} = \nabla_x f \cdot n.$$

Let $f : D \times \mathbb{R} \to \mathbb{R}$, $f(x, \lambda)$ where $x \in D$, $\lambda \in \mathbb{R}$. For $d = 2$, we denote as follows,

$$\nabla_{x,\lambda} f := (\partial_x f, \partial_y f, \partial_\lambda f)\,.$$

For $d = 3$, we extend $\nabla_{x,\lambda}$ in the usual way.

Let $\mathbb{1}_{\mathbb{A}}$ be the characteristic function of the set A,

$$\mathbb{1}_A(x) = \begin{cases} 1, & x \in A, \\ 0, & x \notin A. \end{cases} \tag{2.1.1}$$

For a volume $V(x) \subseteq D$ centered at $x \in D$, we denote the average of a function q over $V(x)$ as

$$\langle q \rangle_V \equiv \langle q \rangle(x) \equiv \frac{1}{|V(x)|} \int_{V(x)} q(y)\ dy. \tag{2.1.2}$$

2.2 Background material

2.2.1 Function Spaces

Let $K \subset \mathbb{R}^d$. Then, $K \subset\subset D$ means that K is a compact subset of the open $D \subset \mathbb{R}^d$.

Define the space of continuous $f : D \to \mathbb{R}$ as $C(D)$. Define the space of continuous functions on D with continuous derivatives up to order $p \geq 0$ as $C^p(D)$,

$$C^p(D) = \{f \in C(D) : D^\alpha f \in C(D),\ \forall \alpha,\ |\alpha| < p\}\,,$$

and

$$C^\infty(D) = \bigcap_{p\geq 1} C^p(D).$$

We denote the space of continuous functions on D with compact support as $C_0(D)$,

$$C_0(D) = \{f \in C(D) : \text{supp}(f) \text{ is compact}\}.$$

We also define the sets

$$C_0^p(D) = C^p(D) \cap C_0(D), \text{ and } C_0^\infty = C^\infty(D) \cap C_0(D).$$

Define the usual L^p norm

$$||f||_{L^p(D)} = \left(\int_D |f|^p\right)^{1/p}.$$

In general, if no specific norm is specified, the L^2 norm is implied, i.e.,

$$||\cdot|| = ||\cdot||_{L^2(D)}$$

We use the Lebesgue spaces, $L^p(D)$, defined as

$$L^p(D) = \left\{f : ||f||_{L^p(D)} < \infty\right\}.$$

Definition 2.2.1 (Weak derivative)**.** Let $f \in L^2(D)$ and $\alpha \in \mathbb{N}^d$. The weak derivative, $\partial^\alpha f$, of f of order $|\alpha|$ is a function in $L^2(D)$ such that

$$\int_D \partial^\alpha f \phi = (-1)^{|\alpha|} \int_D f \partial^\alpha \phi, \ \forall \phi \in C_0^\infty.$$

Example 2.2.1. Let $D = (-1, 1)$, and $f : D \to \mathbb{R}$, $f(x) = |x|$. In this case f is not classically differentiable at $x = 0$. We calculate the weak derivative by finding $\frac{\partial f}{\partial x}$ such that

$$\int_{-1}^1 f\phi_x = -\int_{-1}^1 \frac{\partial f}{\partial x}\phi, \ \forall \phi \in C_0^\infty(0,1).$$

Observe,

$$\begin{aligned}\int_{-1}^1 |x|\phi_x &= \int_{-1}^0 -x\phi_x + \int_0^1 x\phi_x \\ &= -x\phi\big|_{-1}^0 + \int_{-1}^0 \frac{\partial x}{\partial x}\phi + x\phi\big|_0^1 - \int_0^1 \frac{\partial x}{\partial x}\phi = \int_{-1}^0 \phi - \int_0^1 \phi.\end{aligned}$$

So the weak derivative of f is the piece-wise function

$$\frac{\partial f}{\partial x} = \begin{cases} -1, & x < 0, \\ \alpha, & x = 0, \\ 1, & x > 0. \end{cases}$$

We recall that it does not matter what value α takes, when $\frac{\partial f}{\partial x}$ is considered a representative of an equivalence class of functions in L^2.

In what follows we do no distinguish between the classical derivative and the weak derivative. When the classical derivative exists, it is equivalent to the weak derivative.

Let $k \in \mathbb{N}$. Define the Sobolev space $H^k(D)$ as follows

$$H^k(D) = \left\{ f \in L^2(D) : \partial^\alpha f \in L^2(D), |\alpha| \leq k \right\}.$$

We define $H_0^k(D)$ to be the closure in $H^k(D)$ of $C_0^\infty(D)$.

Let $f, g \in L^2(D)$. Define the L^2 inner product as follows

$$(f, g)_{L^2(D)} = \int_D fg.$$

We will often refer to this inner product without the subscript, i.e.,

$$(f, g) = (f, g)_{L^2(D)}.$$

For the following two examples, let $D = (-1, 1)$ and $f : D \to \mathbb{R}$. Let $u : D \to \mathbb{R}$. Let $V \subseteq L^2(D)$ and $f : V \to \mathbb{R}$. For the next two examples, we consider the differential equation

$$-u_{xx} = f, x \in (-1, 1) \tag{2.2.1}$$

where we vary $f \in V$ between examples, so that u is either a classical or weak solution to (2.2.1). For both examples we impose homogeneous Dirichlet boundary conditions.

Example 2.2.2. Let $f(x) = 1$, so $f \in C^0(-1, 1)$. Then

$$-u_{xx} = 1, \ x \in (-1, 1).$$

The classical solution $u \in C^2(-1,1)$ to (2.2.1) is

$$u(x) = \frac{1}{2}(x+1)(1-x).$$

Example 2.2.3. Define $f(x)$ as follows

$$f(x) = \begin{cases} 1, & x \in (-1,0), \\ -1, & x \in (0,1), \end{cases}$$

so $f \in L^2(-1,1)$. Then the solution $u(x) \in H^2(-1,1)$ to (2.2.1) is

$$u(x) = \begin{cases} -\frac{1}{2}x(x+1), & x \in (-1,0), \\ \frac{1}{2}x(x-1), & x \in (0,1). \end{cases}$$

Note in particular that while $u \in H^2(-1,1)$, we have that $u \notin C^2(-1,1)$, but $u \in C^1(-1,1)$.

2.2.2 Gâteaux derivative and notation for the derivative of functionals

Definition 2.2.2 (Gâteaux derivative)**.** Let V be a Hilbert space and $J : V \to \mathbb{R}$. For $\psi, \phi \in V$, the Gâteaux derivative of J at ψ in the direction of ϕ is defined as follows,

$$\frac{\delta J}{\delta \psi}(\phi) = \frac{d}{dt} J(\psi + t\phi)|_{t=0} = \lim_{t \to 0} \frac{J(\psi + t\phi) - J(\psi)}{t}.$$

This derivative is also known as the first variation of J at ψ in the direction of ϕ.

Other common notation for the Gâteaux derivative includes $\delta J(\psi)\phi$, used in [21] and $J'(\psi)(\phi)$, used in [48]. In some other literature the notation $\langle J'(\psi), \phi \rangle$ is used to emphasize the duality pairing between the linear functional $J'(\psi)$, and its argument ϕ. In turn, in computational physics it is common to use the symbol $\nabla J(\psi)(\phi)$ or $\nabla_\psi J(\phi)$.

By the Riesz representation theorem [48, Ch.1] we have for $\frac{\delta J}{\delta \psi} \in V'$ that we can find some representer $g \in V$ of this functional, which is unique,

$$\frac{\delta J}{\delta \psi}(\phi) = (g, \psi)\,, \ \forall \phi \in V. \tag{2.2.2}$$

In what follows we do not distinguish between the operator $\frac{\delta J}{\delta \psi} \in V'$ and the unique element $g \in V$.

We provide now some examples of $\frac{\delta J}{\delta \psi}(\psi)(\phi)$ which are relevant to our model development below.

Example 2.2.4. Let $J(\psi) = \int_0^1 f(x)\psi(x)dx$ where $f, \psi \in L^2(0,1)$. Then $\frac{\delta J}{\delta \psi}(\phi) = \int_0^1 f(x)\phi(x)dx$. One could identify $\frac{\delta J}{\delta \psi}$ with f for any ψ. In other words, $\frac{\delta J}{\delta \psi}$ is constant.

Example 2.2.5. Let $J(\psi) = \int_0^1 f(x)\psi^2(x)dx$. Then $\frac{\delta J}{\delta \psi}(\phi) = \int_0^1 2f(x)\psi(x)\phi(x)dx$. One can identify $\frac{\delta J}{\delta \psi}$ with $2f\psi$. Here $\frac{\delta J}{\delta \psi}$ is not constant.

Example 2.2.6. Let $J(\psi) = \int_0^1 f(\psi(x))dx$. Then $\frac{\delta J}{\delta \psi}(\phi) = \int_0^1 \frac{df}{d\psi}(\psi(x))\phi(x)dx$, and we must assume that $\frac{df}{d\psi} \in L^2(0,1)$. One can identify $\frac{\delta J}{\delta \psi}$ with $\frac{df}{d\psi}$.

Example 2.2.7. Let $J(\psi) = \int_0^1 f(x, \psi(x))dx$. Then $\frac{\delta J}{\delta \psi}(\phi) = \int_0^1 \frac{\partial f}{\partial \psi}(x, \psi(x))\phi(x)dx$. One can identify $\frac{\delta J}{\delta \psi}$ with $\frac{\partial f}{\partial \psi}(x, \psi(x))$. Here we must assume that $\frac{\partial f}{\partial \psi} \in L^2(0,1)$.

In what follows we will use notation

$$\left(\frac{\delta J}{\delta \psi}, \phi\right) = \frac{\delta J}{\delta \psi}(\psi)(\phi). \tag{2.2.3}$$

This choice will avoid the clash with the notation $\langle \cdot, \cdot \rangle$ commonly used for the averages, and will avoid multiple parentheses needed present in $\frac{\delta J}{\delta \psi}(\psi)(\phi)$ when we need to emphasize the dependence of $\frac{\delta J}{\delta \psi}$ on ψ. Even though $(\cdot, \cdot)$ also means an inner product on $L^2(D)$, we find the notation we suggest more intuitive.

The first variation is commonly used to find critical points of functionals. In particular, it is used in the Euler-Lagrange equations in variational calculus. We discuss this below.

2.2.3 Minimization problems, variational formulation, and differential equations

Minimization problems can often be posed as differential equations. By changing the problem formulation new opportunities for solving the problem can be found. In particular, transforming a minimization problem into a differential equation allows, e.g.

finite difference methods to be employed to find approximations. In this section we present some basic examples of how to formulate minimization problems as differential equations and under what conditions the solutions satisfy both the differential equations and the minimization problems. We follow [21, Ch. 11] and [20].

Let D be a bounded, open region in $\mathbb{R}^d$, $d = 1, 2$ or 3. Let $V \subseteq H^1(D)$ and $f \in L^2(D)$. We define the bilinear form $a(\cdot, \cdot)$ and the linear functional $F(\cdot)$ as follows

$$a(\psi, \phi) := \int_D \nabla\psi \cdot \nabla\phi, \qquad\qquad F(\phi) := \int_D f\phi.$$

We also let the quadratic functional A be defined as follows

$$A(\phi) = \frac{1}{2}a(\phi, \phi),$$

and we define the functional $J : V \to \mathbb{R}$,

$$J(\phi) = \frac{1}{2}a(\phi, \phi) - F(\phi). \tag{2.2.4}$$

We are interested in finding the minimizer, $\psi \in V$ of $J(\phi)$,

$$\psi = \arg\min_{\phi \in V} J(\phi).$$

When the minimizer ψ exists, we have

$$J(\psi) \leq J(\phi), \ \forall \phi \in V.$$

Write $\phi = \psi + t\rho \in V$, for $t \in \mathbb{R}$ and $\rho \in V$. If ψ is the minimizer, we have that $J(\psi + t\rho)$ has a minimum at $t = 0$ characterized by

$$\left(\frac{\delta J}{\delta \psi}, \rho\right) = 0, \ \forall \rho \in V. \tag{2.2.5}$$

Equivalently, we have that the minimizer ψ satisfies the problem

$$\text{Find } \psi \in V, \text{ such that } a(\psi, \rho) = (f, \rho), \ \forall \rho \in V. \tag{2.2.6}$$

In turn, if the solution ψ to (2.2.6) is smooth enough, then ψ satisfies an associated PDE which we find by integration by parts.

Example 2.2.8. Minimization with Dirichlet boundary conditions

Let $V = H_0^1(D)$ and assume that the solution ψ to (2.2.6) or, equivalently, the minimizer of $J(\phi)$ defined by (2.2.4), is sufficiently smooth. Then ψ satisfies the PDE

$$\begin{cases} -\Delta\psi(x) - f(x) = 0, & x \in D, \quad (2.2.7a) \\ \psi(x) = 0, & x \in \partial D. \quad (2.2.7b) \end{cases}$$

See [21, Ch. 8] for details on the well-posedness of (2.2.7). In general, the discussion of solvability of problems is outside the scope of this work. However, it is well known that the functional J for the Dirichlet problem is strictly convex. It is also bounded from below because $a(u,u) \geq C||u^2||$ which overpowers the linear term $-\int_D fu$. Thus there is a unique minimizer ψ, the solution to the variational problem (2.2.6).

A general statement on the well-posedness of (2.2.6) when the form $a(\cdot,\cdot)$ is not symmetric, and there is no associated minimization principle, is provided by the Lax-Milgram Theorem [47].

Example 2.2.9. Minimization with Neumann boundary conditions

Suppose now that $V = H^1(D)$ and assume that for (2.2.6) the solution ψ is sufficiently smooth. Then ψ satisfies the PDE

$$\begin{cases} -\Delta\psi(x) - f(x) = 0, & x \in D, \quad (2.2.8a) \\ \dfrac{\partial\psi}{\partial n}(x) = 0, & x \in \partial D. \quad (2.2.8b) \end{cases}$$

The solution to the Neumann problem is not unique. This is because the functional J on V is not strictly convex. There exist many minimizers of J, any two of which differ by a constant. In addition, in (2.2.8) it must be that $\int_D f = 0$ for there to exist a solution ψ. This is required in order for the functional $J(\cdot)$ to be bounded from below. If f is arbitrary and u is any constant, then the term $-\int_D fu$ is not bounded from below.

To see why the condition $\int_D f = 0$ is needed from the form of the PDE (2.2.8), we integrate (2.2.8a),

$$\int_D f = a(\psi, 1) = 0. \quad (2.2.9)$$

We come back to these two examples several times in what follows.

2.3 Lagrange Multipliers for constrained minimization problems

In this section we introduce concepts from [40]. The authors consider constrained optimization problems of some real-valued or possibly extended-real-valued function, f_0. They consider a broad class of constraints including real valued equality constraints, $f_i = 0$, and inequality constraints, $f_i \leq 0$. Let $G \subset \mathbb{R}^n$. Then a standard formulation of optimization is to

$$\begin{aligned} &\text{minimize } f_0(x) \text{ over all } x \in G, \\ &\text{such that } f_i(x) \begin{cases} \leq 0, & i = 1, \ldots, s, \\ = 0, & i = s+1, \ldots, m. \end{cases} \end{aligned} \tag{2.3.1}$$

For this work, we are interested in how the authors use Lagrange multipliers to enforce equality constraints. The Lagrangian for problem (2.3.1) is the function $L : G \times \mathbb{R}^m \to \mathbb{R}$ defined by

$$L(x, y) = f_0(x) + y_1 f_1(x) + \cdots + y_m f_m(x), \quad y = (y_1, \ldots, y_m). \tag{2.3.2}$$

Theorem 2.3.1 (2.2, [40])**.** Consider problem (2.3.1) with equality and inequality constraints present. If x is a locally optimal solution at which the gradients $\nabla f_i(x)$ of the equality constraint functions and the active inequality constraint functions are linearly independent, then there must be a vector y in

$$Y = \{y = (y_1, \ldots, y_s, y_{s+1}, \ldots, y_m) : y_i \geq 0 \text{ for } i = 1 \ldots, s\}$$

such that

$$\nabla_x L(x, y) = 0, \tag{2.3.3a}$$

$$\frac{\partial L}{\partial y_i}(x, y) \quad \begin{cases} = 0 & \text{for } i \in [1, s] \text{ with } y > 0, \text{ and for } i \in [s+1, m], \\ \leq 0 & \text{for } i \in [1, s] \text{ with } y = 0. \end{cases} \tag{2.3.3b}$$

The components of y are called Lagrange multipliers. The first-order optimality conditions in the theorem are known as the Karush–Kuhn–Tucker conditions.

We apply these technique next to the minimization problems described in Section 2.2.3 in which we introduce some constraints on the solution.

2.3.1 Using Lagrange multipliers for boundary value problems

Now we apply the technique of Lagrange multipliers described above to solve the minimization problem under constraints. We consider again the functional $J(\cdot)$ defined by (2.2.4). We proceed without developing the abstract framework.

Let $k \in \mathbb{R}$ be given. We want to minimize $J(\cdot)$ defined by (2.2.4) over $K = \{v \in V : \int_D v = k\}$. Let $V = H_0^1(D)$. We note that K is a closed convex set. Let also $f \in L^2(D)$ be given.

The solution to this constrained minimization problem is formulated with the Lagrange multiplier λ as follows. We first formulate the Lagrangian

$$L(u, \lambda) = J(u) - \lambda(\int_D u - k), \tag{2.3.4}$$

then calculate the first order optimality conditions similar to (2.3.3),

$$\begin{cases} \dfrac{\delta L}{\delta u} = 0, & \text{(2.3.5a)} \\ \dfrac{\delta L}{\delta \lambda} = 0. & \text{(2.3.5b)} \end{cases}$$

Find solutions (u, λ) that satisfy (2.3.5).

Example 2.3.1. We seek $u \in H_0^1(D)$ and $\lambda \in \mathbb{R}$ which satisfy the first order optimality conditions for $J(\cdot)$ under the single constraint expressed in the definition of K.

$$\begin{cases} -\Delta u(x) - \lambda = f(x), \qquad x \in D, & \text{(2.3.6a)} \\ \displaystyle\int_D u(x) = k, & \text{(2.3.6b)} \\ u|_{\partial D} = 0. & \text{(2.3.6c)} \end{cases}$$

We do not provide rigorous analysis of this problem but note that we formulate the PDE (2.3.6) by integration by parts.

We discuss the numerical approximation and remark on the solvability of the discrete problem in Example 2.4.2.

Example 2.3.2. Now let $V = H^1(D)$ and find $u \in H^1(D)$ and $\lambda \in \mathbb{R}$ as in the previous

example.

$$\begin{cases} -\Delta u(x) - \lambda = f(x), & x \in D, \quad (2.3.7a) \\ \int_D u(x) = k, & (2.3.7b) \\ \dfrac{\partial u}{\partial n}(x) = 0, & x \in \partial D. \quad (2.3.7c) \end{cases}$$

This example should be compared to Example 2.2.9.

Note that (2.3.7) is (2.2.8) with constraints. We remind the reader that solutions to (2.2.8) are unique only up to constants and any solution requires that $\int_D f = 0$. However, the solvability of (2.3.7) is not limited by $\int_D f$. We also have uniqueness of solutions. Observe that by integrating (2.3.7a) we get

$$\lambda = -\frac{1}{|D|}\int_D f,$$

so the solution λ is the average value of f, i.e., the function $f + \lambda$ automatically satisfies that $\int_D f + \lambda = 0$. In turn, by (2.3.7b) ensures uniqueness of the solution u. Should u vary by a constant as in solutions to (2.2.8), then the constraint (2.3.7b) would be violated.

The discussion above on existence and uniqueness of solutions for the linear problems under constraints in Examples 2.3.1 and 2.3.2 does not carry over to the case when $f = f(u)$. This is discussed in Sections 4.2.1 when we discussed our proposed model.

2.4 Numerical solution to differential equations

In this section we introduce some of the numerical schemes used in this work. These methods include a standard finite difference scheme for boundary value problems in one dimension and a cell centered finite difference scheme for the Poisson equation in two dimensions. We also discuss the backward Euler method for time stepping and the Implicit-Explicit scheme used for solving time-dependent nonlinear equations.

Many of the examples in this work are solved with second order accurate methods. One can, of course, develop higher order methods or employ strategies, such as adaptive

mesh refinement, to improve the accuracy of the results. However, our focus is on the development of the model and being able to compute numerical solutions quickly.

In Sections 2.4.1 and 2.4.3 we describe the finite difference schemes used in the one dimensional examples. In Section 2.4.2 we describe the cell centered finite difference scheme used to solve Poisson's equation. In Section 2.4.4 we describe the numerical scheme used to generate obstructions in porous media via phase separation.

Solving elliptic or parabolic boundary value problems with finite differences usually involves solving a linear system. In this thesis we do not address the linear solvers directly. In particular, we do not employ any special linear solvers beside the usual "backslash operator". In fact, the numerical solutions in Section 4.2.1 are calculated with Matlab.

2.4.1 Numerical schemes for equilibrium examples with $d = 1$

To compute solutions to example problems in one dimension, we will use a standard Finite Difference scheme. Here we assume that the solution to the underlying differential equation exists and is smooth enough so that the Finite Difference method converges at an optimal rate. In particular, this might require C^4 smoothness of the solution. We follow [26].

Let the domain $D = (0, 1)$. We use uniform step size $h = 1/M$, and $M + 1$ points. We will use $M = 1000$. Discretize the domain by $x_i := ih$, for $i = 0, \ldots, M$.

Let $u : D \to \mathbb{R}$ be any function. We denote the pointwise approximations of u as

$$u_i \approx u(x_i).$$

To denote vectors of approximations $u_i,\ i = 1, \ldots, M - 1$, we use capital, blackboard bold font,

$$\mathbb{U}^T = \begin{bmatrix} u_1 & u_2 & \cdots & u_{M-1} \end{bmatrix}.$$

In the case where the function is denoted by a Greek letter, we use the capital Greek letter. We use the `norm` function in Matlab, which calculates the l^2 norm,

$$||\mathbb{U}||_{l^2} = \left(\sum_{i=1}^{M-1} u_i^2 \right)^{1/2}.$$

We denote a vector of units as

$$\mathbb{1}^T = \begin{bmatrix} 1 & 1 & \cdots & 1 \end{bmatrix}.$$

Example 2.4.1. Suppose we want to approximate the solution to (2.2.7) in one dimension. We solve

$$A\mathbb{U} = \mathbb{F},$$

where the operator A is defined with the standard centered difference for the Finite Difference approximation. When solving for the interior values, the boundary conditions for the problem are encoded in the matrix A. With homogeneous Dirichlet boundary conditions we have

$$A = \frac{1}{h^2}\begin{bmatrix} 2 & -1 & & & \\ -1 & 2 & -1 & & \\ & \ddots & \ddots & \ddots & \\ & & -1 & 2 & -1 \\ & & & -1 & 2 \end{bmatrix} \approx -\frac{d^2}{dx^2}.$$

In this case, the matrix A is symmetric positive definite (SPD) [26]. A symmetric matrix $M \in \mathbb{R}^{nxn}$ is *positive definite* if

$$u^T M u > 0, \quad \text{for all } u \in \mathbb{R}^n \backslash 0. \tag{2.4.1}$$

To approximate Neumann boundary conditions as in (2.2.8b) we use a first order, one-sided approximation

$$u_x(0) \approx \frac{1}{h}\left(u_1 - u_0\right).$$

In this case we must also solve for the boundary values u_0 and u_M. The matrix A and the right hand side are modified, with A as follows

$$A = \frac{1}{h^2}\begin{bmatrix} 1 & -1 & & & \\ -1 & 2 & -1 & & \\ & \ddots & \ddots & \ddots & \\ & & -1 & 2 & -1 \\ & & & -1 & 1 \end{bmatrix} \approx -\frac{d^2}{dx^2}.$$

Here, the matrix A is symmetric non-negative definite (SND). A symmetric matrix $M \in \mathbb{R}^{nxn}$ is *non-negative definite* if

$$u^T M u \geq 0, \quad \text{for all } u \in \mathbb{R}^n. \tag{2.4.2}$$

It is well known that this Finite Difference scheme converges with the order $O(h^2)$ as long as the solution $u(x)$ is C^4 smooth [26]. Following [26] one can easily extend this method to 2D.

Example 2.4.2. Let $\lambda \in \mathbb{R}$, u be a smooth solution of the constrained minimization problem from Example 2.3.1. Suppose we are interested in approximating the solutions to the system of equations

$$\begin{cases} -u_{xx}(x) - \lambda = f(x), & x \in (0,1), \\ \int_0^1 u(x)dx = k, \\ u(0) = u(1) = 0. \end{cases}$$

where $k \in \mathbb{R}$.

We approximate its solution similarly to that above. The new element is that we have to discretize the second equation with an integral. To approximate integrals over D, we use the trapezoidal method,

$$\int_D u(x) \approx \frac{h}{2}u_0 + \sum_{i=1}^{M-1} hu_i + \frac{h}{2}u_m.$$

To find the approximations $\mathbb{U}$ and λ we solve the saddle point system

$$\begin{bmatrix} A & -\mathbb{1} \\ \mathbb{1}^T & 0 \end{bmatrix} \begin{bmatrix} \mathbb{U} \\ \lambda \end{bmatrix} = \begin{bmatrix} \mathbb{F} \\ k/h \end{bmatrix}.$$

The solution $[\mathbb{U}, \lambda]^T$ to this linear system can be shown to exist and be unique. Since this system is square, existence is equivalent to uniqueness. To show uniqueness, we consider $M[\mathbb{U}, \lambda]^T = 0$ where M is the matrix

$$M = \begin{bmatrix} A & -\mathbb{1} \\ \mathbb{1}^T & 0 \end{bmatrix}.$$

From the inner product $(M[\mathbb{U},\lambda]^T,[\mathbb{U},\lambda]^T)=0$ we get the system of equations

$$(A\mathbb{U},\mathbb{U})-(\lambda\mathbb{1},\mathbb{U})=0, \tag{2.4.4}$$

$$(\mathbb{U},\lambda\mathbb{1})=0. \tag{2.4.5}$$

Adding (2.4.4) and (2.4.5) gives $\mathbb{U}^TA\mathbb{U}=0$. Since A is SPD, (2.4.1) implies $\mathbb{U}=0$. Further, from $M[\mathbb{U},\lambda]^T=0$ we calculate

$$A\mathbb{U}-\lambda\mathbb{1}=-\lambda\mathbb{1}=0,$$

thus $\lambda=0$, completing the uniqueness calculation.

Example 2.4.3. We repeat the previous example, but change the boundary conditions from homogeneous Dirichlet to homogeneous Neumann.

$$\begin{cases} -u_{xx}(x)-\lambda=f(x), & x\in(0,1),\\ \int_0^1 u(x)dx=k,\\ u'(0)=u'(1)=0. \end{cases}$$

Let $B=\begin{bmatrix}1.5 & 1 & \cdots & 1 & 1.5\end{bmatrix}^T$. Then the approximation of the constraint function is

$$\int_0^1 u(x)\approx B^T\mathbb{U}. \tag{2.4.7}$$

To find the approximations to $\mathbb{U}$ and λ we solve the saddle point system

$$\begin{bmatrix} A & -B\\ B^T & 0\end{bmatrix}\begin{bmatrix}\mathbb{U}\\ \lambda\end{bmatrix}=\begin{bmatrix}\mathbb{F}\\ k/h\end{bmatrix}.$$

Thanks to the constraint we can show that the solution $[\mathbb{U},\lambda]^T$ exists and is unique. Analogously to the last example, define the matrix M as follows,

$$M=\begin{bmatrix} A & -B\\ B^T & 0\end{bmatrix},$$

and consider $M[\mathbb{U},\lambda]^T=0$. From the inner product $(M[\mathbb{U}\lambda]^T,[\mathbb{U},\lambda]^T)=0$ we again find that $\mathbb{U}^TA\mathbb{U}=0$, but A is SND and we conclude that $\mathbb{U}$ is constant. However, to satisfy

$$B^T\mathbb{U}=0 \tag{2.4.8}$$

it must be that $\mathbb{U}=0$. It follows that $\lambda=0$ and thus the solution exists and is unique.

2.4.2 Cell-centered finite differences for Poisson's equation

The models used in this work will frequently use homogeneous Neumann boundary conditions. In addition, it will be important for the models to be mass conservative. For this reason, in our realistic examples in $d = 2$ we employ the cell-centered variant of the finite difference method. We will also use this method for a mass-conservation correction to the Stokes problem.

To solve Poisson's equation we use the cell-centered finite difference scheme described in [38], which is equivalent to the expanded mixed finite element method where the approximation spaces are lowest order Raviart-Thomas spaces on a rectangular grid. The scheme in [38] is an extension of the scheme in [43], with a focus on the handling of boundary conditions.

We apply the model in [38] as follows. The mass balance equation is

$$\nabla \cdot U = f, \tag{2.4.9}$$

where U is the mass flux and f is a source term. Darcy's law, neglecting gravity, and lumping μ in with K is

$$U = -K\nabla P. \tag{2.4.10}$$

Combine (2.4.9) and (2.4.10) to get

$$-\nabla \cdot (K\nabla P) = f. \tag{2.4.11}$$

To discretize (2.4.9) and (2.4.10) we recall the expanded mixed finite element method with lowest order Raviart-Thomas spaces on a rectangular grid. Define test spaces

$$(W, V) = (L^2(D), H(div; D)),$$

for the pressure and velocity, respectively. The approximation spaces are $(W_h, V_h) \subset (W, V)$, where test functions $w_{ij} \in W_h$ are piecewise constant on cell D_{ij} and $v \in V_h$ are linear in one coordinate direction and constant in the others. For example, $v_{i+1/2,j}$ is linear in the x direction and constant in y, with support $D_{ij} \cup D_{i+1,j}$ and value 1 at

the support cells interface. We discretize domain D into uniform rectangular cells with cell width h. We suppress the subscript h in the rest of this model description.

The interior discretization is as follows. To discretize (2.4.9) multiply by test function w_{ij} and integrate over D to get

$$\int_D \nabla \cdot U w_{ij} = \int_D f w_{ij}. \tag{2.4.12}$$

The left hand side in (2.4.12) simplifies to

$$\int_D \nabla \cdot U w_{ij} = \int_{D_{ij}} \nabla \cdot U, \tag{2.4.13}$$

and the right hand side in (2.4.12) simplifies to

$$\int_D w_{ij} = \int_{D_{ij}} f. \tag{2.4.14}$$

For (2.4.13) in the x direction, employ the divergence theorem to get

$$\int_{D_{i+1/2,j}} U_{i+1/2,j} \cdot n + \int_{D_{i-1/2,j}} U_{i-1/2,j} \cdot n = h(U_{i+1/2,j} - U_{i-1/2,j}). \tag{2.4.15}$$

We solve for discrete velocity values U via Darcy's equation (2.4.10).

The following discretization of (2.4.10) assumes scalar K and is in only the x direction. Suppose K is not degenerate so one can write

$$K^{-1}U = -\nabla P. \tag{2.4.16}$$

Now, multiply (2.4.16) by test function $v_{i+1/2,j}$ and integrate over D,

$$\int_D K^{-1} u v_{i+1/2,j} = -\int_D \nabla P v_{i+1/2,j}.$$

Apply the trapezoidal rule to integration in the x direction and the midpoint rule in the y direction to get the equation for the nodal value $u_{i+1/2,j}$,

$$h\left(\frac{1}{2}K_{ij}^{-1} + \frac{1}{2}K_{i+1,j}^{-1}\right) u_{i+1/2,j} = (P_{i+1,j} - P_{ij}). \tag{2.4.17}$$

Define the transmissibilities $T_{i+1/2,j}$ as

$$T_{i+1/2,j} = h\left(\frac{1}{2}K_{ij}^{-1} + \frac{1}{2}K_{i+1,j}^{-1}\right)^{-1}.$$

Then rewrite equation (2.4.17) as

$$hU_{i+1/2,j} = T_{i+1/2j}(P_{i+1,j} - P_{ij}). \tag{2.4.18}$$

Note that the transmissibilities on an edge use harmonic averages of K values on the adjacent cells.

Combine (2.4.15) and (2.4.18) so that there is only a single variable to solve for, as in (2.4.11). We briefly show how this mixed finite element method is equivalent to the cell-centered finite difference scheme up to quadrature error. This mixed finite element discretization for (2.4.11) on left hand side is the familiar tri-diagonal matrix A as in the previous sections on finite difference methods, establishing that the left hand side is discretized similarly for the two methods. Use the trapezoidal method to approximate the integral in (2.4.14),

$$\int_{D_{ij}} f \approx f_{ij}, \tag{2.4.19}$$

then the right hand side for the mixed finite element scheme is equivalent to the finite difference scheme up to quadrature error in (2.4.19).

The boundary conditions considered for Poisson's equation in this work are Dirichlet boundary conditions and homogeneous Neumann boundary conditions. Suppose there is a boundary in the x direction on the right face. Let P_L be the value on the boundary. Define the boundary transmissibility to be

$$T_L = 2K.$$

Then the discretization (2.4.18) is modified to be

$$hU_{i+1/2,j} = T_L(P_L - P_{ij}).$$

To enforce the homogeneous Neumann boundary condition set

$$T_L = 0.$$

2.4.3 Numerical approximation for time dependent examples with $d = 1$

We extend the notation from 2.4.1 to include time dependence. Let $t \in (0, \infty)$. Discretize time by $t_n := \tau n$, for $\tau > 0$, $n = 0, 1, \ldots$. We will vary τ between examples

to maintain stability.

Let $u : D \times (0, \infty) \to \mathbb{R}$. In this case, u is a function of space and time. We denote pointwise approximations of u at time t as

$$u_i^n \approx u(x_i, t_n).$$

To denote vectors of function approximations at time t_n, we use

$$\mathbb{U}^n = \begin{bmatrix} u_1^n & u_2^n & \cdots & u_{M-1}^n \end{bmatrix}^T.$$

Let $f : \mathbb{R} \to \mathbb{R}$ which can be used when $f = f(u)$. We also we consider $f : \mathbb{R} \times \mathbb{R} \to \mathbb{R}$ useful for $f = f(x, t)$. Finally, we can have $f = f(x, u(x, t))$ or $f = f(x, t, u(x, t))$. We define $f_i^n = f(u_i^n)$ or $f_i^n = f(x_i, t_n)$ or $f_i^n = f(x_i, u_i^n)$ for the three cases listed, respectively. The particular meaning of f_i^n will be clear from the context.

Now we consider a specific time dependent problem of interest. This problem is similar to the gradient flow problems to be considered later in this work. Suppose we are interested in approximating the solutions $(u(x, t), \lambda(t))$ to the following nonlinear system of equations involving a semilinear parabolic equation, and subject to a constraint.

$$\begin{cases} u_t(x,t) - u_{xx}(x,t) - \lambda(t) = f(x), & x \in D, t > 0, \\ \displaystyle\int_D u(x,t) = k, & t > 0, \\ u(0,t) = u(1,t) = 0. & t > 0, \\ u(x,0) = u_{init}(x), & x \in D. \end{cases}$$

We apply discretizations in space and in time. In time, we apply the backward Euler scheme. We discretize in space as in Section 2.4.1. We solve the system

$$\begin{bmatrix} I + \tau A & -\tau \mathbb{1} \\ \mathbb{1}^T & 0 \end{bmatrix} \begin{bmatrix} \mathbb{U}^n \\ \lambda^n \end{bmatrix} = \begin{bmatrix} \mathbb{U}^{n-1} + \tau \mathbb{F} \\ k/h \end{bmatrix}.$$

The above scheme is unconditionally stable [26].

2.4.4 Approximation for nonlinear problems with Neumann conditions with $d = 2$

The main results formulated in this work are two dimensional phase separation problems in porous media. We provide now a statement on how we approximate their

solutions in $D \in \mathbb{R}^2$.

Let $f : \mathbb{R} \to \mathbb{R}$ be non-linear. Let $\lambda(t) \in \mathbb{R}$ and $u : D \times (0, \infty) \to \mathbb{R}$ be unknown and $k \in \mathbb{R}$ fixed. We use the nonlinear function f to achieve the desired modeling results; these are motivated below. Here we focus on the framework for the numerical approximation.

The system of equations we want to approximate is as follows

$$\begin{cases} u_t - \Delta u - \lambda = f(u), & x \in D,\ t > 0, \quad (2.4.21a) \\ \dfrac{\partial u}{\partial n} = 0, & x \in \partial D\ t > 0, \quad (2.4.21b) \\ u(x, 0) = u_{init}(x), & x \in D, \quad (2.4.21c) \\ \displaystyle\int_D u(x, t) = k, & t > 0. \quad (2.4.21d) \end{cases}$$

We discretize (2.4.21) as follows. In time, we treat linear terms implicitly with backward Euler scheme, and we treat the nonlinear terms associated with $f(u)$ explicitly in time. Schemes of this type are known as Implicit-Explicit (IMEX) schemes which can be beneficial due to their stability properties and ease of implementation.

In space we apply the cell-centered Poisson solver in Section 2.4.2. The terms $u,\ \lambda$ and f are all cell centered quantities. We consider the implicit in time treatment of $-\Delta u$ (discretized as in Section 2.4.2). We also solve implicitly for λ. We approximate (2.4.21d) as follows

$$\int_{D_f} u \approx h^2 \sum_{ij} u_{ij}. \quad (2.4.22)$$

The resulting system is an nonlinear algebraic saddle-point system. To find solutions, $\mathbb{U}$ and λ at every time step t_n, we solve the saddle point system

$$\begin{bmatrix} I + \tau A & -\tau \mathbb{1} \\ \mathbb{1}^T & 0 \end{bmatrix} \begin{bmatrix} \mathbb{U}^n \\ \lambda^n \end{bmatrix} = \begin{bmatrix} \mathbb{U}^{n-1} + \tau \mathbb{F}^{n-1} \\ k/h^2 \end{bmatrix}, \quad (2.4.23)$$

where I is the identity matrix. The numerical scheme shown above can be shown to converge at a rate $O(\tau + h^2)$ provided some mild stability conditions depending on f hold.

2.5 Newton's method

In this Section we give a brief outline of Newton's method. We follow the method as in [3, Ch. 5.4].

Let $\mathcal{F} : V \to V$ be Fréchet differentiable, with derivative denoted $\mathcal{F}'$. Let $u \in V$. To solve the equation

$$\mathcal{F}(u) = 0 \tag{2.5.1}$$

we use the following iterative method. Choose an initial guess $u^{(0)} \in V$, for $k = 0, 1, \ldots$, solve the equation

$$\mathcal{F}'\left(u^{(k)}\right)\left(u^{(k+1)} - u^{(k)}\right) = -\mathcal{F}\left(u^{(k)}\right) \tag{2.5.2}$$

for $u^{(k+1)}$.

Theorem 2.5.1. Assume u_* is a solution to (2.5.1) such that $\mathcal{F}'(u_*)$ is nonsingular, bounded, and locally Lipschitz continuous. Then there exists an $\delta > 0$ such that if $||u^{(0)} - u_*|| \leq \delta$, then the iteration (2.5.2) is well defined and converges to u_*. We have also the error bound

$$||u^{(k+1)} - u_*|| \leq C||u^{(k)} - u_*||^2, \tag{2.5.3}$$

for some constant C with $C\delta < 1$.

This theorem of local convergence with quadratic convergence supposes the existence of the root. A theorem due to Kantorovich however, does not suppose the existence of the root. One drawback on Kantorovich's theorem is that in practice it can often be difficult to verify the conditions for a given problem [3].

Theorem 2.5.2 (Kantorovich)**.** Let $r > 0$, $u^{(0)} \in V$ and $\mathcal{F}$ be continuously differentiable on $K = B(u^{(0)}, r) := \{x \in V : ||u^{(0)} - x|| < r\}$. Assume that $\mathcal{F}'$ is Lipschitz on K with constant γ, $\mathcal{F}'(u^{(0)})$ is nonsingular, and there exists two constants $\beta, \eta \geq 0$ such that

$$||\mathcal{F}'(u^{(0)})^{-1}|| \leq \beta$$
$$||\mathcal{F}'(u^{(0)})^{-1}\mathcal{F}(u^{(0)})|| \leq \eta.$$

If $\alpha = \beta\gamma\eta < 1/2$, then the iteration converges to the unique zero u_* of $\mathcal{F}$ in $B(u^{(0)}, r_1)$ where

$$r_1 = \min\left(r, \frac{1+\sqrt{1-2\alpha}}{\beta\gamma}\right).$$

Theorem 2.5.2 gives sufficient conditions for the Newton iteration (2.5.2).

3 Flow and Transport

In this chapter we introduce mathematical models of flow and transport in porous media. We follow established literature on the topic, and introduce those models which are relevant for this work. In particular, we follow [7] for Darcy scale models, [19] for pore scale models, and [52] for upscaling. Details are provided in what follows. We begin by discussing the different scales of interest. The models used to describe flow and transport are dependent on the scale of the problem considered.

At the pore scale we recognize individual grains and the viscous flow with fluid which moves in the void space between the grains, with attention paid to the variation of velocity from zero on pore walls to maximum somewhere in the flow channels between the walls. At Darcy scale we consider average quantities. We do not distinguish individual grains and channels of flow but rather how fluid moves through the porous medium in aggregate. We account for the presence of grains and channels in an average way through the coefficients of porosity and permeability. Porosity is a scalar coefficient that measures what fraction of the porous medium is void space. Permeability is a tensor coefficient that describes how easily fluid moves through a porous medium. These coefficients are clearly impacted by the geometry at the pore scale. They central to the models of flow and transport in porous media at Darcy scale described by partial differential equations. In this work we are interested in the applications in which the permeability and porosity change due to some phenomena associated with the flow and transport.

In this work, we consider porous media in which the individual pores have characteristic lengths on the order of μm to mm. This is a characteristic pore size for soils, or consolidated and unconsolidated sediments [7, Ch. 2.4]. Models for flow at the pore scale are useful because of their ability to capture flow through the void space. In principle, one can set up a computational model with sufficient resolution to simulate viscous flow (e.g., Stokes flow problem), through a cm scale sample of porous medium, whose results are upscaled to provide the coefficients of porosity and permeability. Such

a model would, however, require a million or more unknowns [15] in order to cover a large enough representative volume called REV (Representative Elementary Volume) of a cm length.

Furthermore, large scale applications in porous media or even lab experiments require that we model at a scale of m or km, the lab, core, or reservoir scales. Thus modeling the detailed flow entirely at pore scale is unfeasible since this would require an unmanageable complexity. When the porous medium has characteristic lengths on the order of m to km we use Darcy's law to describe the flow.

The capability to consider the detailed pore scale geometry and solve for the flow at pore scale is not completely lost, however. Through a technique called upscaling, we are able to take information from the lower scale, the pore scale models to the upper scale, Darcy scale. To move information from pore scale to Darcy scale we use homogenization. Homogenization is a means for taking a problem with very heterogeneous data and finding an approximating problem with averaged homogeneous quantities which can be solved more easily. In this work we employ both mathematical and computational homogenization. Both are called upscaling.

Even with upscaling, one faces another conundrum, since at this time it is unrealistic to think one might know the actual pore geometry of every single REV of porous medium. Instead, in [15] the authors proposed to consider random ensembles of pore scale geometries, and produce experimental distributions of porosity and permeability, from which one can draw to simulate at Darcy scale.

The focus of this work is to consider pore geometries in which some new obstructions arise. In particular, we consider the obstructions which form due to one of two possible mechanisms of interest: the growth of biofilm or hydrate crystal growth. In the following Chapters we introduce these two applications and explain why we are interested in these particular obstructions, and provide context for how our strategy for studying obstructions fits within the field. For each realization of a geometry with obstructions we simulate the flow and calculate upscaled coefficients. This section provides the background on these tasks.

In Section 3.1 we present several different models for flow in porous media. In Section 3.2 we present advective transport. In Section 3.3 we discuss the process of upscaling. In Section 3.4 we present numerical methods to solve for flow. In Section 3.5 we present numerical methods to solve for transport.

3.1 Models of flow in porous media

In this section we recall basic models of flow in porous media. We explain four different models which have particular scales associated with them. In particular, we discuss the Stokes flow model, Darcy flow model, Brinkman's flow model, and the immersed boundary Stokes flow model, which is a localized Brinkman's flow.

Each model consists of equations for mass conservation and momentum conservation. Since we consider only fluid that is incompressible, the mass conservation equation has the same form for each of the models. However, the momentum equation depends on the scale at which it is posed and which flow features we are trying to capture in the model. In all cases, the momentum equation describes a relationship between the fluid velocity and pressure gradient.

We start by defining some notation. Let D denote a region of porous medium. The porous domain is partitioned into the solid matrix, D_s and the flow domain D_f, so $D = D_s \cup D_f \cup \Gamma_{s,f}$. Refer to Figure 3.1 for an example porous domain. The distinction between the flow domain and the solid matrix is necessary at the pore scale. For pore scale flow, the solid matrix is the grains which are assumed to be impermeable; the flow domain is the space between the grains, where fluid may flow. We assume that the flow domain is connected, but the solid matrix does not have to be connected. In computational simulations of flow we also assume that the flow domain is connected to the inflow and outflow boundaries to be defined in the sequel.

At the pore scale the momentum and mass conservation equations are posed in D_f. Let $u : \mathbb{D}_f \to \mathbb{R}^d$ denote velocity and $p : \mathbb{D}_f \to \mathbb{R}$ denote pressure. The flow model at pore scale considered here is the Stokes flow model; we describe it in Section 3.1.1.

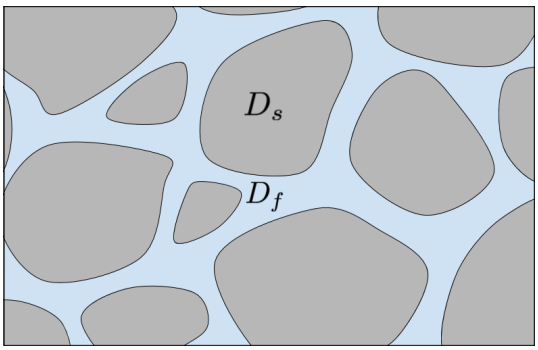

FIGURE 3.1: A cartoon of a porous medium cross-section. The grey grains represent the solid matrix D_s. The connected blue region is the flow domain D_f.

At Darcy scale the momentum and mass conservation equations are posed on D. Let $U : D \to \mathbb{R}^d$ denote the Darcy flux and $P : D \to \mathbb{R}$ denote Darcy scale pressure. The flow model at the Darcy scale considered here is the Darcy flow model described in Section 3.1.2. For the Darcy model geometry information based on D_f and D_s are incorporated into the coefficients permeability, K, tortuosity, $\mathbf{T}$, and porosity, ϕ. For Darcy scale flow the coefficients K and ϕ are local averages based on the porous media geometry. The different domains on which pore scale and Darcy scale flow are solved is a crucial distinction.

We will consider the case where obstructions appear at the pore scale of the porous medium. In the presence of obstructions, the domain is further refined into rock matrix, D_r, obstruction, D_o, and void space, D_v. When the obstructions are permeable, the obstructions are part of the flow domain, $D_f = D_{v,o}$. When the obstructions are not permeable, the obstructions are part of the solid matrix, $D_s = D_{r,o}$. We will make clear when necessary which situation we are considering. The reader is reminded that notation for the partitioning of domain spaces was defined in Section 2.1.

Denote the components of U as U_i, $i = 1, \ldots, d$, i.e. $U = (U_1, \ldots, U_d)$. Let $\mu \in \mathbb{R}$ be the dynamic viscosity, $K \in \mathbb{R}$ be the permeability, and $\rho \in \mathbb{R}$ be fluid density.

3.1.1 Pore scale flow model

We use Stokes equations to solve for the flow at the pore scale. To develop the Stokes equations we follow [19, Ch. 3]. The Stokes equations are

$$\begin{cases} -\mu\Delta u + \nabla p = f, & \text{in } D_f, \quad (3.1.1a) \\ \nabla \cdot u = 0, & \text{in } D_f. \quad (3.1.1b) \end{cases}$$

The fundamental assumption when using this Stokes model is that the flow is "slow" and "steady", so we neglect any turbulence or inertial effects in the flow.

Stokes equation is appropriate for flow with a low Reynolds number, or laminar flow regime. The Reynolds number has many definitions, but we follow one given in [7],

$$\mathrm{Re} = \frac{\rho u l}{\mu}.$$

One can see that slow flow with a short characteristic length, l, relative to the fluid viscosity has a low Reynolds number.

For boundary conditions, we decompose $\Gamma = \partial D_f$ into three parts, $\Gamma = \Gamma_{wall} \cup \Gamma_{in} \cup \Gamma_{out}$, shown in Figure 3.2. The boundary Γ is also decomposed into the parts where we impose Dirichlet and Neumann conditions. We prescribe values for u on the Dirichlet part of the boundary. In particular, $\Gamma_{wall} = \partial D_f \cap \partial D_s$ is the fluid-solid interface. On Γ_{wall} we impose the no-slip boundary condition. Next, Γ_{in} is an inflow boundary. On the Neumann part of the boundary we prescribe values for the total stress in the normal direction; in particular, Γ_{out} is a outflow boundary. We assign values as follows,

$$\begin{cases} u = 0, & \text{on } \Gamma_{wall}, \quad (3.1.2a) \\ u = u_D(x), & \text{on } \Gamma_{in}, \quad (3.1.2b) \\ \mu\nabla u \cdot n - pn = 0, & \text{on } \Gamma_{out}. \quad (3.1.2c) \end{cases}$$

Note that the Dirichlet boundary, Γ_D, is comprised of two parts of the boundary, $\Gamma_D = \Gamma_{wall} \cup \Gamma_{in}$.

The solvability of (3.1.1) with boundary conditions (3.1.2) is well established for $f \in L^2(D_f)$ (see, e.g., [20]). In the case where $\Gamma_{out} = \emptyset$ and $u_D = 0$, then a unique solution $u \in H_0^1(D_f)$ and $p \in L^2(D_f)\backslash\mathbb{R}$ exists. We note that p is only unique up to a constant. Now, if $\Gamma_{out} \neq \emptyset$ and u exists and is unique, then $-\Delta u + \nabla p = f$

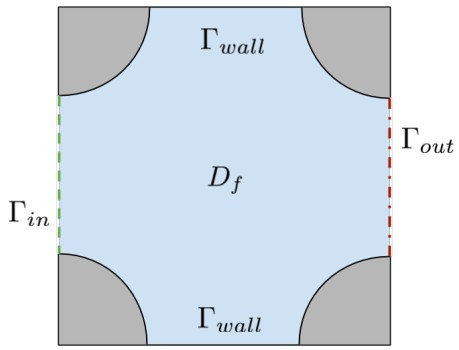

FIGURE 3.2: Illustration of a pore geometry and a possible partition of the boundary. Γ_{in} is shown as the left, dashed green boundary. Γ_{out} is shown as the right, dash-dotted red boundary. Γ_{wall} is shown as the solid black lines.

specifies p up to a constant, but then on Γ_{out} we have $\nabla u \cdot n - pn = 0$ which fixes p. We will approximate solutions $u \in H^1(D_f)^d$ and $p \in L^2(D_f)$ numerically using the computational environment called HybGe-Flow3D [14] which is described later in this chapter.

Example 3.1.1 (Hagen-Poiseuille flow)**.** In this example we describe Hagen-Poiseuille flow, that is flow described by (3.1.1) with boundary conditions (3.1.2) in a long uniformly cylindrical tube $D_f = (0, L)\times(-R, R)$ with radius R and length L, see Figure 3.3. The flow is in the lengthwise x_1 direction of the tube and there is no flow in the radial x_2 direction.

For the Hagen-Poiseuille flow the boundary conditions are as follows. At the wall of the tube apply the no-slip condition on $\Gamma_{wall} = \{x : x_2 = \pm R\}$. At the left boundary $\Gamma_{in} = \{x : x_1 = 0\}$ we have the inflow condition, and impose the same flow at $\Gamma_{out} = \{x : x_1 = L\}$. The inflow condition has the well-known parabolic profile which maintains continuity of u on $\Gamma_D = \Gamma_{in} \cup \Gamma_{wall}$. The fully developed flow solution has the same parabolic profile throughout the tube.

The velocity $u = (u_1, u_1)$ solution is

$$u_1 = \frac{1}{\mu}(R^2 - x_2^2),$$
$$u_2 = 0. \tag{3.1.3}$$

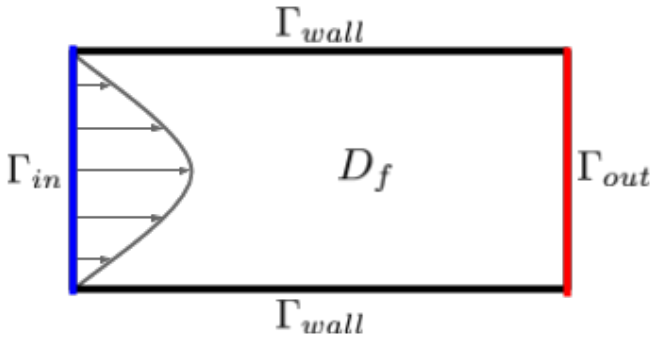

FIGURE 3.3: Hagen-Poiseuille flow as described by (3.1.1) and (3.1.2).

The pressure p solution is unique up to a constant $c \in \mathbb{R}$,

$$p = -2x_1 + c.$$

3.1.2 Darcy scale flow model

To model flow at the Darcy scale we use Darcy's law (3.1.4). To develop Darcy's law we follow [7, Ch. 4]. The porous media system is

$$\begin{cases} \mu U = -K\nabla P, & \text{in } D, \quad (3.1.4a) \\ \nabla \cdot U = 0, & \text{in } D. \quad (3.1.4b) \end{cases}$$

Throughout this work we ignore gravity which would otherwise appear on the right hand side of (3.1.4a).

Darcy's law originated as an empirical law proposed by Henri Darcy in 1856. It has since been shown to have a physical basis as a momentum equation and can also be derived from Stokes equation through asymptotic homogenization.

The Darcy flux, U, is the discharge per unit area. It has units of length per time. The domain on which Darcy's law is solved is D, rather than D_f as in Stokes equation. This characteristic makes Darcy's law ideal for the numerical modeling of flow at realistic reservoir length scales.

We partition the boundary at Darcy scale as follows. Let $\Gamma = \Gamma_D \cup \Gamma_N = \partial D$, with Dirichlet boundary conditions on Γ_D and Neumann boundary conditions on Γ_N,

$$\begin{cases} P = P_D, & \text{on } \Gamma_D, \quad (3.1.5a) \\ U \cdot n = G, & \text{on } \Gamma_N. \quad (3.1.5b) \end{cases}$$

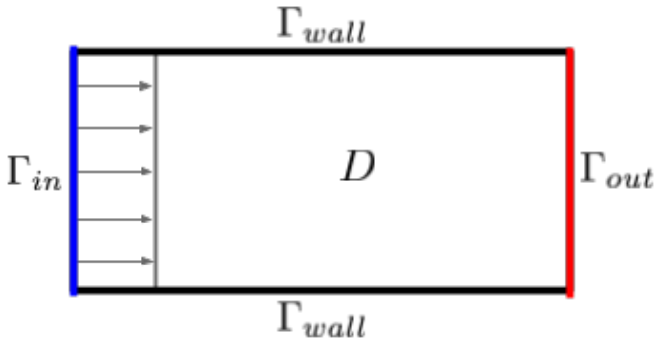

FIGURE 3.4: A cartoon of potential flow modeled with Darcy's equation. In fact U_1 and U_2 are constant in D; if one interprets this example as the Hagen-Poiseuille flow averaged across domain D.

If Γ_D is non-empty, there is a unique solution (P, U) to (3.1.4) and (3.1.5).

See Figure 3.4 for an illustration of solutions to a flow modeled with (3.1.4) using boundary conditions (3.1.5). The flow pictured is subject to the no flow conditions on the top and bottom boundaries, i.e. $U \cdot n|_{\Gamma_{wall}} = U_2|_{\Gamma_{wall}} = 0$. Second, to obtain $U_1 = const$ in the entire domain, we can either (i) use Neumann boundary conditions, or (ii) Dirichlet boundary conditions. For (i), we set Neumann boundary conditions with $U_1 = G = const$ on the left and right boundaries Γ_{in} and Γ_{out}, and obtain pressure solution unique up to a constant. Or we (ii) set $\Gamma_D = \Gamma_{in} \cup \Gamma_{out}$ and set pressures $P|_{\Gamma_{in}} = P_{in}$ and $P|_{\Gamma_{out}}$ with some $P_{in} > P_{out}$.

3.1.3 Brinkman model

When the fluid flow domain contains both the porous domain and free flow domain, or alternatively when the porosity is high, is it is preferable to use Brinkman's equation rather than Stokes equation [7]. This is related to an incompatibility in the boundary conditions of free flow and flow in the porous media. For flow in the fluid domain described by Stokes equation (3.1.1), there is a no-slip condition at the interface with the solid porous media, as in Figure 3.3. For flow in the porous media described by Darcy's law there is slippage, i.e. non-zero flow, at the boundary, as in Figure 3.4. Brinkman's equation resolves the interface incompatibility. Without Brinkman's equation one would

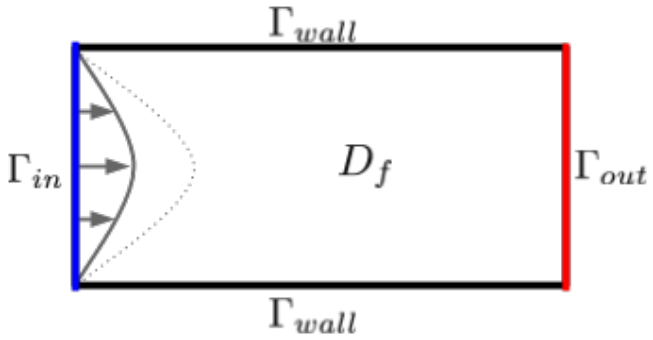

FIGURE 3.5: A Brinkman flow profile. The dotted line is the Stokes flow solution for Hagen-Poiseuille flow. The solid line shows how the drag term in the Brinkman model slows the flow.

have to pose some delicate interface conditions.

Brinkman's equation is

$$\begin{cases} -\mu\Delta U + \mu K^{-1}U = -\nabla P, & \text{in } D_f, \quad (3.1.6a) \\ \nabla \cdot U = 0, & \text{in } D_f. \quad (3.1.6b) \end{cases}$$

The Brinkman equation shares characteristics with both Stokes equation and Darcy's law. The Laplacian ΔU is found in both Stokes equation and Brinkman's equation. In Brinkman's equation, ΔU accounts for the energy dissipation due to the shear rate within the fluid [7, Ch. 4]. The term $K^{-1}U$ is found in both Darcy's law and Brinkman's equation and accounts for the drag of fluid due to the presence of porous medium.

A flow profile for Brinkman flow is shown in Figure 3.5. Here, the K^{-1} term is a drag term on the flow, slowing down the flow relative to Stokes flow.

3.1.4 Immersed boundary Stokes model

As mentioned above in this work we are interested in the flow in pore scale geometries in which some new permeable or impermeable obstructions appear due to the transport or other processes. If these obstructions are impermeable, we can treat them as part of the solid domain D_s, and a computational model would have to use new grid for the flow domain.

However, if they are permeable, say with permeability K, we should formulate a flow model such as Brinkman model to account for these.

The idea is to account together for all the possible obstructions. The case when $K = 0$ corresponds to impermeable obstructions. The case when $K = \inf$ corresponds to the Stokes model. The case when K is finite but nonzero would require Brinkman model. To bridge these cases we consider the immersed boundary Stokes model described below.

The flow model of principle interest in this work is the immersed boundary Stokes model (IBSM) for obstructions presented in [15, 2.4]. We use this model in particular when the obstructions at pore scale are permeable, but we aim to use the model also in the limiting cases of infinitely permeable obstructions or no obstructions.

Now we consider that the flow domain consists of void space and obstructions, $D_f = D_{v,o} \cup \Gamma_{v,o}$. Since the void space and obstructions can be saturated with fluid, it makes sense to call this domain D_f. The solid matrix is comprised of only the rock matrix, $D_s = D_r$. The entire domain is $D = D_s \cup D_f \cup \Gamma_{s,f}$. Let $\Gamma = \Gamma_{s,f}$ denote the interface between the solid matrix and the flow domain.

The flow model is as follows,

$$\begin{cases} -\mu\Delta u + \dfrac{1}{\eta}\mathbb{1}_{D_o} u + \nabla p = f, & \text{in } D_f, \quad (3.1.7a) \\ \nabla \cdot u = 0, & \text{in } D_f, \quad (3.1.7b) \\ u = 0, & \text{on } \Gamma. \quad (3.1.7c) \end{cases}$$

The coefficient $\eta \in \mathbb{R}$ is a volume penalty parameter that corresponds to the permeability of the obstructions. It is shown in [15] that as $\eta \to 0$, the velocity on D_0 decreases at $O(\sqrt{\eta})$. As $\eta \to \infty$, we have that (3.1.7) approaches (3.1.1). In Figure 3.6 we show an illustration of what flow modeled with this equation looks like.

In Figure 3.7 we exhibit how the IBSM can be used to approximate flow through permeable and impermeable obstructions. The fluid moves from left to right, with no-slip boundary conditions on the top and bottom boundary. The rectangular obstruction D_o is in the center of the channel and outlined with a dashed black line.

In the top figure we set $\eta \approx 0$ so that the obstruction is impermeable and we find that the flow velocity in the obstruction is machine zero. In the bottom figure we set

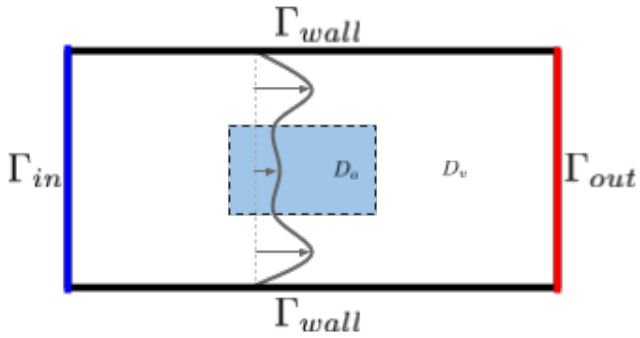

FIGURE 3.6: An IBSM flow profile. The blue box is a permeable obstruction. The solid line exhibits x-direction velocity at the dotted line.

$\eta > 0$ so that the obstruction is permeable. The flow velocity in the obstruction clearly is non-zero, yet has a lower magnitude than the flow velocity around the obstruction.

If one identifies η^{-1} with μK^{-1}, then (3.1.7) can be viewed as a local Brinkman's equation. This model is an alternative to flow models utilizing the Beavers-Joseph-Saffman interface conditions between Stokes and Darcy domains [2].

Well-posedness of (3.1.7) is discussed in [15].

3.1.5 Tortuosity

Beside porosity and permeability there are other quantities important for Darcy scales model of flow and transport that can be derived from pore scale simulations. In this section we consider *tortuosity*.

Tortuosity $\mathbf{T}$ is a coefficient that measures how tortuous a path the fluid must take to cross the domain. As stated in [6], the permeability of a porous medium depends on its porosity, its tortuosity and the average medium conductance, a characteristic related to the cross-sections of the channels through which flow takes place.

There are many definitions and many uses of tortuosity, explained in depth in [12]. In this work we use the notion of hydraulic tortuosity. Denote the straight-line length of a domain D in the direction of flow as l. Also, denote the effective path length taken by the fluid across D as l_{eh}, i.e. the fluid path through D_f. Then the hydraulic tortuosity

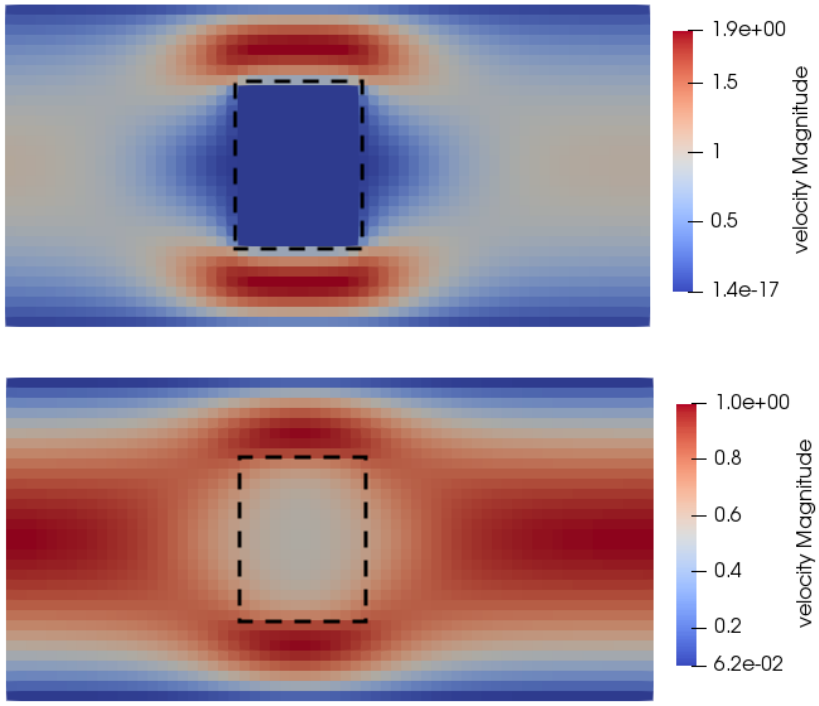

FIGURE 3.7: Velocity magnitude solutions to (3.1.7), as calculated by HybGe-Flow3d. Top: impermeable obstruction. Bottom: permeable obstruction.

is

$$\mathbf{T} = \frac{l_{eh}}{l_{min}}. \tag{3.1.8}$$

In [6] it is stated that this definition is incorrect and that the term on the right should be squared. Nonetheless, we use (3.1.8) as given in [12].

3.2 Models of transport in porous media

There are many phenomena taking place in the subsurface causing the transport of chemical species. They include advection, diffusion and dispersion. The model used in this work incorporates only advection of a single species. Advection is the process of being moved by the bulk flow of a fluid. In many applications it is appropriate to assume that the species being advected do not impact the flow itself. While the purpose of this work is to show the pore scale geometry is affected by some transport phenomena, we do not account directly for the local modification, e.g, of flow viscosity or magnitude in

the transport models.

Furthermore, the problems we are considering involve approximating solutions to viscous laminar flow and transport models with lower order numerical schemes; we will assume physical diffusion to be negligible. In fact, it is likely that the numerical diffusion in the lower order numerical transport schemes used is significant enough to outweigh the actual physical diffusion. Therefore, we do not address diffusive transport below.

We consider advective transport in both the Lagrangian and Eulerian frames of reference. The Lagrangian frame of reference follows an object being advected, and the solutions follow streamlines. The Eulerian frame of reference holds steady in space, observing particles moving through a location. In Section 3.5 we discuss the numerical approaches to solving for each frame of reference.

3.2.1 Transport at the Darcy scale

Let $C \in \mathbb{R}^d \to \mathbb{R}$ denote Darcy scale solute concentration. The model for transport at the Darcy scale in [27] is

$$\frac{\partial}{\partial t}(\phi C) + \nabla \cdot (-\phi \mathbf{T} D \nabla C + UC) = R, \tag{3.2.1}$$

where D is the diffusion coefficient, $\mathbf{T}$ is the tortuosity, ϕ is the porosity and R is a reaction term. By assuming that ϕ is constant in time, diffusion is negligible, and there is no reaction term, we simplify (3.2.1) to

$$\begin{cases} \phi C_t + \nabla \cdot (UC) = 0, & \text{in } D, \quad (3.2.2a) \\ C(x_0, 0) = C_0(x_0), & \text{in } D, \quad (3.2.2b) \\ C = C_D, & \text{on } \Gamma_{in}. \quad (3.2.2c) \end{cases}$$

Darcy fluxes U are given or can be found via the numerical homogenization technique discussed in Section 3.3.1. In what follows we assume U is constant. This is valid, e.g. following the upscaling over D. The homogenization process produces a constant U on D.

Because U is constant, one can calculate an analytical solution to (3.2.2) with the

method of characteristics. When $d = 2$, the solution is as follows for $U = (U_1, U_2)$,

$$C(x,t) = C_0\left(x_1 - \frac{U_1}{\phi}t, x_2 - \frac{U_2}{\phi}t\right). \tag{3.2.3}$$

3.2.2 Advection at the pore scale

Let $c \in \mathbb{R}^d \to \mathbb{R}$ denote pore scale solute concentration. The model for pore scale advection is the following system

$$\begin{cases} c_t + \nabla \cdot (uc) = 0, & \text{in } D_f, \quad (3.2.4a) \\ c(x,0) = c_0(x), & \text{in } D_f, \quad (3.2.4b) \\ c = c_D, & \text{on } \Gamma_{in}. \quad (3.2.4c) \end{cases}$$

The advection model at porescale is very similar to that at Darcy scale. The main difference is the absence of porosity coefficient and the use of u instead of U. We recall that, unlike U, the velocity u is not constant. In addition, the inflow boundary at the porescale Γ_{in} is, in practice, just a subset of the inflow boundary at the Darcy scale.

3.2.3 Breakthrough curves

We use breakthrough curves to compare the flow and transport through different geometries. Breakthrough curves measure the total amount of solute leaving the domain of interest over time, depending on the flow conditions such as the geometry at the porescale or permeability at Darcy scale.

Some common ways of measuring breakthrough are as follows

$$B(t) = \int_{\Gamma_{out}} (u(x) \cdot n) c(x,t)\ dx, \tag{3.2.5}$$

$$B(t) = \frac{\int_{\Gamma_{out}} (u(x) \cdot n) c(x,t)\ dx}{\int_{\Gamma_{out}} u(x) \cdot n}, \tag{3.2.6}$$

$$B(t) = \int_{\Gamma_{out}} c(x,t)\ dx. \tag{3.2.7}$$

In particular, the second definition attempts to remove the dependence of the breakthrough curves on the magnitude of the flow velocity, which in turn depends on the flow boundary conditions.

The breakthrough curve definitions we use in this work are (3.2.5) and (3.2.7). Definitions similar to those above can be formulated at Darcy scale as well.

3.3 Upscaling

In this section we discuss mathematical and computational methods which relate the models and quantities defined at the microscale to their macroscale counterparts.

There are many ways to relate microscale to macroscale models called "upscaling". Techniques of asymptotic expansions or homogenization are popular in mathematics, while techniques of volume averaging have been popular in other sciences and engineering. Numerical homogenization or upscaling are used in computational science. These techniques are used in many contexts and applications. Here we only discuss to the upscaling from pore to Darcy scale. The mathematical theory of homogenization presented rigorously ties the pore scale and Darcy scale models and variables together, based on an assumption that the geometry of the medium is periodic. Numerical homogenization is the method used in practice to utilize information from pore scale simulations in Darcy scale simulations, and works well even if the geometry is not periodic.

As mentioned in Section 3.1, flow at pore scale is solved in D_f, so flow solutions respect the exact geometry of the porous media. However, flow at Darcy scale is solved in D, so the flow solutions lose detail in the geometry. To balance the loss in geometric detail in Darcy scale models, coefficients that represent geometric qualities such as permeability K, porosity ϕ, and tortuosity $\mathbf{T}$ are included. Upscaling is a means for obtainig these coefficients.

Numerical homogenization uses geometries known as Representative Elementary Volumes (REV). REV's are the smallest porous media geometries still large enough to capture all the necessary features of that porous medium. The size of an REV depends on the characteristic of the porous medium being upscaled. For example, to upscale porosity an REV needs to be at least 50 times the pore radius [7, Ch. 1.3.4].

One of the classic results in homogenization is upscaling Stokes flow to Darcy flow [52].

The results of homogenization are useful in establishing formal models for flow and transport, however, these techniques are not ideally suited to our computational models. Homogenization assumes periodic media, but our simulations will be run on

non-periodic packed beads derived from physical experiments. Thus, we employ a numerical homogenization scheme as well.

In Section 3.3.1 we present the numerical method for the homogenization of pore scale flow following [37, 36].

3.3.1 Numerical homogenization

We follow the volume averaging approach detailed in [36]. We present the case where pore scale flow is modeled by immersed boundary Stokes flow (3.1.7). The homogenization for pore scale flow modeled by Stokes flow (3.1.1) is similar and can be found in [36].

This method assumes knowledge of pore scale flow, u, pressure p, and geometry, to calculate Darcy scale flux, U, pressure P, porosity, ϕ, and permeability, K. If the porous medium is isotropic, then K is scalar. If the porous medium is anisotropic, then $K \in \mathbb{R}^{d\times d}$ is a tensor.

Assume a known pore scale domain $D = D_{f,s}$, with permeable obstructions present, $D_f = D_{v,o}$. The geometry D has a uniform, rectangular discretization aligned with an orthogonal coordinate system with base vectors e^i, $i = 1, \ldots, d$. For a series of computational experiments $j = 1, 2, \ldots$, we calculate numerical solutions (u_h^j, p_h^j) to (3.1.7).

Next, we superimpose a Darcy scale rectangular grid on D. The Darcy scale grid, D^*, is composed of a macro cell, shown in Figure 3.8. Let $D^* \subsetneq D$, be a proper subset such that the boundaries of D^* are far enough from the inlet and outlet boundaries of D. We average over the subset domain D^* due to potential numerical artifacts at the boundaries, such as backflow at the outlet. Define the following subsets of D^*: $D_L = D_{1,3}$, $D_R = D_{2,4}$, $D_B = D_{1,2}$, and $D_T = D_{3,4}$. Let x_A be the centroid of D_A.

We calculate the porosity as follows,

$$\phi = \frac{|D_f \cap D^*|}{|D^*|}.$$

We calculate the Darcy flux as follows,

$$U_h^j = \langle u_h^j \rangle_{D^*} = \frac{1}{|D^*|} \int_{D^* u_h^j} = \phi \frac{1}{|D^* \cap D_f|} \int_{D^* \cap D_f} u_h^j.$$

Denote the components of U_h^j as U_i^j, $i = 1, \ldots, d$. Note that u_h is extended on D^* as $u_h|_{D^* \cap D_s} = 0$. We calculate average pressures on $D_A \subset D^*$ as follows

$$P_A^j = \langle p_h^j \rangle_{D_A}.$$

Approximate the pressure gradient as follows

$$(G_{LR}^j, G_{TB}^j) = -\nabla P^j \approx \left(\frac{P_L^j - P_R^j}{x_R - x_L}, \frac{P_B^j - P_T^j}{x_T - x_B} \right).$$

For each experiment, $j = 1, \ldots, d$, the global flow is aligned with e^j. Let e^1 point left to right. Then boundary conditions imposed on (3.1.7) are inflow on the left boundary, outflow on the right boundary and no-slip elsewhere.

Then we calculate K from (3.1.4). For each experiment j we can write

$$\begin{cases} \mu U_1^j = K_{11} G_{LR}^j + K_{12} G_{TB}^j, \\ \mu U_2^j = K_{21} G_{LR}^j + K_{22} G_{TB}^j. \end{cases}$$

With d experiments we can create the following system,

$$\mu \begin{bmatrix} U_1^1 \\ U_2^1 \\ U_1^2 \\ U_2^2 \end{bmatrix} = \begin{bmatrix} G_{LR}^1 & G_{TB}^1 & & \\ & & G_{LR}^1 & G_{TB}^1 \\ G_{LR}^2 & G_{TB}^2 & & \\ & & G_{LR}^2 & G_{TB}^2 \end{bmatrix} \begin{bmatrix} K_{11} \\ K_{12} \\ K_{21} \\ K_{22} \end{bmatrix}. \tag{3.3.1}$$

Due to the judicious choice of experiments, this system is non-singular in practice and we can solve for K.

Symmetry of K is a fundamental property of permeability, but it is not imposed by the method just described. Instead, symmetry of K should come naturally from a good method and set of experiments.

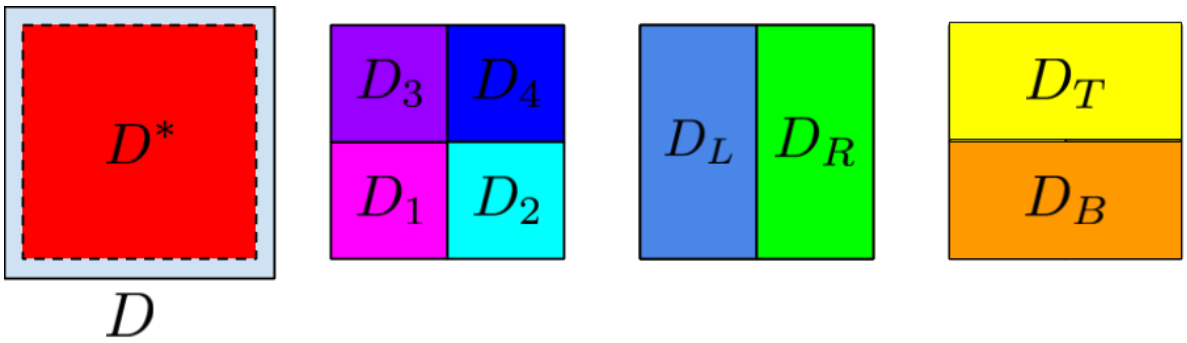

FIGURE 3.8: Domain partitioning for numerical homogenization scheme in Section 3.3.1. From left to right: Domain $D* \subsetneq D$; $D^* = \bigcup_{i=1}^{4} D_i$; $D_L = D_{1,3}$ and $D_R = D_{2,4}$; $D_B = D_{1,2}$ and $D_T = D_{3,4}$.

3.3.2 Remarks on upscaling flow coupled to transport

The approximation for Darcy flux is based on Dupuit's relation [12],

$$U = \langle u \rangle_{D_f} \phi. \tag{3.3.2}$$

This is a natural and reasonable approximation; the seepage velocity is the average fluid velocity reduced in magnitude by the fraction of the space available to the fluid. An interesting feature of this relation, however, is that this relationship alone does not capture the impact of pore scale obstructions in our numerical experiments. Employing the numerical homogenization technique in 3.3.1, for flow in one direction we find that that the principle components of U are constant, dependent only on the boundary conditions and not on the geometry. Clearly the other component(s) of U as well as the pressure distribution depend on the pore geometry and in particular on the presence of obstructions, but the transport model (3.2.2) will not "see" these other quantities. We demonstrate this below.

Let $D = (a, b) \times (c, d)$ be a rectangular Darcy scale domain of fixed size aligned with the coordinate axis, with associated pore scale flow domain D_f. Let γ^A be a collection of segments within a pore scale line in D at some $A \in (a, b)$. We define $\gamma^A = \{(A, y) : (A, y) \in D_f\}$. Let $\bar{\gamma}^A$ be the associated macroscale line segment that subsumes γ^A, $\bar{\gamma}^A = \{(A, y) : y \in (c, d)\}$. See Figure 3.9 for an illustration.

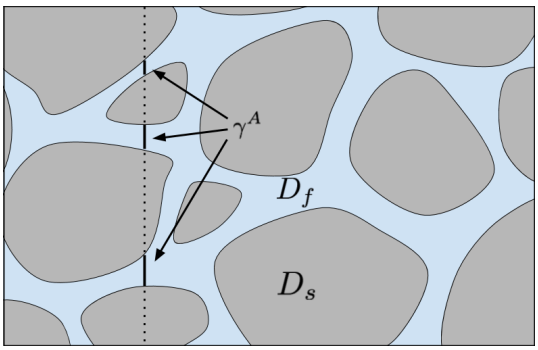

FIGURE 3.9: A porous media domain with a line specified. The solid vertical lines denote the portions of pore scale line γ^A. The macroscale line $\bar{\gamma}^A$ is comprised of the solid and dotted lines.

Define ϕ_A as the "porosity" of γ^A,

$$\phi_A = \frac{|\gamma^A|}{|\bar{\gamma}^A|}.$$

Extend this definitions to the boundaries, so that $\gamma^a,\ \gamma^b$ are the pore scale boundaries on the left and right of D_f respectively, and that $\bar{\gamma}^a,\ \bar{\gamma}^b$ are the Darcy scale boundaries of D on the left and right, respectively.

Lemma 3.3.1. Consider Stokes flow with boundary conditions as in (3.1.1) on D_f with geometry as described above. Let $\Gamma_{in} = \gamma^a$, so $n = (-1, 0)$, and let $\Gamma_{out} = \gamma^b$, so $n = (1, 0)$. All other boundaries have the no-slip condition on Γ_{wall}. Then

$$U_1 := \langle u_1 \rangle_{D_f} \phi = \langle u_1 \rangle_{\gamma^a} \phi_a \tag{3.3.3}$$

Proof. The proof is completed in $d = 2$, but the idea works also in $d = 3$.

The first step is integrating the incompressibility condition, (3.1.1b), using Green's theorem in (3.3.4) and enforcing no slip conditions on Γ_{wall} to get that the total flow over the inlet is equal to the total flow over the outlet. Observe that,

$$\begin{aligned} 0 = \int_{D_f} \nabla \cdot u &= \int_{\Gamma} u \cdot n \\ &= \int_{\Gamma_{in}} u \cdot n + \int_{\Gamma_{out}} u \cdot n + \int_{\Gamma_{wall}} u \cdot n, \\ &= -\int_{\Gamma_{in}} u_1 + \int_{\Gamma_{out}} u_1. \end{aligned} \tag{3.3.4}$$

Thus, by (3.3.4)

$$\int_{\Gamma_{in}} u_1 = \int_{\Gamma_{out}} u_1.$$

Next, we note that u can be extended on $\bar{\gamma}^A$ by $u|^{\bar{\gamma}^A/\gamma^A} := 0$. This extension allows the macro scale flux to be written as an average over the macro scale domain,

$$\phi_A \langle u \rangle = \frac{\phi_A}{|\gamma^A|} \int_{\gamma^A} u = \frac{1}{|\bar{\gamma}^A|} \int_{\bar{\gamma}^A} u.$$

Next, we show the Darcy flux at the outlet is equal to the Darcy flux at the inlet,

$$\phi_b \langle u_1 \rangle_{\gamma^b} = \frac{\phi_b}{|\gamma^b|} \int_{\gamma^b} u_1 = \frac{1}{|\bar{\gamma}^b|} \int_{\bar{\gamma}^b} u_1 = \frac{1}{|\bar{\gamma}^a|} \int_{\bar{\gamma}^a} u_1 = \frac{\phi_a}{|\gamma^a|} \int_{\gamma^a} u_1 = \phi_a \langle u_1 \rangle_{\gamma^a}.$$

Now, this works across any vertical cross section, γ^A. Thus, as a consequence of incompressibility,

$$\phi_A \langle u \rangle_{\gamma^A} = \phi_a \langle u \rangle_{\gamma^a}.$$

We now prove our claim,

$$\begin{aligned}
U_1 &:= \phi \langle u_1 \rangle_{D_f} \\
&= \frac{\phi}{|D_f|} \int_{D_f} u_1 \\
&= \frac{1}{|D|} \int_D u_1 \\
&= \frac{1}{|D|} \int_a^b \int_c^d u_1 \\
&= \frac{1}{|D|} \int_a^b |\bar{\gamma}^a| \phi_a \langle u_1 \rangle_{\gamma^a} \\
&= \phi_a \langle u_1 \rangle_{\gamma^a}.
\end{aligned}$$

□

This result shows that for Stokes flow restricted to one direction, the average velocity in the principal direction depends only on the conditions at the inflow boundary. Of course, U_2 and the pressure p as well its upscaled pressure gradient depend both on the actual pore geometry.

We give an example to illustrate Lemma 3.3.1.

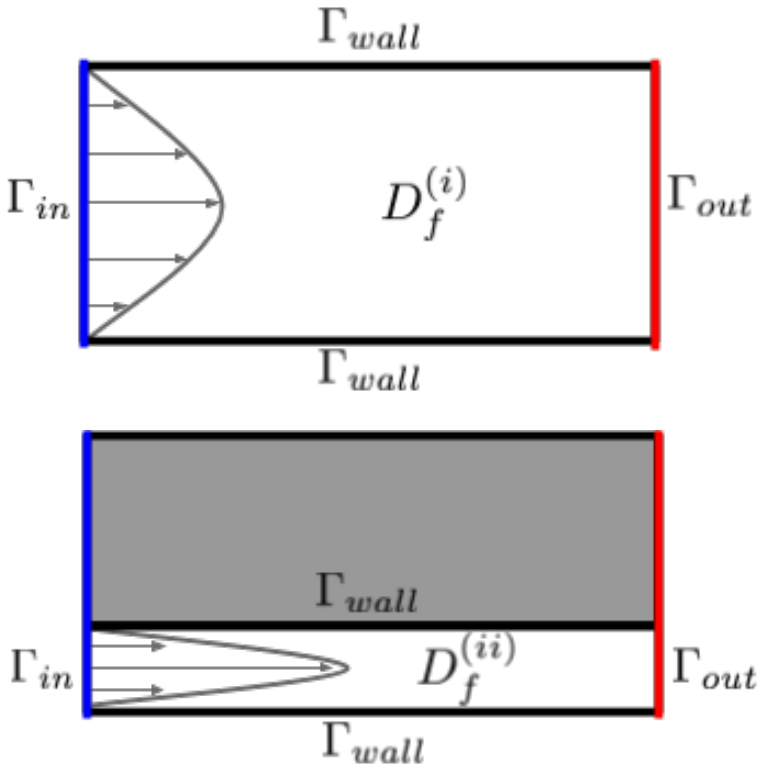

FIGURE 3.10: Flow domains $D_f^{(i)}$ and $D_f^{(ii)}$, and an illustration of the flow solutions for Example 3.3.1.

Example 3.3.1. Consider Hagen-Poiseuille flow in $D_f \subseteq D = [0,2] \times [0,1]$. We find analytical solutions for two cases, (i) and (ii), and denote the varying conditions and solutions with a superscript (i) or (ii).

Hagen-Poiseuille flow describes Stokes flow (3.1.1) in a channel with parabolic inflow. We use boundary conditions (3.1.2), where Γ_{in} is the left boundary, Γ_{wall} imposes the no-slip condition on the top and bottom boundaries, and Γ_{out} is the right boundary. Let $\mu = 1$. The velocity solution is identical to the inflow propagated forward through the domain, with solution given by (3.1.3). See Figure 3.10 for an illustration of the domains and flow solutions.

(i) Let the flow domain be $D_f^{(i)} = D$, so $\phi_{\Gamma_{in}^{(i)}} = 1$. Set $u_D^{(i)}(x,y) = y(1-y)$.

The average velocity at the inflow is

$$\langle u_D^{(i)} \rangle_{\Gamma_{in}^{(ii)}} = \frac{1}{6}.$$

When considered as an average over the domain D we have

$$\phi_{\Gamma_{in}^{(i)}} \langle u_D^{(i)} \rangle_{\Gamma_{in}^{(i)}} = \frac{1}{6}.$$

Since the solution is constant in x, we have

$$U^a = \frac{1}{6}. \tag{3.3.5}$$

(ii) Let the flow domain be $D_f^{(ii)} = [0, 0.2] \times [0, 1]$, so $\phi_{\Gamma_{in}^{(ii)}} = 0.2$. Set $u_D^{(ii)}(x, y) = 125y(0.2 - y)$.

The average velocity at the inflow is

$$\langle u_D^{(ii)} \rangle_{\Gamma_{in}^{(ii)}} = \frac{5}{6}.$$

When considered as an average over the domain D, we have

$$\phi_{\Gamma_{in}^{(ii)}} \langle u_D^{(ii)} \rangle_{\Gamma_{in}^{(ii)}} = \frac{1}{6}.$$

Since the solution is constant in x, we have

$$U^{(ii)} = \frac{1}{6}. \tag{3.3.6}$$

We see by (3.3.5) and (3.3.6) that $U^{(i)} = U^{(ii)}$. That is the average velocity over D is the same, despite different fluid speeds in D_f.

Lemma 3.3.1 is important to the upscaling efforts in the following way. We are investigating how pore scale geometry changes impact the upscaled permeability. The upscaling method to find permeability, K, in section 3.3.1 has two degrees of freedom, ∇P and $U = \langle u \rangle_{D^*}$. We remind the reader that $D^* \subsetneq D$ is a subset such that the boundaries of D^* are away from the boundaries of D, but D^* is sufficiently large to capture the flow characteristics of D. By fixing the inflow conditions we have removed one degree of freedom, thus the value of K is dependent only on ∇P. Now, that isn't quite true, as $D^* \subsetneq D$, but then the only change in U from one experiment to the next is what part of the flow exists in the subset domain. The impact of that has not been determined.

In some cases it may make sense to have the Darcy flux U incorporate the tortuosity $\mathbf{T}$. As explained in [12], if the Darcy flux is to remain constant while the fluid path length increases, then the interstitial velocity must increase. The authors derive the following modification to Dupuit's relation (3.3.2),

$$U = \langle u \rangle_{D_f} \phi \mathbf{T}^{-1}. \tag{3.3.7}$$

Our results will make use of both (3.3.2) and (3.3.7).

3.4 Numerical methods for flow

In this section we describe how to approximate numerical solutions to the immersed boundary Stokes flow model (3.1.7), Stokes flow (3.1.1), and Darcy flow (3.1.4). The Darcy flow solutions are calculated from the pore scale solutions via numerical homogenization, as previously presented in Section 3.3.1.

The numerical approximation techniques for flow problems can be roughly divided into the classes of finite element techniques, finite differences, and finite volumes. Each class has its advantages and disadvantages. Finite element methods can provide very accurate approximations on complex geometries, but for the viscous flow problems require care in the choice of the approximating spaces; in addition, may not necessarily provide mass conservative velocity solutions. Finite volume methods and some finite difference methods can be quite robust, stable, and mass conservative but are not highly accurate. In addition, working in complex pore scale geometries is challenging in itself. Detailed discussion of these approximation techniques is outside the scope of this work, as they are used only as a tool. Nevertheless we provide some information on the challenges to the use of these techniques when applied to the flow simulations at the pore scale.

In Section 3.4.1 we overview some open finite element solvers that can be used to solve flow. In Section 3.4.2 we describe the importance of having mass conservative flow for use in transport simulations. In Section 3.4.3 we describe a method for correcting mass conservation of flow solutions. In Section 3.4.4 we discuss HybGe-Flow3D [14], which we use to solve (3.1.1) and (3.1.7).

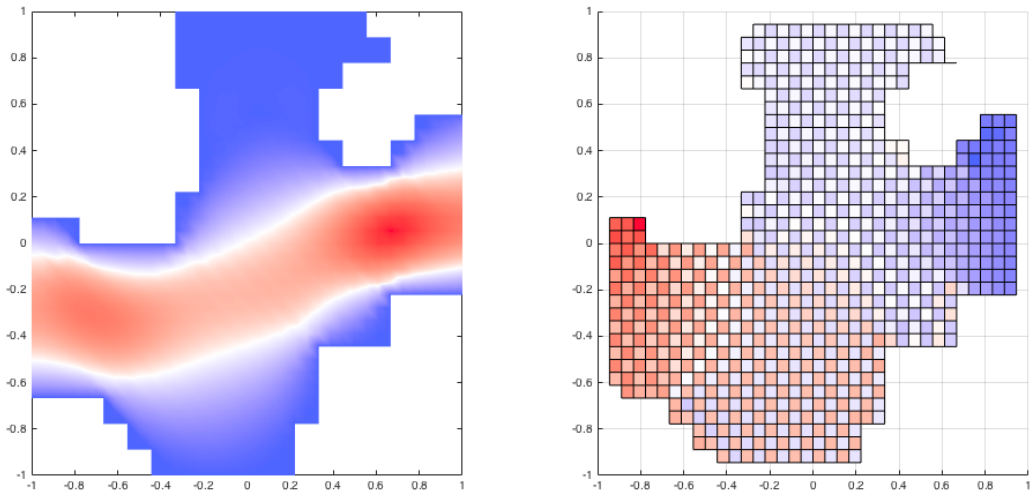

FIGURE 3.11: Stokes flow solution with classical checkerboard instabilities in pressure. Left: velocity magnitude. Right: pressure.

3.4.1 Finite element flow solvers

Solving Stokes equation with mixed Finite Elements requires using stable element pairs [19, Ch. 3.3]. One classical problem with an unstable element pair of finite element spaces occurs with the approximation spaces of bilinear velocities and piecewise constant pressures. In particular, one can get velocity solutions that seem reasonable, but with a checkerboard pattern in the pressure solution. This issue requires a correction, i.e., stabilization. Detailed description is outside the scope of this work, but we provide an example in Figure 3.11 where Stokes flow has been solved in a single pore model with IFISS [19].

Assuming now that the flow solution was obtained in stable manner, for example with bilinear velocities and a scheme which is stabilized, additional difficulty arises when attempting to use that scheme in a transport scheme approximating, e.g, (3.2.4). With Finite Elements there is no direct method for using the flow solution u directly for transport. For example, bilinear velocities would have nodal solutions at the corners of the cells, while a transport scheme would require it at the midpoints of the cell edges. This is known as incompatibility between the numerical methods, a broader topics outside our scope. A quick technique to fix this problem is to interpolate the

velocity from the finite element solution to provide the approximate velocities at the degrees of freedom required for the transport scheme.

This solution creates another difficulty however in that the obtained velocity is not mass conservative, i.e., it does not satisfy $\nabla \cdot u = 0$. We discuss how to handle this in what follows.

3.4.2 Mass conservation of flow solutions

It is well known that a particular numerical flow solution will may not be appropriate for transport [16]. Small errors in satisfying conservation of mass, (3.1.1b) or (3.1.4b), can cascade into problems in the approximation of transport. When using a non-conservative velocity field for transport one would see non-physical creation and/or destruction of the solute being transported.

The consequences of using non-conservative flow solutions for transport are exhibited, e.g., in [16]. Consider the one dimensional transport equation

$$c_t + (uc)_x = 0, \ (x,t) \in D \times (0,T], \tag{3.4.1}$$

with $u = 1$. Let $U \approx u$ be the approximation to u, with $U = 1 + 0.05\cos(20\pi x)$. Then U has 5% error approximating u, but $-\pi \leq U_x \leq \pi$. If one approximates (3.4.1) with an upwind scheme which assumes that the velocity is divergence free, and velocity U, then the approximation to the solution $c(x,t)$ is oscillatory and violates the maximum principle.

The remedy to this problem is to either implement a special transport scheme or to use post processing to approximate the flux across the cell faces. Another solution is to make a correction to U so it would be mass conservative. This technique was implemented very successfully in large scale ocean circulation models coupled to contaminant transport [11]. Our first experience with this technique is described in [53] for a velocity field interpolated from data. We describe this technique below.

3.4.3 Mass conservation correction

One way to project Finite Element flow solutions for mass conservative flow is presented in [11], which we adapt to the pore scale simulations. The method is as follows. Let u be the Finite Element flow solution to Stokes flow (3.1.1) on domain D_f. Partition the domain boundary as $\partial D_f = \Gamma_D \cup \Gamma_N$, where $\Gamma_D = \Gamma_{wall} \cup \Gamma_{in}$, $\Gamma_N = \Gamma_{out}$, the note that $\Gamma_D \cap \Gamma_N = \emptyset$. Let $u \cdot n = g(x)$ on Γ_D.

We calculate $\mathcal{P}u$, the flow solution on the cell edge recovered from u. This can be done by injection, interpolation, projection, etc. We want to find an approximation $\hat{u} \approx \mathcal{P}u$, such that the approximation satisfies mass conservation and matches the Dirichlet boundary condition,

$$\begin{cases} \nabla \cdot \hat{u} = 0, & \text{on } D_f, \quad (3.4.2a) \\ \hat{u} \cdot n = g, & \text{on } \Gamma_D. \quad (3.4.2b) \end{cases}$$

Define the approximation to be the original projected velocities with some correction,

$$\hat{u} = \mathcal{P}u + \gamma. \quad (3.4.3)$$

Combine (3.4.2) and (3.4.3), to get the problem

$$\begin{cases} \nabla \cdot \gamma = -\nabla \cdot \mathcal{P}u, & \text{on } D_f, \quad (3.4.4a) \\ \gamma \cdot n = g - \mathcal{P}u \cdot n = \tilde{g}, & \text{on } \Gamma_D. \quad (3.4.4b) \end{cases}$$

Assume that $\gamma = -\nabla\phi$, where ϕ is a pseudo-pressure. Assume that $\phi = 0$ on Γ_N. Then we can write the elliptic problem

$$\begin{cases} -\Delta\phi = -\nabla \cdot \mathcal{P}u, & \text{on } D_f, \quad (3.4.5a) \\ -\nabla\phi \cdot n = \tilde{g}, & \text{on } \Gamma_D, \quad (3.4.5b) \\ \phi = 0 & \text{on } \Gamma_N. \quad (3.4.5c) \end{cases}$$

Then, one solves (3.4.5) to get the correction term γ. We solve (3.4.5) with the cell centered finite difference scheme described in Section 2.4.2.

In Figure 3.12 we exhibit the pitfall of using a non-conservative velocity field for transport and the value of correcting that velocity field for conservation. We solve the

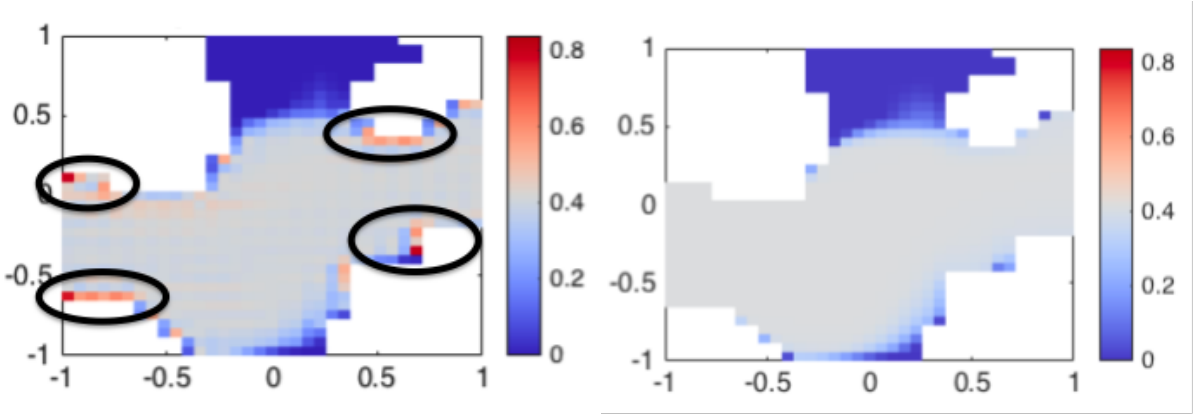

(a) (b)

FIGURE 3.12: Solutions to (3.4.6) with (a) non-conservative velocity approximation U and (b) conservative velocity approximation $\hat{U}$. Note the red voxels (circled in some instances) in (a), these are instances of overshoot, i.e. non-physical creation of solute c that violates the maximum principle. We see no such instances in (b).

system

$$\begin{cases} c_t + \nabla \cdot (uc) = 0, & \text{in } D_f, \quad (3.4.6a) \\ c(x,0) = 0, & \text{in } D_f, \quad (3.4.6b) \\ c(x,d) = c_d, & \text{on } \Gamma. \quad (3.4.6c) \end{cases}$$

We present solutions with velocity approximations $U \approx u$, where U is non-conservative, and $\hat{U} \approx U$, where $\hat{U}$ is found via the method described above so that $\nabla \cdot \hat{U} = 0$. Solutions are shown at arbitrary time T.

3.4.4 HybGe-Flow3d method for Stokes flow

A well known finite volume scheme which is stable and mass conservative is the MAC scheme [34]. The scheme resembles the cell-centered Darcy scale flow solver described in Section 2.4.2.

An extension of this scheme was developed in [13, 15] to solve the Stokes flow problem with permeable obstructions. Without the obstructions, it simply solves the Stokes flow problem. To solve Stokes flow we use HybGe-Flow3D [14]. HybGe-Flow3d uses a well known staggered grid finite volume method [15, 55]. This approach defines

pressures at cell centers and velocities at cell edges. This inherently mass conservative method is a natural choice when using the velocity field for transport.

Our description of HybGe-Flow3D follows [13]. The domain D_f is discretized into uniform rectangular cells. Write (3.1.1) as follows,

$$\begin{cases} -\mu\Delta u_1 + \partial_{x_1} p = f_1, & \text{in } D_f \quad (3.4.7a) \\ -\mu\Delta u_2 + \partial_{x_2} p = f_2, & \text{in } D_f \quad (3.4.7b) \\ -\mu\Delta u_3 + \partial_{x_3} p = f_3, & \text{in } D_f \quad (3.4.7c) \\ \partial_{x_1} u_1 + \partial_{x_2} u_2 + \partial_{x_3} u_3 = 0. & (3.4.7d) \end{cases}$$

Each of the equations in (3.4.7) is discretized independently, following the staggered grid method. The discretization of (3.4.7) gives a saddle-point system that is solved iteratively. The iterative solvers implemented in HybGe-Flow3D include two Krylov subspace methods, the Conjugate Gradient Method (CG) and the Generalized Minimum Residual Method (GMRES).

3.5 Numerical methods for transport

In this section we describe our numerical schemes for both Eulerian and Lagrangian transport. The methods used in the section were chosen due to ease of implementation, as this work is a proof of concept. As such, the methods employed are both first order accurate methods. We point to examples of higher order methods that could be implemented to improve the accuracy.

We also describe how we calculate breakthrough curves for the transport. Lastly, we discuss tortuosity and how it follows from the approximations of the Lagrangian streamlines.

3.5.1 Eulerian advective transport

To solve the advection equation (3.2.4) in the Eulerian frame of reference we use a simple Finite Volume upwind scheme. We implement Godunov's method, following [25]. This explicit in time method is stable for a Courant-Friedrichs–Lewy (CFL) number up

to $1/2$ in $d = 2$.

The CFL condition states that a numerical method can be convergent only if its numerical domain of dependence contains the true domain of dependence of the PDE, at least in the limit as τ and h go to zero [25].

We develop the method with $d = 2$ and uniform step size h. In (3.2.4a), c is a scalar conserved quantity and velocity is (u, v). Identify flux functions in the x and y directions as $f(c)$ and $g(c)$ respectively. Expand the terms in (3.2.4a) as follows

$$c_t + \nabla \cdot ((u, v)c) = c_t + (uc)_x + (vc)_y = c_t + f(c)_x + g(c)_x. \tag{3.5.1}$$

Combine (3.5.1) and (3.2.4) to write

$$c_t = -f(c)_x - g(c)_y. \tag{3.5.2}$$

Integrate (3.5.2) on grid cell $\mathcal{C}_{ij}$ to get the integral form of the conservation law,

$$\begin{aligned}\frac{d}{dt}\iint_{C_{ij}} c(x,y,t) &= -\iint_{C_{ij}} f(c(x,y,t))_x - \iint_{C_{ij}} g(c(x,y,t))_y \\ &= \int_{y_{j-1/2}}^{y_{j+1/2}} f(c(x_{i-1/2},y,t)) - \int_{y_{j-1/2}}^{y_{j+1/2}} f(c(x_{i+1/2},y,t)) \\ &\quad + \int_{x_{i-1/2}}^{x_{i+1/2}} g(c(x,y_{j-1/2},t)) - \int_{x_{i-1/2}}^{x_{i+1/2}} g(c(x,y_{j+1/2},t)).\end{aligned} \tag{3.5.3}$$

We denote flux approximations across cell edges as follows

$$\begin{aligned}F^n_{i-1/2,j} &\approx \frac{1}{\tau h}\int_{t_n}^{t_{n+1}}\int_{y_{j-1/2}}^{y_{j+1/2}} f(c(x_{i-1/2},y,t)), \\ G^n_{i,j-1/2} &\approx \frac{1}{\tau h}\int_{t_n}^{t_{n+1}}\int_{x_{i-1/2}}^{x_{i+1/2}} g(c(x,y_{j-1/2},t)).\end{aligned}$$

Define cell average c^n_{ij} at time t_n as follows

$$\rfloor^n_{ij} = \iint_{\mathcal{C}_{ij}} c(x,y,t_n).$$

Integrate (3.5.3) in time and divide by cell size h^2 to get the fully discrete flux difference method as follows

$$c^{n+1}_{ij} = c^n_{ij} - \frac{\tau}{h}\left[F^n_{i+1/2,j} - F^n_{i-1/2,j}\right] - \frac{\tau}{h}\left[G^n_{i,j+1/2} - G^n_{i,j-1/2}\right]. \tag{3.5.4}$$

We use the upwind flux approximations

$$F^n_{i-1/2,j} = \begin{cases} u_{i-1/2,j}c^n_{i,j}, & u_{i-1/2,j} \leq 0, \quad (3.5.5a) \\ u_{i-1/2,j}c^n_{i-1,j}, & u_{i-1/2,j} > 0, \quad (3.5.5b) \end{cases}$$

and

$$G^n_{i,j-1/2} = \begin{cases} v_{i,j-1/2}c^n_{i,j}, & v_{i,j-1/2} \leq 0, \quad (3.5.6a) \\ v_{i,j-1/2}c^n_{i,j-1}, & v_{i,j-1/2} > 0. \quad (3.5.6b) \end{cases}$$

Using fluxes (3.5.5) and (3.5.6) is also known as the first-order accurate donor-cell upwind (DCU) method [25] The DCU method is only stable for τ such that

$$\left|\frac{u\tau}{h}\right| + \left|\frac{v\tau}{h}\right| \leq 1. \quad (3.5.7)$$

3.5.2 Lagrangian advective transport

Solving advection in the Lagrangian frame of reference follows the streamlines for the flow. The equations we need to solve come from the method of characteristics. Combine the pore scale advection equation (3.2.4a) with the divergence free condition, $\nabla \cdot (u, v) = 0$, to get

$$c_t + \nabla \cdot ((u, v)c) = c_t + uc_x + vc_y = 0.$$

By the method of characteristics, we solve the following system of ordinary differential equations,

$$\begin{cases} \dfrac{dt}{d\tau} = 1, & (3.5.8a) \\ \dfrac{dx}{d\tau} = u(x), & (3.5.8b) \\ \dfrac{dy}{d\tau} = v(x), & (3.5.8c) \\ \dfrac{dc}{d\tau} = 0. & (3.5.8d) \end{cases}$$

Now, $c(x, t)$ is constant along streamlines, so for any given $c(x, 0) = c_0(x)$ we calculate the path given by (3.5.8b) and (3.5.8c) with the one-step forward Euler method.

We follow the forward Euler method as in [26]. For (3.5.8b) with time step τ, the method is

$$x^{n+1} = x^n + \tau u^n(x^n).$$

The numerical velocity solutions are given on cell edges. To approximate velocities for arbitrary point x, we use linear interpolation of cell edge velocities. For $x \in \mathcal{C}_{ij}$, the approximation is as follows,

$$u^n(x) \approx \frac{x_{i+1/2,j} - x}{h} u^n_{i-1/2,j} + \frac{x - x_{i-1/2,j}}{h} u^n_{i+1/2,j},$$
$$v^n(y) \approx \frac{y_{i,j+1/2} - y}{h} v^n_{i,j-1/2} + \frac{y - y_{i,j-1/2}}{h} v^n_{i,j+1/2}.$$

While the method of characteristics is exact, the solution obtained with the technique described here is only first order accurate due to low order time integration. As mentioned, c is constant along streamlines. The value for c is set at the inlet by boundary condition (3.2.4c), then propagated according the streamline calculated.

This method could be improved by using a more stable or higher order multi-stage method, such as from the Runge-Kutta family. We briefly describe Runge-Kutta methods as in [25]. Runge-Kutta methods are explicit methods for ordinary differential equations that generate intermediate values to construct higher order approximations. For example, a second-order accurate method for (3.5.8b) would be

$$x^* = x^n + \frac{\tau}{2} u^n(x^n),$$
$$x^{n+1} = x^n + \tau u^n(x^*).$$

3.5.3 Breakthrough curves

The breakthrough curve we use most often is (3.2.7),

$$B(t) = \int_{\Gamma_{out}} c(x,t). \tag{3.5.9}$$

We approximate (3.5.9) at pore scale in both the Lagrangian and Eulerian frame of reference.

First, consider the Lagrangian frame of reference. As described in Section 3.5.2, this method calculates streamlines. All streamlines begin at the inlet, Γ_{in} and end at the outlet Γ_{out}. Let $i = 1, \ldots, N$ be the index of N streamlines. We assume that the boundary condition $c = c_D \in \mathbb{R}$ on Γ_{in} is constant. Let $D = [a,b] \times [c,d]$, so that $\Gamma_{out} = \{(x,y) : x = b\}$. Let $\xi^n_i = (x^n_i, y^n_i)$ be the position of the front of streamline i

at time n, where $(x_i^0, y_i^0) = (0, y_i^0)$ for all streamlines. Let $\Xi^n = \{\xi_i^n : x^n \geq b\}$. Then we approximate (3.2.7) by summing the number of streamlines that have reached the outlet,

$$B(t^n) \approx \sum_{\Xi^n} c_D. \tag{3.5.10}$$

Next, consider the Eulerian frame of reference. Let $\mathcal{C}_{M,j}$ be the cells bordering the outlet of D discretized into $M \times N$ cells.

Since we don't have the values of c on the cell edges, we use the cell averages found by the DCU scheme. To calculate the breakthrough value we use the approximation

$$B(t^n) \approx \sum_{j=1}^{N} c_{Mj}^n. \tag{3.5.11}$$

3.6 Numerical method for tortuosity

In this last section we describe our method for calculating tortuosity $\mathbf{T}$.

To determine the tortuosity (3.1.8) of a macro scale domain $D = [a, b] \times [c, d]$ we average the effective path lengths for flow through the associated pore scale domain D_f, which we normalize by the length of D.

To find the length of a streamline, we use the Lagrangian advective transport solution as described in Section 3.5.2. The path of streamline (i) is given by (x_i^n, y_i^n), $n = 0, \ldots, N_T$. The length l_{eh} of streamline (i) is estimated by

$$l_{eh}^i \approx \sum_{n=0}^{N_T-1} ||\xi_i^{n+1} - \xi_i^n||_{l^2} = \sum_{n=0}^{N_T-1} \sqrt{(x_i^{n+1} - x_i^n)^2 + (y_i^{n+1} - y_i^n)^2}.$$

Then, we average the lengths of the streamlines $i = 1, \ldots, N$,

$$l_{eh} \approx \frac{1}{N} \sum_{i=1}^{N} l_{eh}^i.$$

Lastly, we normalize by the length of D. In the case of flow in the direction of the first dimension, we have

$$\mathbf{T} = \frac{l_{eh}}{b - a}.$$

4 Motivation and tools used to generate pore geometries with pore filling and pore coating obstructions

In this chapter we introduce two methods for generating physically realistic pore scale obstructions in porous media. The first method we introduce is an extension of a phase separation model based on the Allen-Cahn equation subject to constraints. The second method is a Markov chain Monte Carlo method, inspired by the Ising model.

Both methods are designed to generate not just one, but multiple independent realizations of the geometries at pore scale. The first method finds local minima of a functional which is not convex. These minimizers are reached from different initial guesses or initial conditions. The second method is probabilistic and is well known to generate multiple final states.

Motivation. As discussed in Chapter 3, Darcy scale properties of a porous media, such as permeability, porosity and tortuosity, are highly dependent on the pore scale geometry. As the pore scale geometry changes, so will the aforementioned Darcy scale properties.

Below, we review methods several many approaches to finding how the Darcy properties change when the geometry changes due to chemical processes at the micro scale.

Literature review. (A) First, one can study the problem experimentally, and measure the properties at Darcy scale only, while subjecting the medium to some given chemical process.

(B) The second method provides measures of the Darcy scale properties accompanied by detailed information about the geometry by designing an experiment and imaging the media while the process is ongoing. For example, in [10] the authors use experiment to study hydrate formation. The authors find evidence of Ostwald ripening of gas hydrate crystals in pores and porous media. Ostwald ripening is a process through which small hydrate particles nucleate, then combine to form larger crystal structures. At high hydrate saturations this ripening process leads to grain-cementing and reduced

permeability.

However, there are difficulties associated with those methods for studying pore scale geometry changes. First, they can be costly and time consuming. Experiments to grow hydrates require cryochambers kept at very high pressures and low temperatures, possibly running for months [10]. Experiments to grow biofilms can't be imaged in situ, as the biofilm needs to be killed for imaging [35].

In addition, the imaging process for experiments is a hard problem in it's own right. The density of biofilm is only slightly higher than that of water, making it difficult to distinguish the obstruction from the void space [35]. For the experiments in [10] xenon is substituted for methane in the hydrate formation because xenon has an X-ray mass attenuation coefficient one order of magnitude higher than methane, making it easier to image.

(C) The third method utilizes computations, conducting direct numerical simulations (DNS) of the process at the pore scale, accompanied by upscaling of the properties to Darcy scale. In particular, in [54] the authors consider crystal dissolution and precipitation in a thin strip at pore scale. The authors work in 1D, establishing the existence and uniqueness of solutions to their model, while accounting for how the pore geometry changes due to dissolution and precipitation.

In [35] the authors combine experiment with DNS of biofilm growth in porous media. The numerical model incorporates an advection-diffusion-reaction model, for the biofilm and nutrients, coupled to a Navier-Stokes system for the hydrodynamics. The use of DNS is very appealing because they seem to connect the connect the computational models to physical reality. Unfortunately, the use of DNS is also very complex. Simulations for realistic problems include evolving 3D geometries with the numbers of voxels on the order of 10,000,000, and an appropriately larger number of unknowns. Full transient studies with such simulations and multiple parameters are unfeasible [15]. Finally, any DNS simulation of flow and transport requires some initial geometry and initial conditions which are plagued with large uncertainty, thus would require additional stochastic simulations. Rephrasing, DNS give very specific answers for what may

be a very non-specific question, and is extremely complex.

Approach to generation of pore scale geometries obstructions proposed in this work. In this work we propose the fourth approach (D) of generating multiple realizations of the process of formation of obstructions using computational simulations. Our simulations are not based on first principles, yet we generate geometries similar to those found by x-ray imaging. The advantage of our approach over DNS is that it is fast and does not require that we know or are able to calibrate the exact coefficients for the complex process underlying the formation of obstructions.

One of the advantages of our methods is that they are computationally cheap and easy to run. The methods are designed to quickly find a realistic obstruction representation starting from some initial random configuration. When run multiple times, we find as many independent realizations as desired.

Furthermore, each of the two methods proposed has a few parameters that can be tuned to account for different obstruction characteristics. Currently, the parameters are set by hand based on heuristics. These heuristics are based on our intuition and the visual observation of images from the literature.

In particular, we consider two specific processes which lead to the so called "pore filling" or "pore coating" behavior. In the first, typical for hydrate crystal formation, the obstructions made by crystals form in the void space rather than at the walls. One could say colloquially that the hydrates "avoid the solid matrix". Such behavior is seen, e.g., in the experiments in [56].

On the other hand, the latter, "pore coating" is the behavior when the obstructions such as biofilms cling to the solid matrix. See, e.g., the experimental work reported in [35].

The methods we propose can easily account for these two different behaviors.

Last but not least, in the future our models can be coupled with a flow solver to model how flow changes as the hydrate or biofilm aggregate. The phase separation method in Chapter 5 generates obstructions with smooth boundaries, and it could also be coupled to the Lattice model presented in Chapter 6 to smooth the obstructions.

The outline of this section is as follows. In Section 4.1 we describe why we study pore filling and pore coating obstructions. In particular, we describe how biofilm and hydrate meet those descriptions and what impacts they have on porous media flow and transport. In Section 4.2 we present background literature relevant to the CLPS model we develop in the next chapter.

4.1 Motivation behind the need for generation of geometries with pore filling and pore coating obstructions

4.1.1 Pore filling obstructions: hydrate crystals

In this section we describe why we study hydrate. Clathrate hydrate is a crystal lattice comprised of frozen water cages trapping gas molecules [10]. Our particular interest is in methane hydrate is when the trapped gas is methane.

This naturally-occurring and highly-concentrated form of methane holds significant quantities of carbon in the global system. Methane hydrate formation occurs in areas of low temperature and high pressure making them abundant in permafrost and marine sediments, which are estimated to contain 2×10^3 to 4×10^6 Gt of carbon [10]. Such a large quantity of carbon makes methane hydrates a energy source [8] and potential climate change accelerant [42]. It is possible for ocean and atmospheric warming to perturb hydrate stability, leading to the release of the trapped methane. The released methane may reach the atmosphere, exacerbating global warming. Methane has a Global warming Potential of 25, meaning that pound for pound, methane emissions are estimated to absorb 25 times the energy of carbon dioxide emissions [50].

Since methane and methane hydrate are important for various reasons, scientists attempt to probe the subsea and arctic sediments to detect their presence and to predict their evolution. The formation of hydrate has been shown to influence the porous media in many significant ways, and these make observations and experiments at large scale difficult. In particular, this includes impact of hydrate presence on the seismic velocities [23], permeability [24], strength [29], thermal conductivity [22] and electrical properties

[51].

Therefore, laboratory studies and imaging are undertaken to study the evolution of hydrate crystals in small laboratory samples. In [10] the authors note that the transport and mechanical properties of hydrate bearing sediments are dependent upon the spatial distribution and shape of the hydrates, but that the evolution of hydrate shape and spatial distribution are not yet well understood. In [10] the authors complete physical experiments followed by x-ray imaging to help fill that knowledge gap.

The three experiments in [10] are (i) xenon hydrate growth in water and gas phases without porous media, (ii) methane hydrate growth on water droplets, and (iii) xenon hydrate growth in wet sandpack. Xenon is used as a substitute for methane to improve the imaging process of the experiments. High-resolution CT images and photos of the experiments are available in digital rocks portal [39].

The work of [10] provides experimental evidence of Ostwald ripening of gas hydrates in large pores and in a sand pack. The hydrate growth rate is shown to depend on both overpressurization and undercooling. As the ripening occurs the hydrates become pore-filling which has causes significant changes to the permeability and sediment strength. At sufficiently high saturation levels the hydrates become grain cementing.

Relation to our work.

In this work we develop models which can be applied to the goal of obtaining physically realistic pore scale geometries containing hydrate crystals so that Darcy scale properties such as permeability or tortuosity can be studied. In particular, our CLPS model captures the Ostwald ripening evolutionary process of hydrate formation and simulates hydrate shape and distribution within an REV. Specifically, one could use our model to reproduce geometries similar to those in experiment (iii) of [10] as follows.

(1) Starting with the images of the wet sandpack, extract a suitable REV to be used with the CLPS model and use it as the pore domain D. (2) Tune the parameters of the CLPS model such that the obstructions formed are similar to those imaged in the experiment. (3) With the parameters fixed, create many realizations of obstructed geometries. (4) For each realization of geometry from the family found in (3) calculate

permeability, tortuosity, etc.

4.1.2 Pore coating obstructions: biofilm

In this section we describe biofilms and why we study them. By biofilm we refer to the microorganisms growing in porous media which form a special extracellular polymer substance called EPS of high density which is impermeable or almost impermeable to the external flow. EPS protects the microbes but clogs the pore void space. As with the formation of hydrate crystals, excessive growth of biofilm impacts the flow and transport properties of porous media.

In particular, a reduction in hydraulic conductivity due to biofilm clogging porous media has been shown to have significant impacts on the following topics. In [32] the authors show that biofilm growth would be expected to have a major effect on contaminant transport when proper conditions for growth exist. In [4] the authors evaluate biofilm growth models in the context of enhancing in situ bioremediation of contaminated aquifers. In [33] the authors study biological clogging during the artificial recharge of underground storage. In [49] the authors simulate the progressive clogging of a septic bed, showing how the biofilm initially forms at the up-gradient end of the flow displacing wastewater infiltration.

The importance of determining the Darcy scale properties of porous media containing the evolving biofilm calls for laboratory experiments combined with x-ray imaging. In particular, in [35] the authors combine experiment with direct numerical simulation of biofilm growth in porous media. The authors note that the biofilm growth depends on various environmental conditions, in particular on the flow rate. The experimental dataset is based on a glass bead domain inoculated by biomass. The imaging data is incorporated directly by a computational model for flow and transport , i.e., a DNS model. Next, upscaling such as described in Section 3 is used to determine the Darcy scale properties after biofilm growth. The computational model found good agreement with the properties measured from the physical experiment.

Relation to this work.

The complexity of the DNS simulations in [35] is enormous. Furthermore, the results depend significantly on the local pore geometry, on the physical parameters assumed, as well as on the initial conditions representing the inoculation with microbes. In other words, there might be large uncertainty as to the actual results.

The methods proposed in this work could be used instead of such DNS models and generating plausible realizations of geometries directly. This would would not contradict the apparent uncertainty of DNS but rather directly support it. Our CLPS and Lattice models can be used to enhance the link between the physical and computational experiments in [35].

Furthermore, the models proposed in this paper could be used to generate a set of physically plausible random initial conditions for the DNS model.

4.2 Literature background on CLPS models

In this work we consider two classes of models we call CLPS and Lattice. The bulk of the thesis is spent on the model called CLPS, which extends Allen-Cahn equation. In this section we review some work relevant to our CLPS model and provide context to some of our design decisions. Background on Lattice models is provided in Chapter 6 where they are introduced.

In Section 4.2.1 we introduce the Allen-Cahn equation. In Section 4.2.2 we review [18] to show known challenges for equations such as Allen-Cahn. In Section 4.2.3 we review [45] to recall the error bounds for numerical approximations to the Allen-Cahn equation. In Section 4.2.4 we review [41] to introduce adding a phase conservation constraint to the Allen-Cahn equation.

4.2.1 Allen-Cahn equation

Let $D \in \mathbb{R}^d$, $d = 2,\ 3$ be a bounded domain, n be the outward normal, and $f(u) = W'(u)$, with W being a given energy potential, such as the double well potential

$W(u) = (1-u^2)^2$. The Allen-Cahn equation is

$$\begin{cases} u_t - \Delta u + \dfrac{1}{\epsilon^2} f(u) = 0, & x \in D,\, t > 0, \quad (4.2.1a) \\ \nabla u \cdot n = 0, & x \in \partial D,\ t > 0, \quad (4.2.1b) \\ u(x,0) = u_0(x), & x \in D, \quad (4.2.1c) \end{cases}$$

Here u represents the concentration of one of two phases and ϵ represents the interfacial width. We note that in other work the parameter is applied differently as $u_t - \epsilon\Delta u + \frac{1}{\epsilon} f(u) = 0$; the difference in the two equations amounts to a scaling of time. The characteristic length of the domain is much larger than ϵ. These equations describe the evolution and separation of the two phases. The two phases are represented as the state where $u = 1$ or where $u = -1$. The equilibrium states are separated by a region of width proportional to ϵ called the diffuse interface region.

As shown in [18], (4.2.1) describes the gradient flow of the Liapunov energy functional

$$J(u) := \int_D \left(\frac{1}{2} |\nabla u|^2 + \frac{1}{\epsilon^2} W(u) \right). \quad (4.2.2)$$

Another classic phase separation model is the Cahn-Hilliard equation [9]. Similar to the Allen-Cahn equation, the Cahn-Hilliard equation is a gradient flow for (4.2.2), however it also satisfies phase conservation but is fourth order. We choose to not work with the fourth order Cahn-Hilliard equation, but rather enforce phase conservation on the Allen-Cahn equation as explained starting in Section 4.2.4.

4.2.2 Dynamics of semilinear parabolic equations

In [18] the authors consider the following semilinear parabolic initial value problem

$$\begin{cases} u_t - \Delta u + f(u) = 0, & x \in D,\, t > 0, \quad (4.2.3a) \\ u = 0, & x \in \partial D,\, t \geq 0, \quad (4.2.3b) \\ u(x,0) = u_{init}(x), & x \in D. \quad (4.2.3c) \end{cases}$$

This is the Allen-Cahn equation introduced in the previous section, with $\epsilon = 1$ and homogenous Dirichlet boundary conditions. The authors assume that $D \in \mathbb{R}^d$ and $d \leq 3$ is bounded with Lipschitz boundary ∂D. Further, assume that the initial condition

$u_{init} \in K = \{\eta \in L^2(D) : ||\eta||_\infty \leq M\}$. Finally, assume that the nonlinear function f satisfies the following properties

$$f \in C^2,$$
$$f(0) = 0,$$
$$\text{There exists } u > 0, \text{ such that } f(r)/r > 0 \text{ for any } r > u,$$
$$W''(u) \geq -C_F,$$

where

$$W(u) = \int f(u),$$

and $C_F > 0$.

The authors results are broad, but we present only those relevant to this work. First, for each $u_{init} \in K$, there exists a unique solution to (4.2.3) which satisfies for all $T > 0$

$$u \in L^2(0, T; H_0^1(D)) \cap C[0, T; L^2(D)].$$

The mapping $u_0 \to u(t)$ is continuous for each $t > 0$. Thus, the solution operators $\{S(t)\}_{t\geq 0}$ defined by $S(t)u_0 := u(t)$ forms a continuous semigroup on $L^2(D)$.

Next, we have that the functional (4.2.2) with $\epsilon = 1$ is a Lyapunov functional for $\{S(t)\}_{t\geq 0}$. This means that solutions to (4.2.3) evolve towards solutions of the equilibrium problem

$$\begin{cases} -\Delta u + f(u) = 0, & x \in D, \quad (4.2.4a) \\ u = 0, & x \in \partial D. \quad (4.2.4b) \end{cases}$$

There is no uniqueness guaranteed for (4.2.4).

These results help to understand the gradient flow as the process towards finding the (multiple) equilibrium solutions for non-convex functionals.

In particular, the function known as double-well potential $W(u) = (1 - u^2)^2$ satisfies the properties above. Its derivative $f(u) = W'(u)$ is non-monotone, but $W''(u) \geq -4$. The function $f(u)$ in e.g., $u' + f(u) = 0$ provides the coarsening (phase separation) effect towards the stable equilibria $u = -1$, $u = 1$ and away from the unstable local minimum $u = 0$. The PDE with this function is known as Allen-Cahn

equation, it is also known as one of diffuse interface models or phase field or phase separation models. By design the solutions to these equations exhibit sharp gradients in certain regions; these regions have a particular width related to the particular parameters of the model. The sharp gradients arise due to a competition between the diffusive effects and nonlinear functions involved.

Relation to this work. In what follows we do not use the analysis in [18] directly. In fact, we use a function $W(u) = \frac{1}{4}u^2(u-1)^2$ with local minima at $u = 0$ and $u = 1$ and a local maximum at $u = 1/2$. Furthermore, we use Neumann boundary conditions as in Section 4.2.1, and we impose a constraint.

4.2.3 Numerical approximation of Allen-Cahn equation

Numerical solution of gradient flow problems such as Allen-Cahn equations is challenging, and the literature is abundant. Below we discuss the general challenges associated with the numerical approximation of gradient flow models and recall a few relevant results.

The first challenge is the presence of sharp fronts. These require fine spatial grid and small h. Second challenge is the strong nonlinearity. If explicit or semi-implicit methods are used for the nonlinear terms, this calls for small τ.

The second challenge is nonlinearity of the model. If fully implicit methods are used, one has to use a nonlinear solver such as Newton's iteration, and this approach may be very cumbersome. In turn, fully explicit methods with the stiff diffusion would require very small time steps. Therefore, various authors consider semi-implicit schemes where diffusion is treated implicitly but the nonlinear terms are treated explicitly. For these, one does not aim to obtain unconditional stability, but rather a particular form of stability in a specially chosen quantity of interest.

In particular, in [45] the authors develop energy stable numerical schemes with error bounds for solving the Allen-Cahn and Cahn-Hilliard equations. The analysis in that paper is done on the weak formulations, so that the results may be easily extended from the intended spectral methods.

We now give an example of a semi-implicit scheme for the Allen-Cahn equation. Consider the time discretized, first-order semi-implicit method applied to the weak form of (4.2.1)

$$\frac{\mathbb{U}^{n+1} - \mathbb{U}^n}{\tau} + A\mathbb{U}^{n+1} + \frac{1}{\epsilon^2}\mathbb{F}^n = 0. \tag{4.2.5}$$

By [45, Lemma 2.1], if $\tau \leq \frac{2\epsilon^2}{L}$, then the proposed scheme is energy stable with J as defined in (4.2.2), i.e.

$$J(u^{n+1}) \leq J(u^n), \ \forall n \geq 0,$$

provided various additional assumptions hold.

Because the estimates above are established in the weak form of the Allen-Cahn equation, they apply not only to the spectral-Galerkin method preferred by the authors, but also to Finite Element schemes. The stabilized first-order, semi-implicit scheme is a promising possibility for improvement on our methods. We do not plan on implementing the spectral-Galerkin method suggested by the authors in this paper and developed in detail in [44] due to the complex geometries of the REVs used in our simulations.

Relation to this work. We employ the same implicit-explicit method as described above to solve our CLPS model. We note that the CLPS model is different than the one considered above in that the CLPS model adds constraint. Refer to Section 2.4.4 for a description of the scheme implemented in this thesis.

4.2.4 Literature on nonlocal reaction-diffusion equations and nucleation

In [41] the authors consider a nonlocal reaction-diffusion equation for the phase separation of a binary mixture. Their work modifies the equations considered in Section 4.2.3 by incorporating phase conservation into the Allen-Cahn equation.

The phase conservation is incorporated as a constraint equation; this is done similarly to what we discussed in Section 2.3, even if our model development was done independently from [41]. We employ this same strategy for phase conservation in the development of the CLPS model in the following sections. We also recall the background material we developed in Examples 2.3.1 and 2.3.2.

Let $D \in \mathbb{R}^n$ be a smooth bounded domain with outward normal n and total volume $|D|$. Let $f = W'$, where W is the double well potential. Let $u : D \to \mathbb{R}$ be the order parameter and consider the system

$$\begin{cases} u_t - \Delta u + f(u) - \dfrac{1}{|D|}\displaystyle\int_D f(u) = 0, & x \in D,\ t > 0, \quad (4.2.6a) \\ \nabla u \cdot n = 0, & x \in \partial D, \quad (4.2.6b) \\ u(x,0) = u_{init}(x), & x \in D. \quad (4.2.6c) \end{cases}$$

One important characteristic of this system is that it conserves u. To see this, integrate (4.2.6a) over space and time to get the following

$$\int_0^t \int_D u_t - \int_0^t \int_D \Delta u + \int_0^t \int_D \left(f(u) - \frac{1}{|D|}\int_D f(u) \right) = 0. \tag{4.2.7}$$

Now, the second term of (4.2.7) vanishes by using Green's theorem and the boundary condition (4.2.6b),

$$\int_D \Delta u = \int_{\partial D} \nabla u \cdot n = 0. \tag{4.2.8}$$

The last term of (4.2.7) vanishes as well

$$\int_D \left(f(u) - \frac{1}{|D|}\int_D f(u) \right) = \int_D f(u) - \int_D \left(\frac{1}{|D|}\int_D f(u) \right) = \int_D f(u) - \int_D f(u) = 0. \tag{4.2.9}$$

Finally, the first term of (4.2.7) simplifies as

$$\int_0^t \int_D u_t = \int_D \int_0^t u_t = \int_D u(x,t) - \int_D u(x,0) = \int_D u(x,t) - \int_D u_{init}(x). \tag{4.2.10}$$

Combining eqs. (4.2.7) to (4.2.10) we have that

$$\int_D u(x,t) = \int_D u_{init}(x),\ t > 0. \tag{4.2.11}$$

Solving or approximating the system in the form (4.2.6) achieves the goal of phase separation with order parameter preserved. However, the equation is nonlocal and thus presents challenges to numerical approximation. An equivalent formulation is by introducing an additional variable, a Lagrange multiplier. This formulation is equivalent to (4.2.6).

Consider systems of equations of the following form,

$$\begin{cases} u_t - \Delta u + f(u) - \lambda(t) = 0, & x \in D,\ t > 0, \quad (4.2.12a) \\ \nabla u \cdot n = 0, & x \in \partial D, \quad (4.2.12b) \\ u(x,0) = u_{init}(x), & x \in D\ , \quad (4.2.12c) \\ \int_D u = k, & t > 0, \quad (4.2.12d) \end{cases}$$

for $k \in \mathbb{R}$. A similar calculation to the above, using (4.2.12d) we find that

$$\lambda(t) = \frac{1}{|D|} \int_D f(u).$$

Define the energy functional F as in (4.2.2). In (4.2.12) we have modified the Allen-Cahn equation by including the non-local term $\lambda(t)$ in (4.2.12a) and adding the constraint (4.2.12d). In [41] the authors establish (4.2.12) as a second order, non-local, mass conserving gradient flow for F, subject to the constraint (4.2.11).

For our purposes, this phenomenological model is an improvement over the Allen-Cahn and Cahn-Hilliard equations. The Cahn-Hilliard equation is fourth order, local and mass conservative. The Allen-Cahn equation is a second order, local, and mass non-conserving. By using (4.2.12) one has the best of both, in that it is mass conserving, but also second order and thus easier to work with.

The work in [41] focuses on the evolving interface of the binary mixture. Through asymptotic analysis the authors established that the binary mixture rapidly separates. Particularly useful to our CLPS model the authors have demonstrated that this model qualitatively captures the behavior of ripening nuclei.

5 Using phase separation models to generate obstructions

In this section we develop our phase separation model for obstruction generation in porous media, which we call the Constrained Local Phase Separation (CLPS) model. The model is an extension of the Allen-Cahn (AC) equation (4.2.1), originally proposed in [1] to describe the motion of anti-phase boundaries in crystalline solids. The functional f is a given energy potential. The AC equation models the phase separation of a binary mixture by coupling a diffusion operator with a nonlinear reaction term.

The Cahn-Hilliard (CH) equation, proposed in [9], is another equation that models phase separation of binary mixtures. The AC and CH equations are often studied together, as in [45]. Both the AC and CH equations are L^2 gradient flows for the Ginzburg-Landau free energy functional [45]. See Sections 4.2.3 and 4.2.4 for more on the development of these equations.

The AC equation is second order and phase non-conserving. The CH equation is fourth order and phase conserving. The model developed in this section is both second order and phase conserving. To achieve this we the AC equation and utilize a Lagrange multiplier to enforce the total phase constraint, as described in Sections 2.3 and 4.2.4. By adding the constraint the model becomes non-local reaction diffusion equation.

The phase separation occurs in the flow domain of porous media at the pore scale. We add spatial variability to our model so that the phase separation can react accordingly to the interface of the flow domain and the solid matrix. What this means is that we can control whether obstructions aggregate adjacent to the solid matrix, similar to biofilm, or whether the obstructions aggregate away from the solid matrix, similar to hydrates.

The long time behavior the of the AC and CH equations is to find local energy minima, suggesting that our model simulates physically realistic obstructions. We are able to quickly generate a large number of pore scale geometries with obstructions, introducing stochasticity by randomizing the initial conditions.

This section is organized as follows. We begin in Section 5.1 by explaining how

we obtain multiple realizations of obstructions by using gradient flow and non-convex energy functionals. In Section 5.2 we discuss how to add phase conservation to a linear energy minimizing equation. In Section 5.3 we exhibit how to use gradient flow to evolve a system to a local minimum. In Section 5.5 we minimize a constrained nonlinear equation. In Section 5.6 we use gradient flow to evolve a constrained nonlinear equation to a local minimum. In Section 5.7 we compare solutions calculated by Newton's method to the IMEX scheme we use. In Section 5.8 we present our model in full, exhibiting how we use phase separation to generate pore scale obstructions in porous media.

5.1 Gradient flow and multiple minima of a non-convex functional

As explained above, we are interested in finding mutliple realizations of pore scale geometries with randomly distributed obstructions. In this Section these realizations will be found as local minima of a certain functional or as stationary solutions of a gradient flow problem associated with these functionals.

Let W be the so called "double well potential,"

$$W(\psi) = \frac{1}{4}\psi^2(\psi - 1)^2. \tag{5.1.1}$$

We have

$$f := \frac{dW}{d\psi} = \psi\left(\psi - \frac{1}{2}\right)(\psi - 1). \tag{5.1.2}$$

See Figure 5.1 for illustration.

The function W is neither convex nor concave, and its gradient is only locally monotone increasing and monotone decreasing. The function W has two minima at $\psi_* = 0$ and $\psi^* = 1$, and a local maximum at $\psi^0 = \frac{1}{2}$.

Note that in Section 4.2.1 the Allen-Cahn equation is introduced with a double well potential with minima at $\psi = -1$ and $\psi = 1$. We define W as in (5.1.1) so that the total sum of phases at a point is 1. With this definition, ψ can be thought of as the percentage of phase total. We feel this definition is more easily extensible to multi-phase separation.

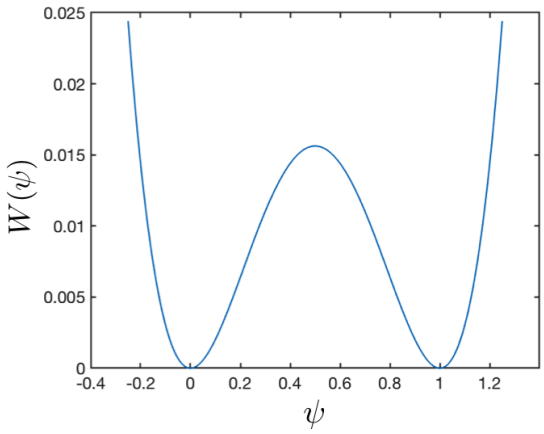

(a) $W(\psi)$, defined in (5.1.1).

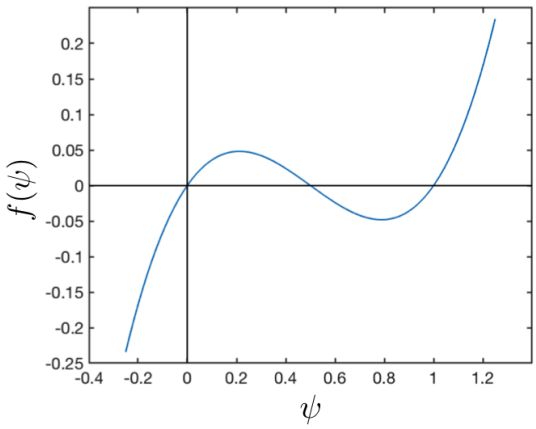

(b) $f(\psi)$, defined in (5.1.2).

FIGURE 5.1: The double well potential W and its derivative f introduced in Section 5.1.

It is clear what the critical points are for this simple problem. In general, one may employ a numerical solver, e.g., Newton's method, to solve the problem for the critical points of W by finding the root of

$$f(\psi) = 0. \tag{5.1.3}$$

iteratively. Since f is a non-monotone function with multiple zeros, depending on the initial guess $\psi^{(0)}$, the iteration will converge to either ψ_*, ψ^*, or to ψ^0.

Alternatively, a gradient flow process steers ψ towards ψ_* if the initial guess or initial condition $\psi_0 < 0.5$, or steers ψ towards ψ^* if $\psi_0 > 0.5$.. In other words, gradient flow seeks the stationary point(s) of the evolution equation

$$\frac{d\psi}{dt} + f(\psi) = 0, \quad \psi(0) = \psi_0. \tag{5.1.4}$$

The stationary solution will be one of ψ_*, ψ^*, or ψ^0 depending on ψ_0.

The existence of multiple stationary points and multiple equilibria for these simple problems is the desired feature for our phase separation method developed below.

5.2 Minimization under equality constraints

We recall the discussion in Section 2.3.1 and apply phase conservation constraints to an AC-type equation as described in Section 4.2.1. In this section we exhibit the role of the interfacial width ϵ.

Let $f \in L^2(D)$ be linear and $V \subseteq H^1(D)$. We want to find the minimizer of the functional J,

$$J(\phi) = \int_D \left(\frac{\epsilon}{2} |\nabla \phi|^2 + \frac{1}{\epsilon} W(\phi) \right),$$

over $K = \{v \in V : \int_D v = k\}$, $k \in \mathbb{R}$. Define L as in (2.3.4) with J as above.

Thus we solve the system

$$\begin{cases} -\epsilon \Delta \psi(x) - \dfrac{1}{\epsilon} f(x) - \lambda = 0, \qquad x \in D, & \text{(5.2.1a)} \\ \displaystyle\int_D \psi(x) - k = 0, & \text{(5.2.1b)} \end{cases}$$

with boundary conditions determined from V.

Example 5.2.1 (Constrained minimization with Dirichlet boundary conditions)**.** Let $V = H_0^1(D)$. We look for solutions to systems in the form of (5.2.1), with $D = (0, 1)$, $k = 1$, $\epsilon > 0$ and $f(x) = \sin(2\pi x)$,

$$\begin{cases} -\epsilon \psi_{xx}(x) - \dfrac{1}{\epsilon} \sin(2\pi x) - \lambda = 0, \qquad x \in (0, 1), & \text{(5.2.2a)} \\ \displaystyle\int_0^1 \psi = 1, & \text{(5.2.2b)} \\ \psi(0) = \psi(1) = 0. & \text{(5.2.2c)} \end{cases}$$

We present in Figure 5.2 numerical solutions to 5.2.2. We illustrate the dependence of the solutions on ϵ by solving when $\epsilon = 0.1$, $\epsilon = 0.15$ $\epsilon = 0.3$ and $\epsilon = 1$. When $\epsilon = 0.1$ the solution takes on the characteristics of the oscillatory sine function. As ϵ increases we see that λ is increasing as well, shifting the source terms from being dominated by f to being dominated by λ. We see that when $\epsilon = 1$ the solution is nearly symmetric, as one would expect if the source term was uniform.

To illustrate the impact of the constraint on the solutions, we solve the uncon-

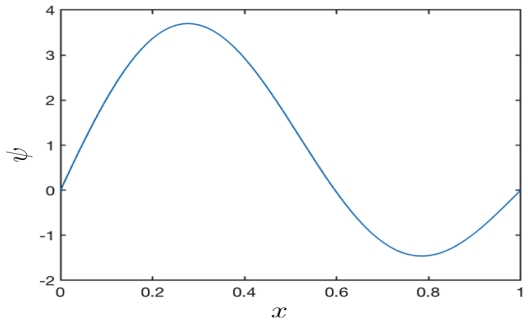

(a) $\epsilon = 0.1$, $\lambda \approx 1.2$.

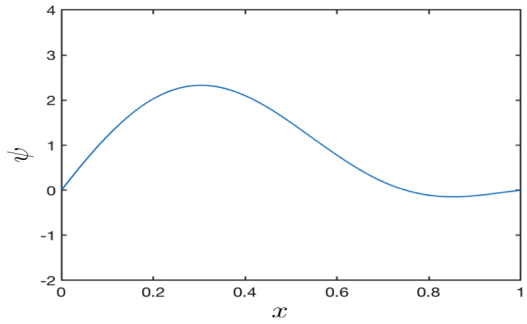

(b) $\epsilon = 0.15$, $\lambda \approx 1.8$.

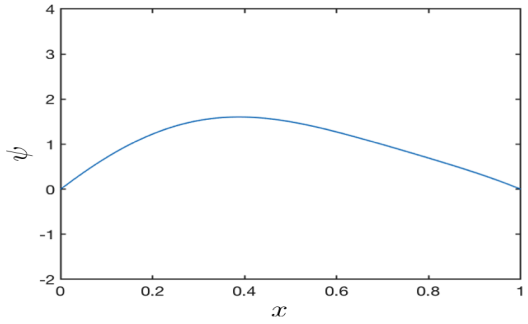

(c) $\epsilon = 0.3$, $\lambda \approx 3.6$.

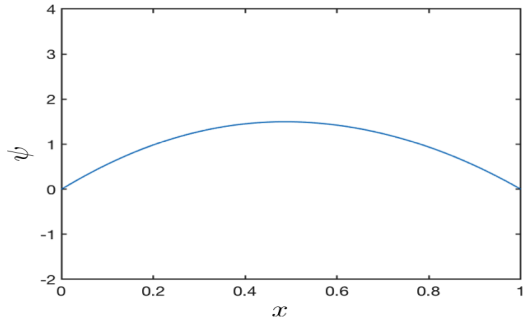

(d) $\epsilon = 1$, $\lambda \approx 12$.

FIGURE 5.2: Numerical solutions $\psi(x)$ to (5.2.2) in Example 5.2.1 with varying ϵ. In each example λ provided is found by solving the problem (5.2.2).

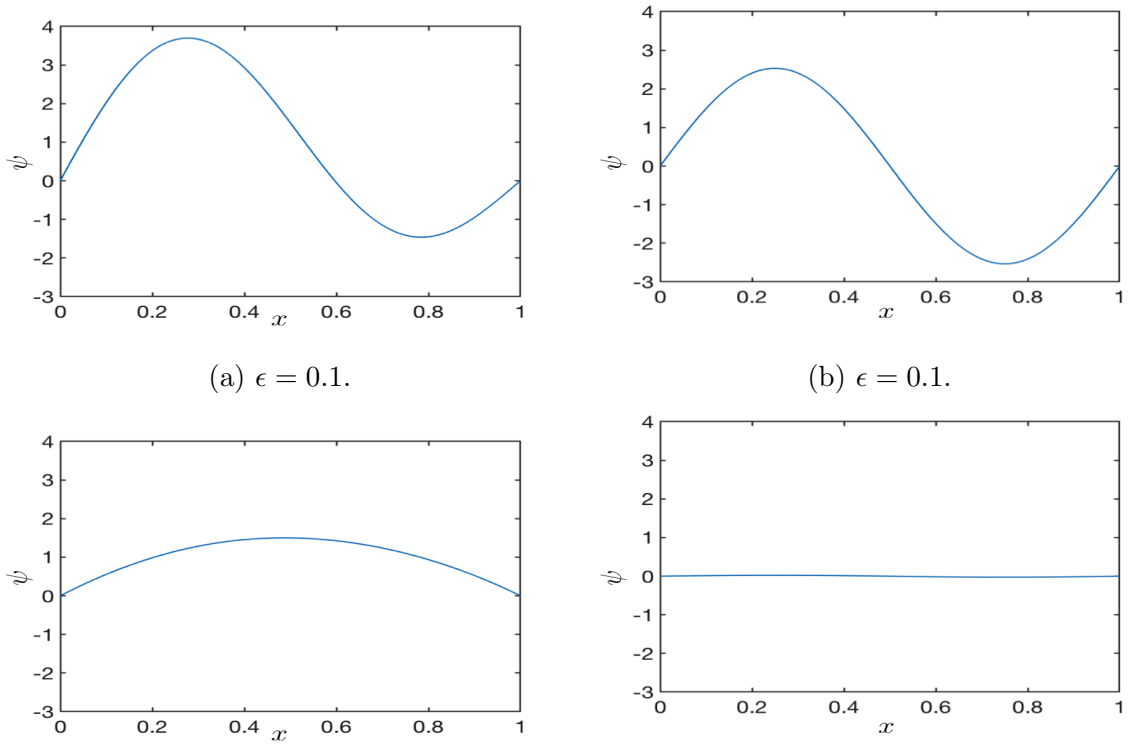

(a) $\epsilon = 0.1$.

(b) $\epsilon = 0.1$.

(c) $\epsilon = 1$.

(d) $\epsilon = 1$.

FIGURE 5.3: Numerical solutions $\psi(x)$ to (5.2.2) (left) and (5.2.3) (right) in Example 5.2.1 with $\epsilon = 0.1$ (top) and $\epsilon = 1$ (bottom). Compares solutions to the same problem, constrained by $\int_D \psi = 1$ (left) and unconstrained (right).

strained system

$$\begin{cases} -\epsilon\psi_{xx}(x) - \dfrac{1}{\epsilon}\sin(2\pi x) = 0, \qquad x \in (0,1), & \text{(5.2.3a)} \\ \psi(0) = \psi(1) = 0, & \text{(5.2.3b)} \end{cases}$$

for comparison. In Figure 5.3 we compare solutions to the unconstrained problem (5.2.3) and the constrained problem (5.2.2). The solution to the unconstrained problem is

$$\psi(x) = \frac{1}{(2\pi\epsilon)^2}\sin(2\pi x),$$

which has the property

$$\int_0^1 \psi(x) = 0.$$

Example 5.2.2 (Constrained minimization with Neumann boundary conditions)**.** Let $V = H^1(D)$ and change function $f(x)$ in (5.2.2) and look for new solutions. Let $f(x) = \cos(2\pi x)$ and impose homogeneous Neumann boundary conditions to set up the system

$$\begin{cases} -\epsilon\psi_{xx}(x) - \dfrac{1}{\epsilon}\cos(2\pi x) - \lambda = 0 \qquad x \in (0,1) & \text{(5.2.4a)} \\ \displaystyle\int_0^1 \psi = 1, & \text{(5.2.4b)} \\ \psi_x(0) = \psi_x(1) = 0. & \text{(5.2.4c)} \end{cases}$$

Here, we have made a judicious choice for f, since we want compatibility with the Neumann boundary condition.

Another point to note here, is that without the constraint this problem would not have a unique solution. The Neumann boundary conditions allow for solutions that vary by a constant, but with the constraint, there is a unique solution. For example, for arbitrary $c \in \mathbb{R}$, define $\phi(x)$ as follows

$$\phi(x) = \frac{1}{(2\pi)^2}\cos(2\pi x) + c.$$

Then $\phi(x)$ satisfies the equation $-\phi_{xx} - \cos(2\pi x) = 0$, with homogeneous Neumann boundary conditions. Compare this with the unique solution to (5.2.4),

$$\psi(x) = \frac{1}{(2\epsilon\pi)^2}\cos(2\pi x) + 1.$$

We present in Figure 5.4 the numerical solutions to (5.2.4). We illustrate dependence of the solutions on ϵ, by showing solutions when $\epsilon = 0.1$, $\epsilon = 0.15$, $\epsilon = 0.3$ and $\epsilon = 1$. For each value of ϵ, the solution takes the oscillatory shape of the cosine function but varies in amplitude. The amplitude of the solutions decreases as ϵ increases. We see that for all values of ϵ, λ remains small.

5.3 Gradient flow for convex functionals

Suppose now we are interested in the evolution towards one of the local minima of $J(\cdot)$ over V. Let $\psi : D \times [0,\infty) \to \mathbb{R}$, and $\psi(x,0) = \psi_{init}(x)$. To find the evolution

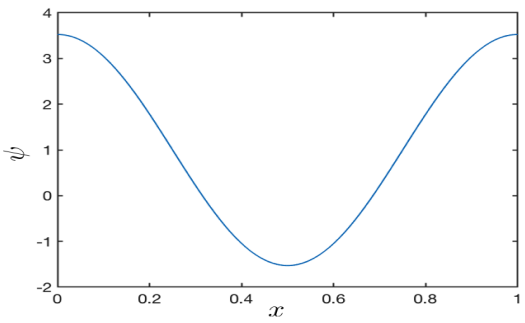

(a) $\epsilon = 0.1$, $\lambda \approx 0.01$.

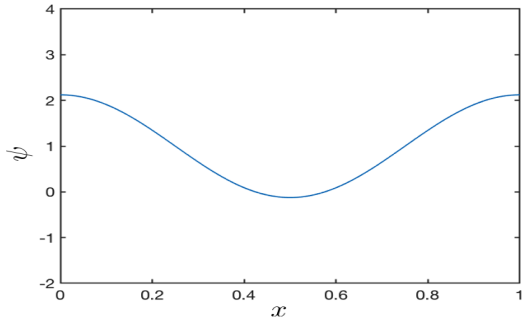

(b) $\epsilon = 0.15$, $\lambda \approx 0.0067$.

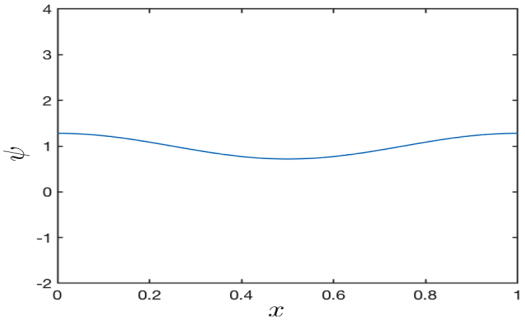

(c) $\epsilon = 0.3$, $\lambda \approx 0.0033$.

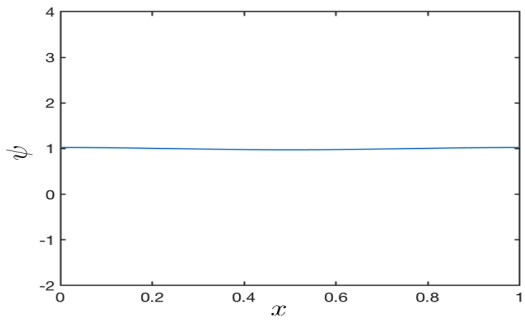

(d) $\epsilon = 1$, $\lambda \approx 0.001$.

FIGURE 5.4: Numerical solutions $\psi(x)$ to (5.2.4) in Example 5.2.2, with varying ϵ.

of $\psi(x,t)$ from its initial condition $\psi_{init}(x)$ we use gradient flow as in [18] and described in Section 4.2.2. We look for solutions to the gradient flow equation

$$\frac{\partial \psi}{\partial t} + \frac{\delta J}{\delta \psi} = 0. \tag{5.3.1}$$

Example 5.3.1 (Gradient flow with Dirichlet boundary conditions)**.** We use the problem setup described in Section 2.4.3. Let $V = H_0^1(D)$. Let $\psi \in V$, $\psi_{init}(x) = 0$, and $f(x) = \sin(2\pi x)$. We look for solutions to the follow system,

$$\begin{cases} \psi_t(x,t) - \epsilon\psi_{xx}(x,t) - \dfrac{1}{\epsilon}\sin(2\pi x) = 0, & x \in (0,1), t > 0, \quad (5.3.2a) \\ \psi(0,t) = \psi(1,t) = 0, & t > 0, \quad (5.3.2b) \\ \psi(x,0) = 0, & x \in D. \quad (5.3.2c) \end{cases}$$

In Figure 5.5 we illustrate how as $t \to \infty$, the solution to (5.3.2) approaches to the solution of the equilibrium problem (5.2.3).

5.4 Evolution to a constrained minimum

As explained earlier we are interested in finding local minima of a given functional with constraints. To do this, we combine the ideas of gradient flow and constrained minimization.

We want to find functions ψ that satisfy

$$\frac{\partial \psi}{\partial t} + \frac{\delta L}{\delta \psi} = 0, \tag{5.4.1}$$

over V.

Let $\psi : D \times [0,\infty) \to \mathbb{R}$. A solution $\psi \in K$ to (5.4.1) will satisfy

$$\begin{cases} \dfrac{\partial \psi}{\partial t}(x,t) - \epsilon\Delta\psi(x,t) - \lambda = \dfrac{1}{\epsilon}f(x), & x \in D, t > 0, \quad (5.4.2a) \\ \displaystyle\int_D \psi(x,t) = k, & t > 0. \quad (5.4.2b) \end{cases}$$

We add an initial condition and set boundary conditions based on V.

Example 5.4.1 (Gradient flow to constrained minima with Dirichlet boundary conditions)**.** Consider systems in the form of (5.4.2). Let $V = H_0^1(D)$, with $D = (0,1)$,

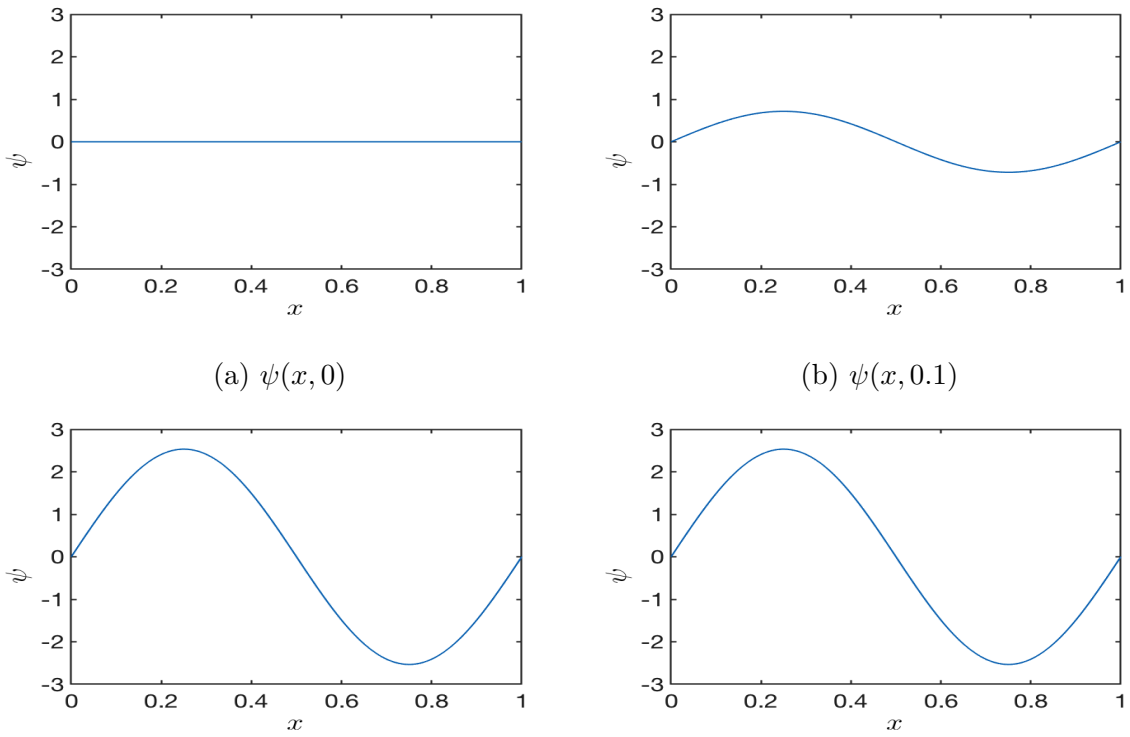

(a) $\psi(x, 0)$

(b) $\psi(x, 0.1)$

(c) $\psi(x, 10)$

(d) $\psi(x)$

FIGURE 5.5: (a-c) Solutions, $\psi(x, t)$ to (5.3.2) in 5.3.1. (d) Solution, $\psi(x)$ to (5.2.3), in 5.2.1.

$k = 1$, $\epsilon > 0$, and $f(x) = \sin(2\pi x)$. For boundary conditions, let $\psi(0,t) = \psi(1,t) = 0$. As initial conditions, we use $\psi(x) = 1$, for $x \in D$.

$$\begin{cases} \psi_t(x) - \epsilon\psi_{xx}(x) - \lambda = \dfrac{1}{\epsilon}\sin(2\pi x), & x \in (0,1),\ t > 0, \quad (5.4.3a) \\ \psi(0,t) = \psi(1,t) = 0, & t > 0, \quad (5.4.3b) \\ \psi(x,0) = 1, & x \in (0,1), \quad (5.4.3c) \\ \displaystyle\int_0^1 \psi(x,t) = 1, & t > 0. \quad (5.4.3d) \end{cases}$$

We illustrate how for two different values of ϵ, the solution, $\psi(x,t)$, to (5.4.3) converges to the equilibrium solutions of (5.2.2) in Section 5.2.1. In Figure 5.6 we show the evolution of $\psi(x,t)$ when $\epsilon = 1$ and $\tau = 0.01$. In Figure 5.7 we show the evolution of $\psi(x,t)$ when $\epsilon = 0.1$ and $\tau = 0.1$.

Example 5.4.2 (Gradient flow to the constrained minima with Neumann boundary conditions)**.** Let $V = H^1(D)$, so we have homogeneous Neumann boundary conditions and redefine $f(x) = \cos(2\pi x)$,

$$\begin{cases} \psi_t(x) - \epsilon\psi_{xx}(x) - \lambda = \dfrac{1}{\epsilon}\cos(2\pi x), & x \in (0,1),\ t > 0, \quad (5.4.4a) \\ \psi_x(0,t) = \psi_x(1,t) = 0, & t > 0, \quad (5.4.4b) \\ \psi(x,0) = 1, & x \in (0,1), \quad (5.4.4c) \\ \displaystyle\int_0^1 \psi(x,t) = 1, & t > 0. \quad (5.4.4d) \end{cases}$$

We present snapshots of solutions $\psi(x,t)$ to (5.4.4) for two different values of ϵ. The time step is varied since the solution when $\epsilon = 1$ converges much faster than the solution when $\epsilon = 0.1$.. We see in Figures 5.8 and 5.9 the solutions when $\epsilon = 1$ and $\epsilon = 0$, respectively. The solutions $\psi(x,t)$ converge to the solutions of the equilibrium problem (5.2.4).

5.5 Minimization of a constrained, nonlinear equation at pore scale

In this section we introduce nonlinearities as well as the dependence on the geometry of the pore domain to the functional J. These are designed to "promote" a

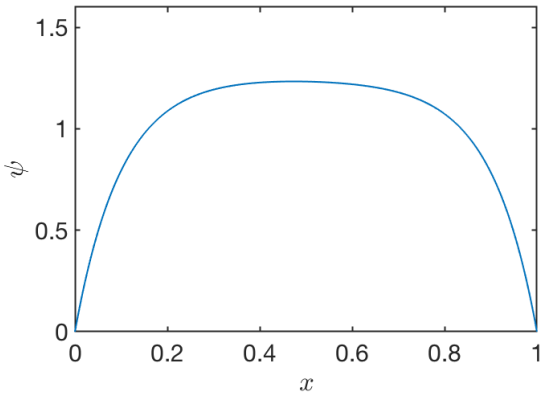

(a) $t = 0.01$.

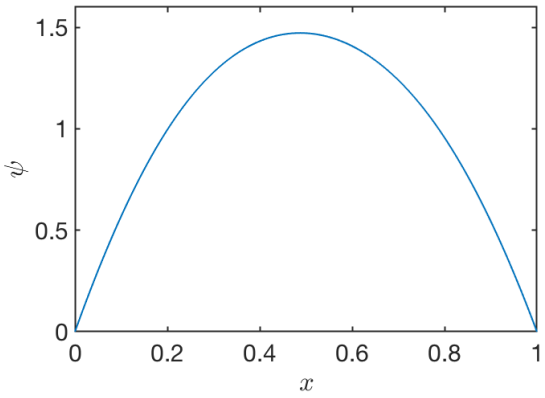

(b) $t = 0.05$.

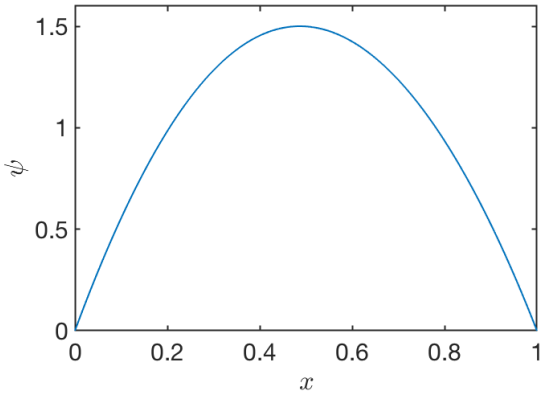

(c) $t = 0.15$.

FIGURE 5.6: Numerical solutions, $\psi(x, t)$ to (5.4.3) in Section 5.4.1 with $\epsilon = 1$. As time increases, the solution approaches the equilibrium solution shown in Figure 5.2d.

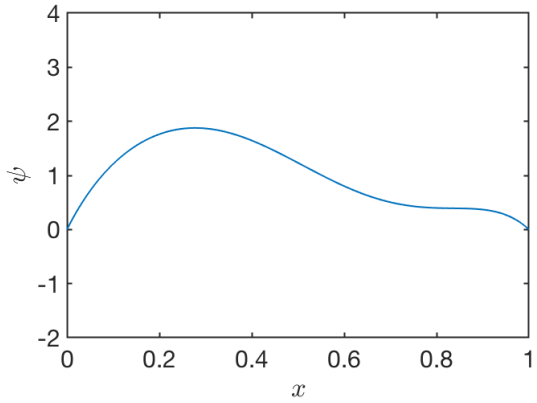

(a) $t = 0.1$.

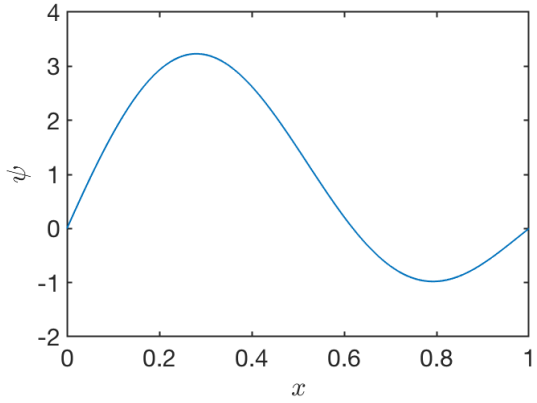

(b) $t = 0.5$.

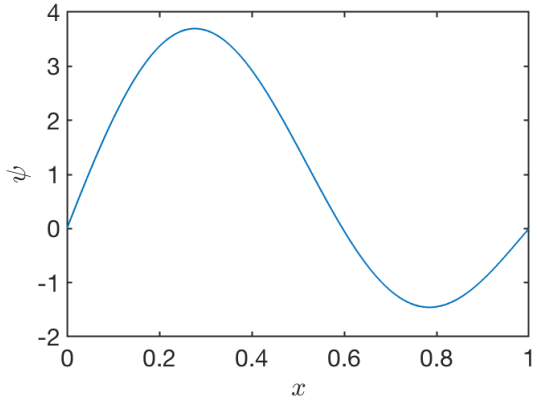

(c) $t = 2$.

FIGURE 5.7: Numerical solutions, $\psi(x, t)$, to (5.4.3) in Section 5.4.1 with $\epsilon = 0.1$. As time increases, the solution approaches the equilibrium solution shown in Figure 5.2a.

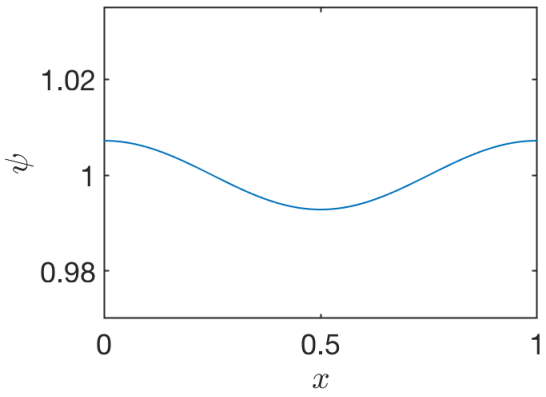

(a) $t = 0.01$.

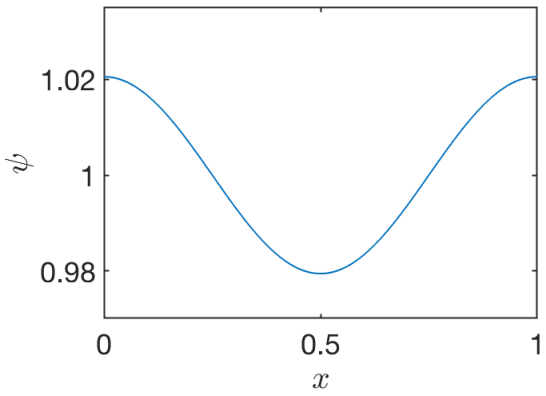

(b) $t = 0.05$.

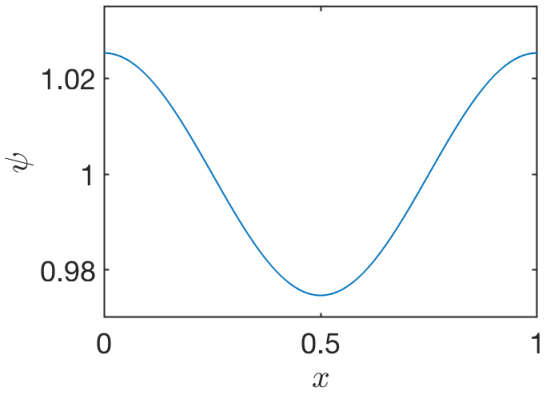

(c) $t = 0.2$.

FIGURE 5.8: Numerical solutions, $\psi(x)$, to (5.4.4) with $\epsilon = 1$. As time increases, the solution approaches the equilibrium solution shown in Figure 5.4d.

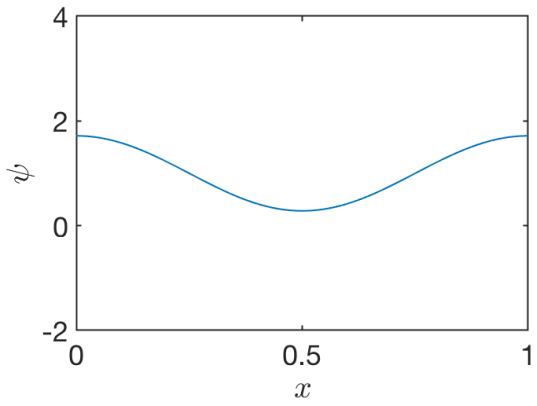

(a) $t = 0.1$.

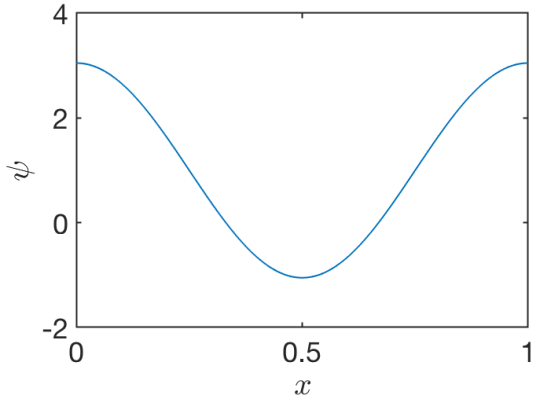

(b) $t = 0.5$.

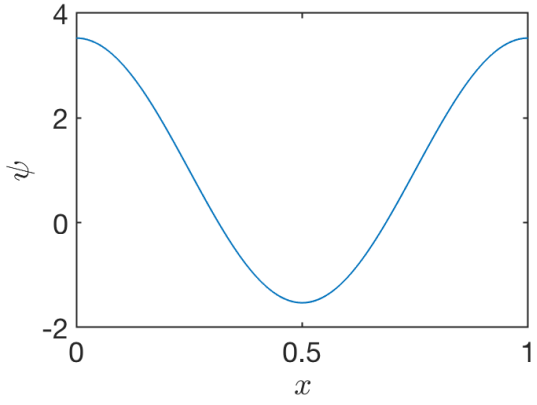

(c) $t = 4$.

FIGURE 5.9: Numerical solutions, $\psi(x)$, to (5.4.4) with $\epsilon = 0.1$. As time increases, the solution approaches the equilibrium solution shown in Figure 5.4a.

particular behavior of the solution ψ to the phase separation problem. In particular, these nonlinear functions aim to produce the stationary solutions for which the regions where $\phi(x) = 0$ or $\phi(x) = 1$ aggregate together. Furthermore, they are designed to cause these regions to be close or to be far from the wall of the porous medium, as desired for a given example.

Let $V = H^1(D)$. Now we define auxiliary functions used in the model to generate obstructions.

Definition 5.5.1 (Injection functions)**.** Let $W : \mathbb{R} \to \mathbb{R}$, with $W \in C^1(\mathbb{R})$. Let also $G : D \times \mathbb{R} \to \mathbb{R}$, with

$$G(x, \phi) = r(x)Q(\phi)\chi_{[a,b]}(\phi). \tag{5.5.1}$$

Here $\chi_{[a,b]}(\phi)$ is the characteristic function on the interval (a, b), for $a, b \in \mathbb{R}$, and $Q(\cdot) \in C^1(\mathbb{R})$ and $r(x) \in C(D)$ be given.

Define W as the double well potential given in (5.1.1). We refer to f as the coarsening function. We refer to $\partial_\phi G(x, \phi) = g(x, \phi)$ as the localization function.

Let $J : V \to \mathbb{R}$ be defined as follows

$$J(\phi) = \int_D \left(\frac{\epsilon}{2}|\nabla\phi|^2 + \frac{1}{\epsilon}W(\phi) + \theta G(x, \phi) \right),$$

with $\theta \in \mathbb{R}$. Define L as in (2.3.4), with J as above.

We want to find functions $\psi \in K$ that satisfy

$$\frac{\delta L}{\delta \psi} = 0. \tag{5.5.2}$$

A solution $\psi : D \to \mathbb{R}$ will satisfy

$$\begin{cases} -\epsilon\Delta\psi(x) + \dfrac{1}{\epsilon}f(\psi) + \theta g(x, \psi) - \lambda = 0, & x \in D, & \text{(5.5.3a)} \\ \dfrac{\partial\psi}{\partial n}(x) = 0, & x \in \partial D, & \text{(5.5.3b)} \\ \displaystyle\int_D \psi(x) = k. & & \text{(5.5.3c)} \end{cases}$$

Because this model is nonlinear, we do not make any claims on the existence and uniqueness of solutions.

In what follows we propose to use the particular functions W and G based on intuition and heuristics. While full analysis of the well-posedness of the nonlinear problem (5.5.3) with the particular functions W and G is out of our scope, we intend to consider it in the future. On the other hand we attempt to explain the reasoning behind our heuristics in the section below.

Definition 5.5.2 (Localization functions, $d = 1$)**.** Let $D = (0, 1)$. We define an auxiliary function $G_\delta(x, \psi) = r_\delta(x)Q(\psi)$, with $\delta \in \mathbb{R}$

$$r_\delta(x) = \begin{cases} 1 - \frac{x}{\delta}, & x \in [0, 2\delta], \\ -1, & x > 2\delta, \end{cases} \tag{5.5.4}$$

where

$$Q(\psi) = \begin{cases} 0, & \psi < 0, \\ \frac{1}{3}\psi^3 - \frac{1}{2}\psi^2, & 0 \le \psi \le 1, \\ -\frac{1}{6}, & \psi > 1. \end{cases} \tag{5.5.5}$$

Then we calculate

$$q(\psi) = \frac{dQ}{d\psi}(\psi) = \begin{cases} 0, & \psi < 0, \\ \psi^2 - \psi, & 0 \le \psi \le 1, \\ 0, & \psi > 1. \end{cases}$$

We note that

$$q(\psi) \le 0, \tag{5.5.6}$$

and that g_δ is

$$g_\delta = r_\delta(x)q(\psi) = r_\delta(x)\psi(\psi - 1)\chi_{[0,1]}(\psi). \tag{5.5.7}$$

The one dimensional localization function is defined for optimal use in examples illustrating the impact of g_δ and θ. That is, $r_\delta(0) = 1$ and $r_\delta(1) = -1$. We see in the following definition for localization functions in higher dimensions that $r_\delta|_\Gamma = 1$.

Definition 5.5.3 (Localization functions, $d > 1$)**.** Let $D \in \mathbb{R}^2$ and $\Gamma \subset D$. Define r_δ

as follows,

$$r_\delta(x) = \begin{cases} 1 - \frac{1}{\delta} \min_{x_0 \in \Gamma} ||x - x_0||_{l^2}, & ||x - x_0||_{l^2} < 2\delta \\ -1, & ||x - x_0||_{l^2} \geq 2\delta. \end{cases} \tag{5.5.8}$$

Define localization function $G_\delta(x, \psi) = r_\delta(x)Q(\psi)$, with Q as above.

5.5.1 Equilibrium model with localization functions

We consider now an equation in the form of (5.5.3) in which we introduce additional parameters $\epsilon > 0$ and $\theta \in \mathbb{R}$. We consider the stationary problem

$$-\epsilon\psi_{xx} + \frac{1}{\epsilon}f + \theta g_\delta - \lambda = 0. \tag{5.5.9}$$

and the associated evolution problem

$$\psi_t - \epsilon\psi_{xx} + \frac{1}{\epsilon}f + \theta g_\delta - \lambda = 0. \tag{5.5.10}$$

Our goal now is to explain the impact of f and g and of the parameters ϵ and θ. We ignore the role λ for now: as we have seen, λ and the additional equation (5.5.3c) together maintain the total amount of ψ.

First we consider the impact of f alone, i.e., if $\theta = 0$. By including ϵ in (5.5.9) we can control the magnitude of the diffusion relative to the sharpening due to f. In other words, the diffusion operator smears the solution ψ while f sharpens the solution ψ towards either 0 and 1; the parameter ϵ provides relative control on those effects.

Next we explain the role of θg_δ. For illustration, we show the components of

$$g(x, \psi) = r_\delta(x)q(\psi)$$

in Figure 5.10, with $\delta = 0.25$.

We first discuss the role of $q(\psi) = -\psi(1 - \psi)\chi_{[0,1]}(\psi)$. This nonpositive function when present in, e.g., $-\epsilon\psi_{xx} + \frac{1}{\epsilon}f + \theta q = 0$, acts as a penalty term or nonlinear source term whose effect is confined to $\psi \in [0, 1]$. The impact is the strongest when $\psi \approx \frac{1}{2}$. It is hard however to discuss fully this equilibrium problem due to the nonlinearities involved for the whole range of possible boundary conditions. In particular, we see that

the problem $-\epsilon\psi_{xx} + q = 0$ alone, with homogeneous Neumann conditions has exactly two solutions $\psi(x) = 1$, and $\psi(x) = 0$.

On the other hand, we can get insight to the evolution problem (5.5.10) by studying, e.g., the ODE $\psi_t + f + \theta q = 0$ first. With $\theta > 0$ we see that $\psi_t = -\theta q$ has a stable equilibrium at 1, and an unstable one at 0. Adding $-f$ to the right hand side does not change the qualitative nature of this evolution towards the stable equilibrium $\psi^* = 1$. In contrast, if $\theta < 0$ then it is the $\psi_* = 0$ which is "promoted".

Next we discuss the product in θg_δ of $\theta q(\psi)$ with $r_\delta(x)$. By design, the factor r_δ controls the impact of q which depends the location x and its distance relative to the left boundary of D.

Let $\theta > 0$, (respectively $\theta < 0$). Then close to the left boundary $x = 0$ we have $r_\delta \approx 1$, thus the effect for $x < \delta$ is to "encourage" ψ towards $\psi^* = 1$. Away from the boundary $r_\delta \approx -1$, and the effect is to promote $\psi_* = 0$.

Finally, we use the magnitude of $\theta \in \mathbb{R}$ to control the amplitude of this feature.

5.6 Using gradient flow to find local minima of constrained nonlinear equations

We now use the gradient flow method to find stationary solutions to nonlinear equations. Since the functionals involved may not be necessarily convex, we expect to get stationary solutions which correspond to local minima, and which are dependent on the initial condition used. In other words, we expect that there are multiple equilibria. This is the desired effect.

We explain gradient flow in Section 5.1. We refer to background information in Section 4.2.2.

Define L as in the previous section. We wish to find solutions to (5.4.1) in K. By using a family of initial conditions we will find a family of solutions ψ.

Example 5.6.1 (Gradient flow to local minima)**.** Let $D = (0, 1)$ and $V = H_0^1(D)$. We

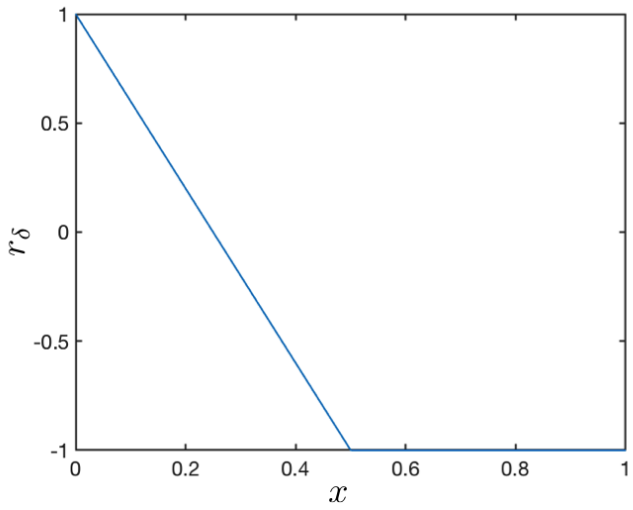

(a) $r_\delta(x)$, $\delta = 0.25$, (5.5.4).

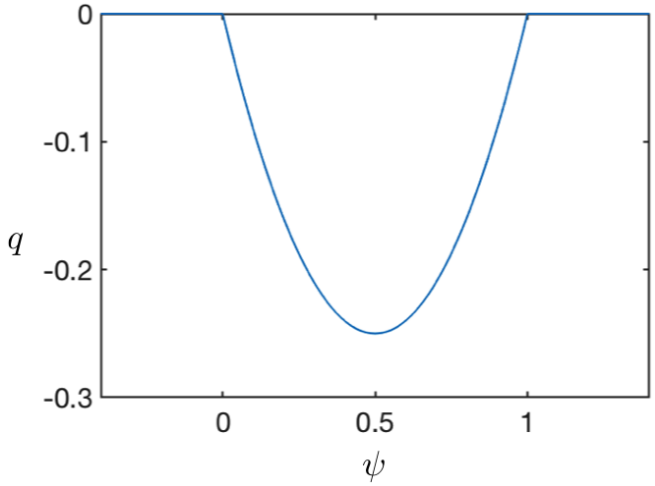

(b) $q(\psi)$, defined in (5.5.7).

FIGURE 5.10: The components of $g_\delta(x, \psi) = r_\delta(x)q(\psi)$ introduced in Section 5.5.2

look for solutions $\psi(x,t)$ to

$$\begin{cases} \psi_t - \epsilon\psi_{xx} - \lambda = -\dfrac{1}{\epsilon}f - \theta g_\delta, & x \in (0,1),\ t > 0, \quad (5.6.1a) \\ \psi_x(0,t) = \psi_x(1,t) = 0, & t > 0, \quad (5.6.1b) \\ \psi(x,0) = \psi_{init}(x), & x \in (0,1), \quad (5.6.1c) \\ \displaystyle\int_D \psi(x,t) = 0.5, & t > 0. \quad (5.6.1d) \end{cases}$$

This example will include many variations on ϵ, θ and δ, as we explore how these variables impact solutions. As before, we use the numerical methods described in 2.4.3.

For illustration we use two different initial conditions, $\psi^{(i)}_{init}(x)$, $i \in \{1,2\}$. In numerical experiments we set $\psi^{(1)}_{init}(x_j)$ to 0 or 1 such that $\psi_{init}(x_j) \sim U\{0,1\}$, $1 \le j \le M-1$. The second $\psi^{(2)}_{init}(x_j)$ is drawn from the same distribution.

Example 5.6.2. Our first experiment will show how different initial conditions allow the method to find different local minima. Let $\epsilon = 0.005$, $\theta = 10$, and $\delta = 0.1$.

In Figures 5.11 and 5.12 we show the two stationary states corresponding to the different initial conditions.

When the initial condition is set at $\psi^{(1)}_{init}(x)$, a single valley in the phase parameter forms in $\psi(x, 0.1)$. For this single large valley, the balance between the diffusion operator and the double well potential is such that the peaks remain separate, i.e., the sharpening due to the double well potential holds.

When the initial condition is set to $\psi^{(2)}_{init}(x)$, two smaller valleys can be observed in $\psi(x, 0.5)$. In this case, the diffusion operator and the double well potential cause the formation of a single block of phase parameter.

Example 5.6.3. In this experiment we check for dependence of solutions on the grid. We repeat the previous experiment with $\psi_{init}(x) = \psi^{(1)}_{init}(x)$, but halve the step size. Compare the result in Figure 5.13 with Figure 5.11. Let $\hat{\psi}$ be the solution on the refined grid and ψ the solution on the original grid. In Figure 5.14 we show $|\hat{\psi} - \psi|$ and

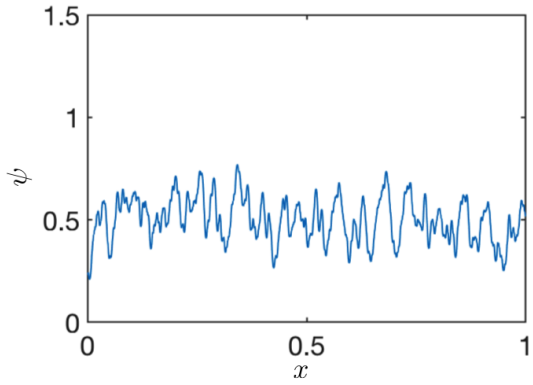

(a) $\psi(x, 0.005)$.

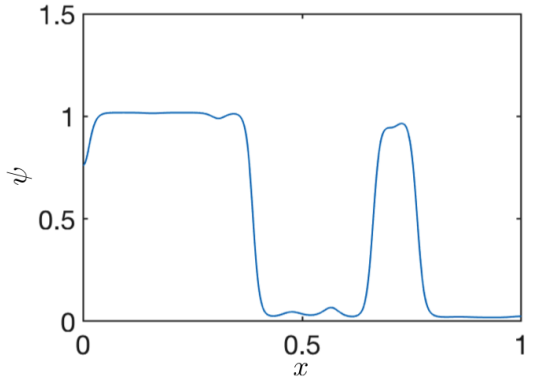

(b) $\psi(x, 0.1)$.

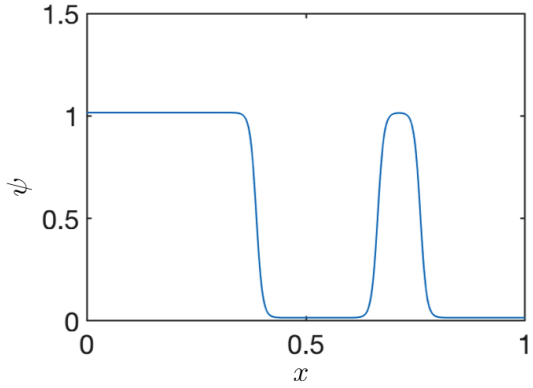

(c) $\psi(x, 0.4)$.

FIGURE 5.11: Solutions $\psi(x, t)$ to (5.6.1), with initial conditions $\psi_{init}^{(1)}(x)$ (top).

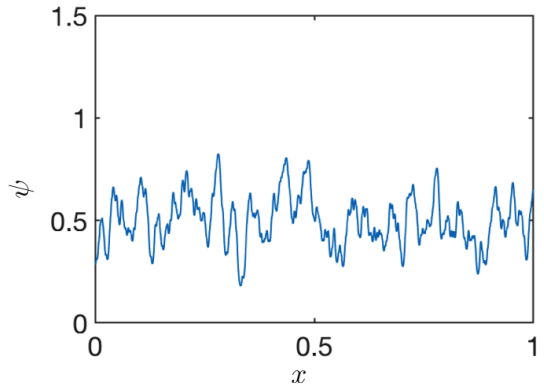

(a) $\psi(x, 0.005)$.

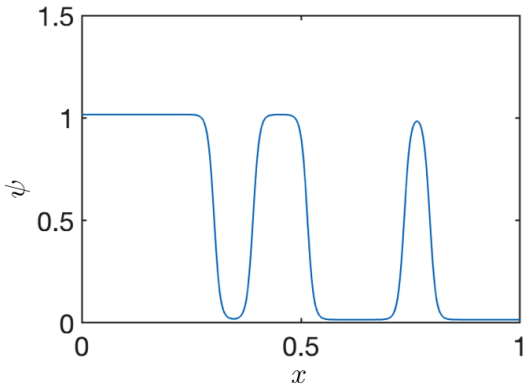

(b) $\psi(x, 0.5)$.

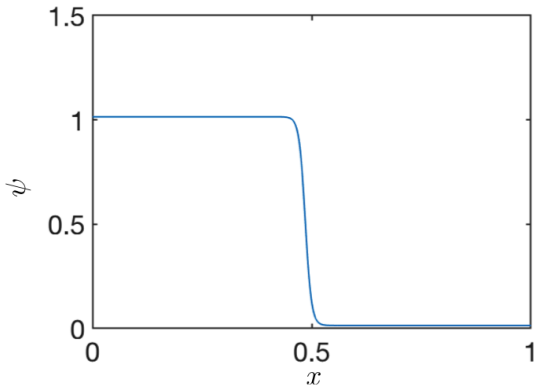

(c) $\psi(x, 5.5)$.

FIGURE 5.12: Solutions $\psi(x, t)$ to (5.6.1), with initial conditions $\psi^{(2)}_{init}(x)$.

observe that the greatest difference in solutions is at the phase interface. The relative difference in λ is

$$\frac{|\hat{\lambda} - \lambda|}{\hat{\lambda}} = 7.8 \times 10^{-4}.$$

For the rest of the experiments, let $\psi_{init}(x) = \psi^{(2)}_{init}(x)$.

Example 5.6.4. In this example we study the impact of θ. In Figure 5.15 we compare results for when $\theta = 1$ and $\theta = 10$. In both cases we use $\epsilon = 0.005$ and $\delta = 0.1$. For this problem, higher positive values for θ encourage the phase parameter to be closer to 1 on the left boundary and closer to 0 on the right boundary. So we see that when $\theta = 1$ we are only weakly encouraging this behavior and on the right boundary we have that the phase parameter is near 1. Then, when $\theta = 10$ we are strongly encouraging the behavior, so at the right boundary the phase parameter is suppressed to near 0.

Example 5.6.5. We look next at the impact of ϵ, shown in Figure 5.16. Let $\theta = 1$ and $\delta = 0.1$. We see from Figure 5.16a that smaller values of ϵ enforce separation of the phase parameter towards 0 and 1, allowing multiple smaller blocks of phase parameter. As ϵ increases, Figure 5.16b, the smaller peaks of phase parameter are absorbed into the larger block when they are not separated by too much distance. At large values of ϵ, as shown in Figure 5.16c, the solution smears and loses the sharp distinction in phase parameter values.

5.7 Newton's Method

We examine the use of Newton's method to solve the equilibrium problem (5.5.2) and the time dependent gradient flow problem (5.4.1) with L defined as in the previous section. That is, we use Newton's method to directly find the solution of an equilibrium problem and also to solve for each time step in an evolutionary equation. The main point is that the Newton iteration may converge to different solutions depending on the

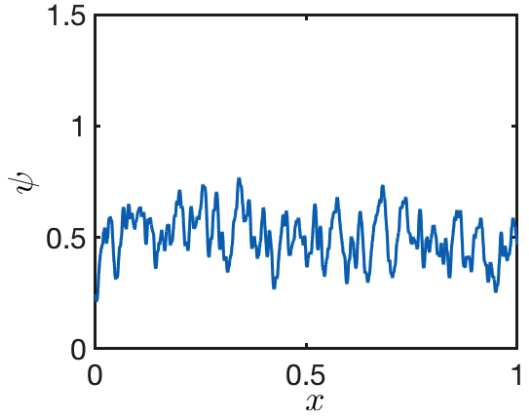

(a) $\psi(x, 0.005)$.

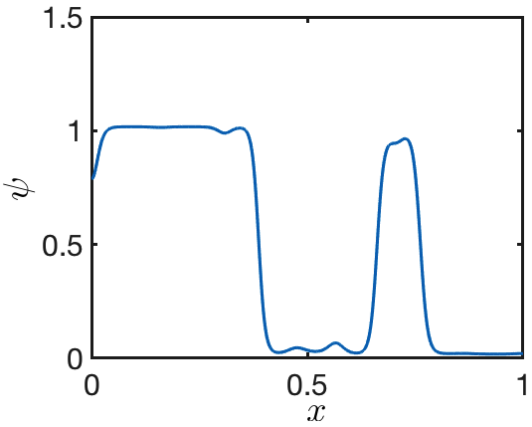

(b) $\psi(x, 0.1)$.

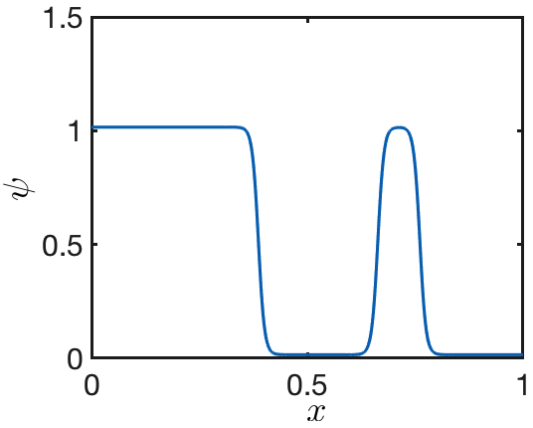

(c) $\psi(x, 0.4)$.

FIGURE 5.13: Solutions $\psi(x, t)$ to (5.6.1) with initial conditions $\psi_{init}^{(1)}(x)$ on a refined grid.

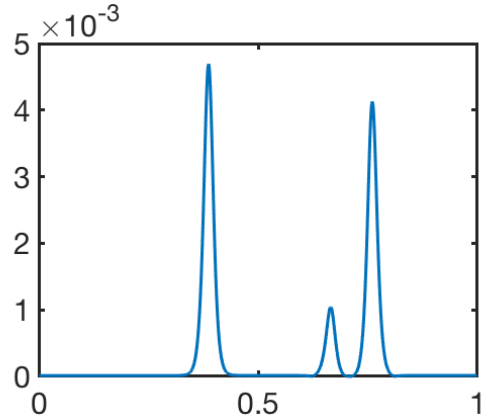

FIGURE 5.14: Difference in solutions on original grid and the refined grid, $|\hat{\psi} - \psi|$.

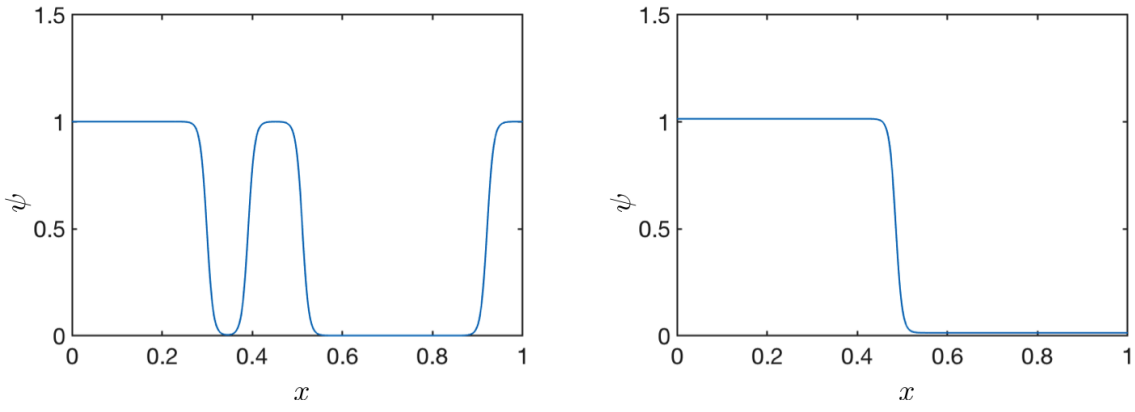

(a) $\psi(x, 4.5)$ with $\theta = 1$.

(b) $\psi(x, 5.5)$ with $\theta = 10$.

FIGURE 5.15: Solutions, $\psi(x, t)$, to (5.6.1) showing the impact of the coefficient θ.

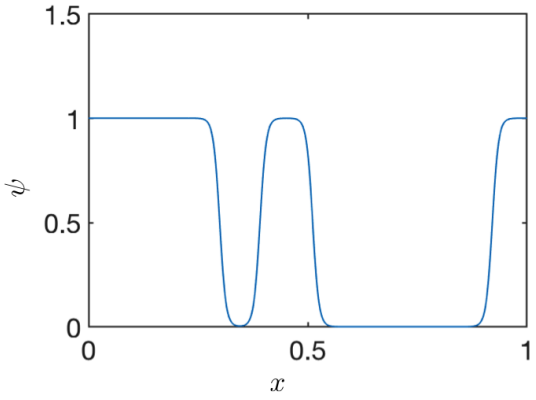

(a) $\psi(x, 4.5)$, $\epsilon = 0.005$.

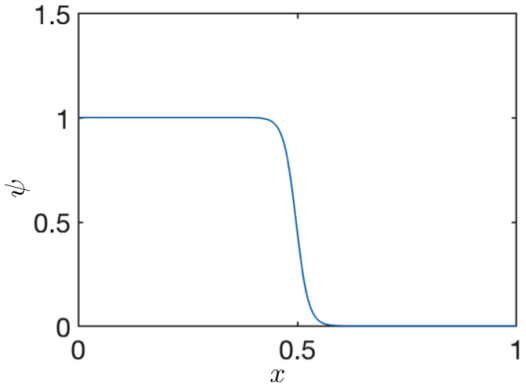

(b) $\psi(x, 1.5)$, $\epsilon = 0.01$.

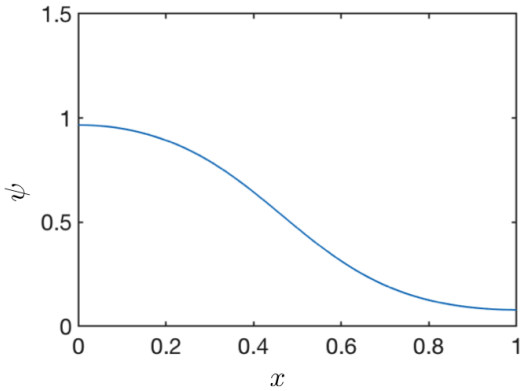

(c) $\psi(x, 3.0)$, $\epsilon = 0.1$.

FIGURE 5.16: Solutions $\psi(x, t)$, to (5.6.1) showing the impact of the coefficient ϵ.

initial guess. Similarly, the gradient flow may converge to different stationary solutions depending on the initial conditions chosen.

However, we show that the solution we calculate via gradient flow is qualitatively similar to solutions found via Newton's method.

Example 5.7.1 (Using Newton's method to solve equilibrium problem (5.5.3))**.** Define $\mathcal{F}$ as follows.

$$\mathcal{F}(\psi,\lambda) = \begin{bmatrix} \mathcal{F}_1 \\ \mathcal{F}_2 \end{bmatrix} := \begin{bmatrix} -\epsilon\Delta\psi + \frac{1}{\epsilon}f + \theta g - \lambda \\ \int_D \psi(x) - k_0 \end{bmatrix}. \tag{5.7.1}$$

We apply the Finite Difference discretization described in Section 2.4.3 to (5.7.1), and use Newton iteration (2.5.2).

Define the following diagonal square matrices with diagonals as follows,

$$\begin{aligned} \text{diag}(\mathbb{F}^{(k)}) &= \left[f_1^{(k)} \cdots f_{M-1}^{(k)}\right]^T, \\ \text{diag}(\mathbb{F}_\psi^{(k)}) &= \left[{f_1'}^{(k)} \cdots {f'}_{M-1}^{(k)}\right]^T, \\ \text{diag}(\mathbb{G}^{(k)}) &= \left[g_1^{(k)} \cdots g_{M-1}^{(k)}\right]^T, \\ \text{diag}(\mathbb{G}_\psi^{(k)}) &= \left[\partial_\psi g_1^{(k)} \cdots \partial_\psi g_{M-1}^{(k)}\right]^T. \end{aligned}$$

This results in the following system,

$$\begin{bmatrix} \epsilon A + \frac{1}{\epsilon}\mathbb{F}_\psi^{(k)} + \theta\mathbb{G}_\psi^{(k)} & -B \\ B^T & 0 \end{bmatrix} \begin{bmatrix} \psi^{(k+1)} \\ \lambda^{(k+1)} \end{bmatrix} = \begin{bmatrix} \left(\frac{1}{\epsilon}\mathbb{F}_\psi^{(k)} + \theta\mathbb{G}_\psi^{(k)}\right)\psi^{(k)} - \left(\frac{1}{\epsilon}\mathbb{F}^{(k)} - \theta\mathbb{G}^{(k)}\right)\mathbb{1} \\ k_0/h \end{bmatrix}. \tag{5.7.2}$$

Let $\epsilon = 0.005$ and $\delta = 0.1$. We present in Figure 5.17 solutions $\psi^{(k)}$ when $\theta = 1$ and $\theta = 10$. This set of coefficients and parameter is identical to the solutions presented in Figure 5.15. We observe that the two methods find different local minima, i.e. the distribution of the phase parameter ψ is significantly different. However, the same qualitative behavior exists, in that as θ increases, we see the suppression of ψ on the right boundary, as we'd expect.

Example 5.7.2. [Using Newton's method to solve the evolutionary problem (5.4.1)] In this case, we are using gradient flow to find the equilibrium solution and utilizing Newton's method to do a fully implicit solve for each time step.

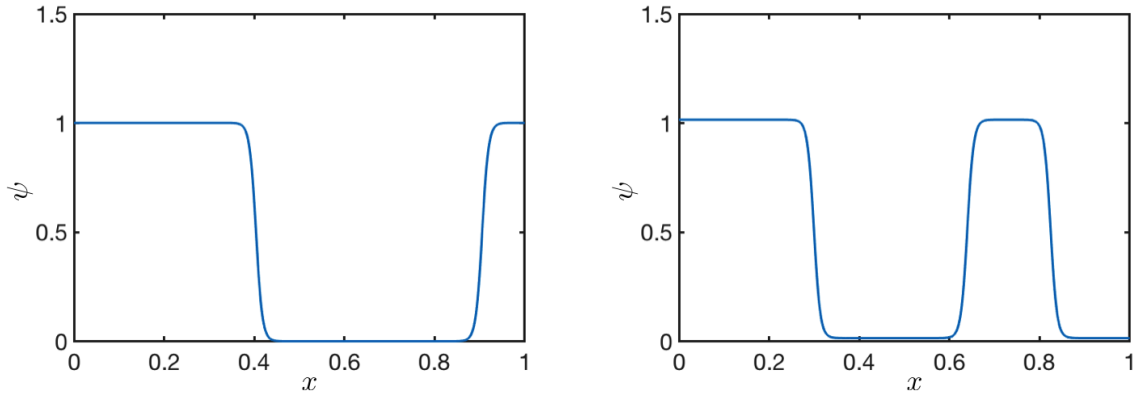

(a) $\psi^{(1127)}$ with $\theta = 1$.

(b) $\psi^{(46)}$ with $\theta = 10$.

FIGURE 5.17: Solutions, $\psi^{(k)}$, to (5.7.2)

We first discretize (5.4.1) in time with backward Euler,

$$\frac{\psi^{(n+1)} - \psi^{(n)}}{\tau} - \epsilon\Delta\psi^{(n+1)} + \frac{1}{\epsilon}f(\psi^{(n+1)}) + \theta g(\psi^{(n+1)}) = 0.$$

Define $\mathcal{F}$, as

$$\mathcal{F}(\hat{\psi}, \lambda) = \begin{bmatrix} \mathcal{F}_1 \\ \mathcal{F}_2 \end{bmatrix} := \begin{bmatrix} \frac{\hat{\psi}-\psi^{(n)}}{\tau} - \epsilon\Delta\hat{\psi} + \frac{1}{\epsilon}f(\hat{\psi}) + \theta g(\hat{\psi}) - \hat{\lambda} \\ \int_D \hat{\psi}(x) - k_0 \end{bmatrix}. \tag{5.7.3}$$

We apply the iteration (2.5.2) and the Finite Difference discretization described in Section 2.4.3 to (5.7.3). This results in the following system,

$$\begin{bmatrix} I + \tau\epsilon A + \frac{\tau}{\epsilon}\hat{\mathbb{F}}_{\psi}^{(k)} + \tau\theta\hat{\mathbb{G}}_{\psi}^{(k)} & -\tau B \\ B^T & 0 \end{bmatrix} \begin{bmatrix} \hat{\psi}^{(k+1)} \\ \hat{\lambda}^{(k+1)} \end{bmatrix} = \begin{bmatrix} \psi^n + \tau\left(\frac{1}{\epsilon}\hat{\mathbb{F}}_{\psi}^{(k)} + \theta\hat{\mathbb{G}}_{\psi}^{(k)}\right)\hat{\psi}^{(k)} - \left(\frac{1}{\epsilon}\hat{\mathbb{F}}^{(k)} - \theta\hat{\mathbb{G}}^{(k)}\right)\mathbb{1} \\ k_0/h \end{bmatrix}.$$

After the Newton iteration has converged, we set $\psi^{(n+1)} = \hat{\psi}^{(k)}$ and $\lambda^{n+1} = \hat{\lambda}^{(k)}$.

5.8 Generation of obstructions by phase separation in $d = 2$

We now use the tools described in this chapter to generate obstructions in pores. We are interested in recreating obstructions that are either biofilm-like or hydrate-like. As explained in Chapter 4 biofilm is a pore coating obstruction while hydrate is a pore

filling obstruction. By judiciously choosing coefficients and injection functions we will be able to capture the main characteristics of these obstructions. The choice of these coefficients is guided by heuristics and intuition rather than any quantitative model. In the future we hope to guide the choice of parameters by some data science approach.

Consider a pore domain $D_{f,r}$, partitioned into the rock matrix and the fluid space, D_r and D_f respectively. Let $\Gamma = D_f \cap D_r$ be the interface between the two domains. Let $r_\delta(x)$ be defined as in (5.5.8).

We use the double well potential defined in (5.1.1) and the localization function $\frac{\partial g_\delta}{\partial \psi}$ defined in (5.5.7). With the definition of r_δ given in (5.5.8) the behavior of g will be to either "encourage" or "discourage" the formation of obstruction close to the interface Γ. We say, colloquially, that we "promnote" certain desired behavior.

When $\theta > 0$, we promote $\psi = 1$ on Γ, and when $\theta < 0$ we promote $\psi = 0$ on Γ.

Next we present the algorithm of generation of independent realizations of pore geometries with obstructions. In other words, we assign some cells originally in D_f to D_o. Our algorithm has two main steps. STEP 1 uses a numerical simulations of the model for generation of domains with obstructions, with some random initial condition $\psi_{init}(x)$, and lets it run until a stationary state $\phi(x, t_N)$ is achieved. STEP 2 post-processes the numerical solution $\psi(x, t_N)$, and assigns D_o.

5.8.1 STEP 1

We recap the model here. The system we solve is

$$\begin{cases} \psi_t - \epsilon\Delta\psi - \lambda = -\dfrac{1}{\epsilon}f - \theta g_\delta, & x \in D_f,\ t > 0, & \text{(5.8.1a)} \\ \dfrac{\partial \psi}{\partial n} = 0, & x \in \partial D_f\ t > 0, & \text{(5.8.1b)} \\ \psi(x, 0) = \psi_{init}(x), & x \in D_f, & \text{(5.8.1c)} \\ \displaystyle\int_{D_f} \psi(x, t) = k, & t > 0. & \text{(5.8.1d)} \end{cases}$$

We refer to Section 2.4.4 for details on the numerical method for solving the following examples, as well as details on the domain D.

We run the simulations in time until the system seems to have reached a stationary solution, say until $t = t_N$.

5.8.2 STEP 2

Now we must "translate" the information provided by the order parameter $\psi(x,t)$ to indicate where the obstructions have formed. Naturally, we want to use ψ as an indicator of whether or not a particular cell is obstructed.

Now consider some value $\psi_j^N = \psi(x_j, t_N)$ found by the numerical model at time t_N and cell j. Since ψ_j^N can take any value between 0 and 1, we must decide how to decide whether x_j is in D_o or D_f. In other words, we want to assign an indicator i_j to a cell based on ψ_j^N. The indicator $i_j = 0$ if the cell j is in D_f and $i_j = 1$ otherwise. We discuss two ways to do that named ALGORITHM (A) and ALGORITHM (B).

ALGORITHM (A). One can establish a threshold value ψ_* and use it in many ways. For example, we could set a minimum value ψ_* and assign the cell associated with x_j to D_o if $\psi_j^N \geq \psi_*$, and to D_f otherwise. This first way satisfies the idea that the phase parameter ψ_j^N represents the amount of obstruction material contained in cell j. In fact, in the case of biofilm or hydrate growth we have a natural interpretation of the threshold value. In particular, the biofilm detected in imaging experiments reported in [35] was found due to the use of a contrast agent (barium) which is excluded from the biofilm phase due to the molecule size. To paraphrase, this threshold idea says that "there is enough material here to stop the flow in this cell."

ALGORITHM (B). Another way to use a threshold is by choosing a certain number M of the cells $j_1, j_2, \ldots j_M$ with the highest ψ_j^N values. This second way has the benefit of allowing a fixed number of obstructed cells. A fixed number of obstructed cells may be desirable in that it produces D_o with a predetermined desired value of porosity. In fact, recall that the initial condition $\psi_{init}(x)$ is piecewise constant and has M cells with $i_j = 1$ or $\psi_j^0 = 1$, and since our evolution model conserves the phase parameter so that $\int_D \psi(x,t)dx = const$, after applying the evolution and applying the thresholding, there should be M obstructed cells at t_N.

To find the M cells with the highest values of phase parameter we use the Matlab function `maxk`. Consider a set $(\psi_i^N)_1^{M+1}$ such that $\psi_1^N > \psi_2^N > \cdots > \psi_M^N = \psi_{M+1}^N$. Then, using the function `maxk` to return the M highest values of $(\psi_i^N)_1^{M+1}$ will return $(\psi_i^N)_1^M$. In this case, `maxk` returns ψ_M^N instead of ψ_{M+1}^N because of the lower index.

5.8.3 Examples of pore scale geometries with obstructions

Now we present examples. Since the focus of this section is on modeling with the phase parameter, we show the contours of $\psi(x, t_N)$ but we do not map from ψ_j^N to the indicator i_j of obstructed cells.

In turn, when we generate multiple realizations of the geometries D_0 and use them for the results shown later in Chapter 7 we use ALGORITHM (B), i.e., the process of choosing the M cells with the highest ψ_j^N value.

Within each example the parameters are constant, but the initial condition ψ_{init} varies so that we generate multiple realizations.

Example 5.8.1 (Pore filling obstruction generation)**.** In this case, we are generating obstructions that aggregate together and avoid the fluid-rock interface.

We choose $k = 0.05$, $\epsilon = 0.2$, $\delta = 0.1$, and $\theta = -0.5$. Note that we are also using step size $h = 0.05$, so $\delta = 3h$. In Figure 5.18 we present the simulated stationary solution corresponding to some random initial condition.

We see that as desired the pore filling obstructions form away from the fluid-rock interface.

Example 5.8.2 (Pore coating obstruction generation)**.** In this case, we are generating obstructions that aggregate together and whose growth is encouraged at the fluid-rock interface.

This time we choose $k = 0.05$, $\epsilon = 0.3$, $\delta = 0.15$, and $\theta = 0.5$. Note that we are also using step size $h = 0.05$, so $\delta = 3h$.

In Figure 5.19 we present the profile of the simulated stationary solution corresponding to some random initial condition.

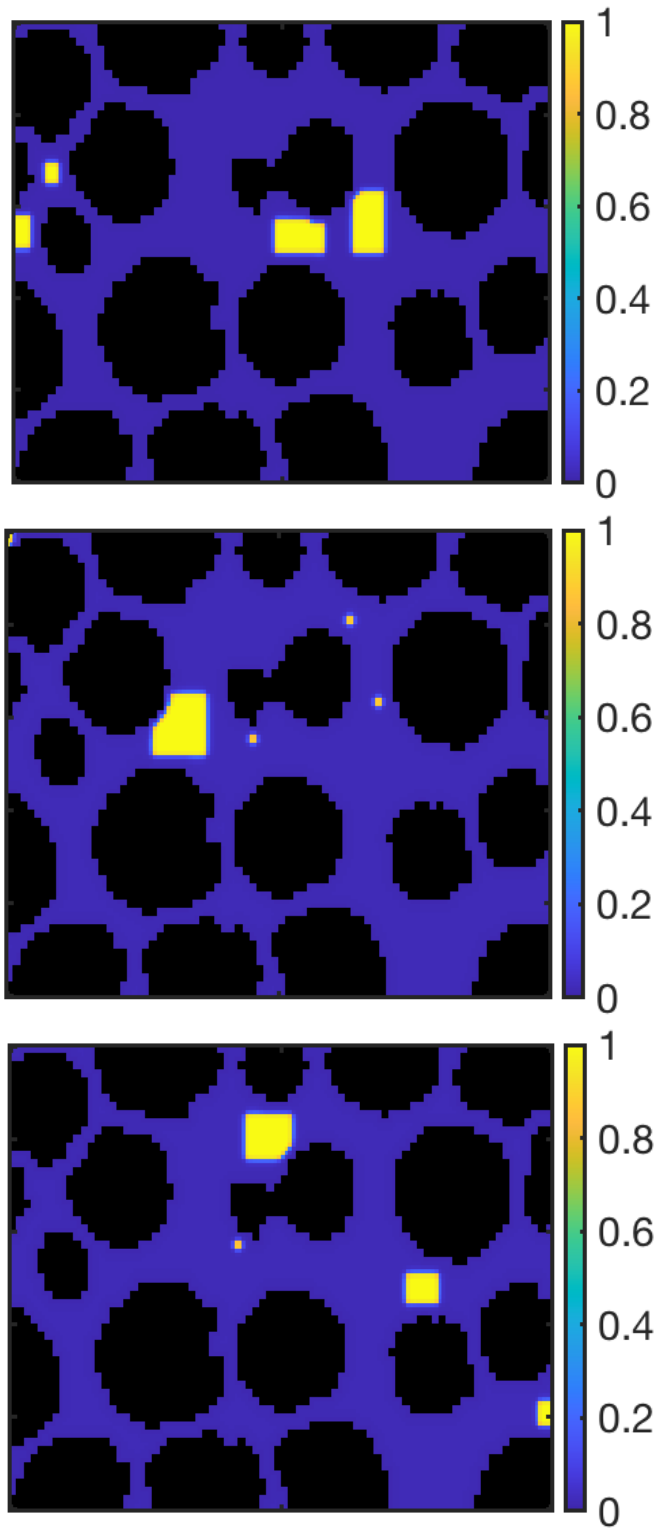

FIGURE 5.18: Pore filling obstructions generated by a method of constrained optimization. See 5.8.1. Black is the rock matrix, the color is $\psi(x)$, $x \in D_f$.

As expected, the pore coating obstructions are all adjacent to rock, with throat clogging present.

Example 5.8.3 (Pore filling obstruction on refined grid)**.** With this next example we explore the scaling effects as we refine the step size h. Denote quantities on the refined grid with a superscript *. We recreate the first experiment in Example 5.8.1 on a refined grid with step size $h^* = h/2$.

The initial conditions across experiments are retained, so $\psi^*_{init}(x) = \psi_{init}(x)$. Similarly, the total phase parameter is kept consistent across scales $k^* = k$ as well as the distance parameter $\delta^* = \delta$.

To create obstructions similar to the result of Example 5.8.1 we set parameters $\epsilon^* = \epsilon\frac{h}{h^*}$ and $\theta^* = \theta\frac{h^*}{h}$. The simulated stationary solution is shown in Figure 5.20

In general the results agree, with 3 primary obstructions forming. On the original grid there were 4 distinct formations, but on the refined grid the two smaller obstructions were aggregated into the larger obstructions. This may be due to the refined grid or perhaps due to the necessary changes to the parameters; if ϵ were slightly smaller it's possible there would still be 4 obstructions.

One can also see that the obstructions have rounded edges, they aren't as rectangular. The middle obstructions is able to wedge into the crevice on its top side.

Finding the right combination of parameters to work on the refined grid was not obvious to us. The appropriate method for scaling remains an open question.

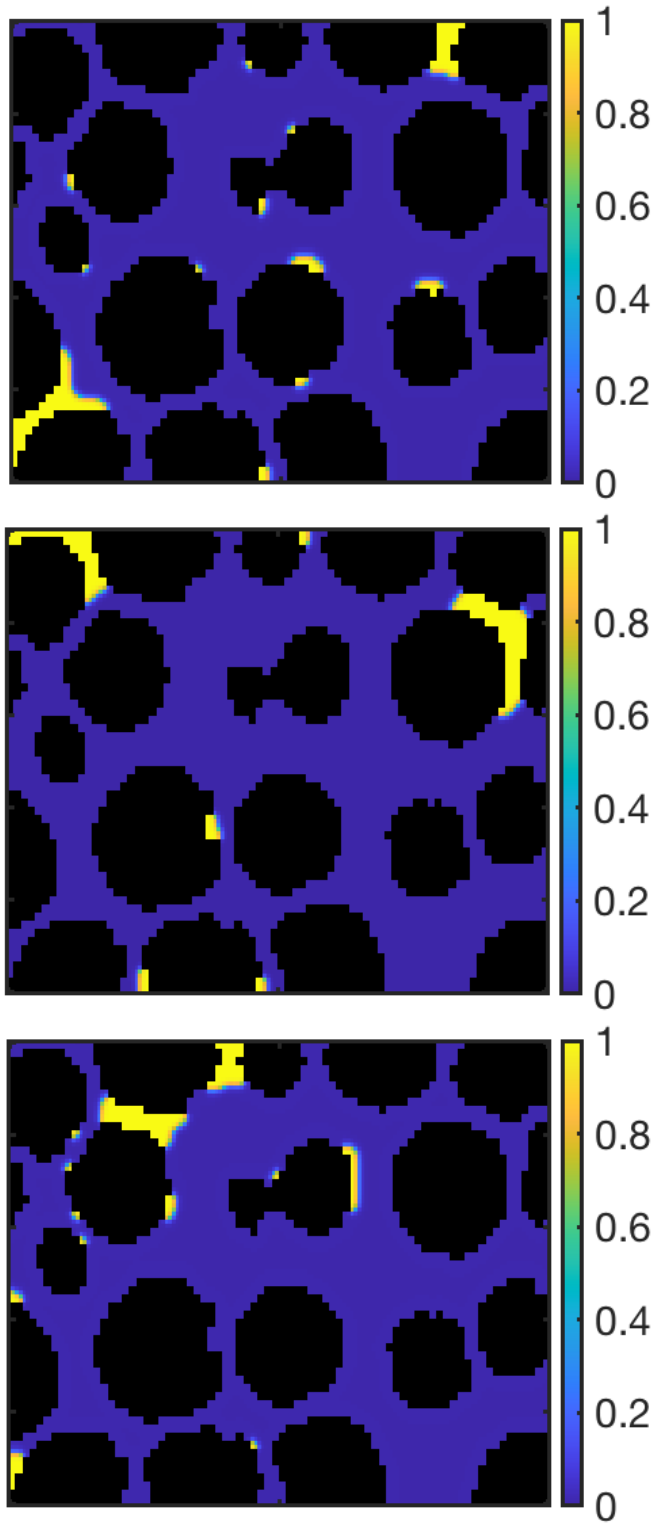

FIGURE 5.19: Pore coating obstruction generated by a method of constrained optimization. See 5.8.2. Black is the rock matrix, the color is $\psi(x)$, $x \in D_f$.

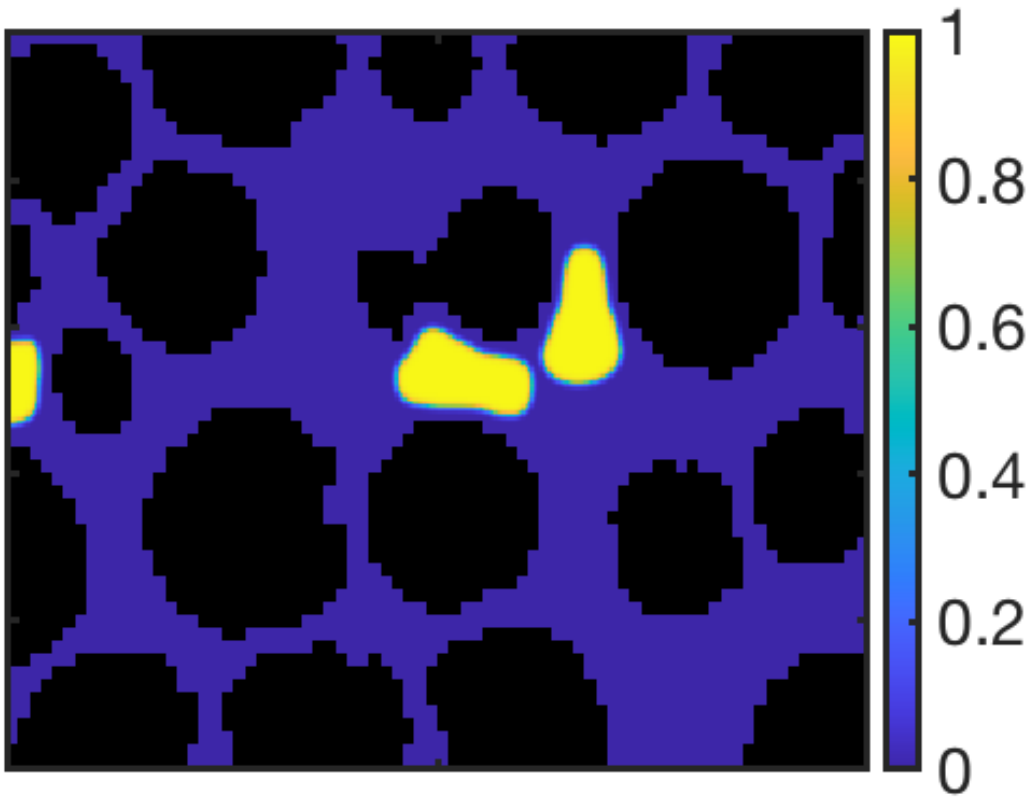

FIGURE 5.20: Pore filling obstruction generated on a refined grid. Compare with the top image of Figure 5.18. Black is the rock matrix, the color is $\psi(x)$, $x \in D_f$.

6 Using the Lattice method to generate obstructions

In this section we present our Markov Chain Monte Carlo (MCMC) method for generation obstructions, which we refer to as the Lattice model. To develop the background of MCMC methods we follow [28] and [46]. Some ideas below follow the work in [30] developed for the needs of multicomponent adsorption. We refer to this work for detailed references of earlier work on the topic by Monson et al.

We recall first the Ising model, which is used to construct low energy configurations of an $L \times M$ lattice. The lattice has nodes at Cartesian coordinates, $\langle i, j \rangle$, where $i, j = 1, \ldots, L$. A node is connected to all nodes with unit distance. For each node, $\langle i, j \rangle$, on the lattice we assign the value $x_{\langle i,j \rangle} = \pm 1$. With the use of an appropriate energy functional, called the Hamiltonian, we generate configurations, $X = (x_{\langle i,j \rangle})_{\langle i,j \rangle}$, that satisfy the Boltzmann distribution. A configuration is a event E in state space Ω, where Ω is set of all possible arrangements for the Lattice. Event E occurs with probability $P(E)$.

Inspired by the Ising model, we build a model for the generation of obstructions in a pore. This model allows for a fixed rock matrix and the generation of obstructions with a predefined aggregation patter, e.g. adjacent to or avoiding the rock matrix. The aggregation pattern is controlled by defining different Hamiltonians. Our Lattice model is used to generate large families of obstructed pore scale geometries that follow the Boltzman distribution, defined in what follows.

In Section 6.1 we introduce the probability background necessary for development of our Lattice model. In Section 6.2 we discuss the fundamentals of MCMC methods. In Section 6.3 we describe the Ising model. We conclude with Section 6.4 which describes our model and provides examples of how we use it to generate pore scale obstructions in porous media.

6.1 Notation

Define the probability space triple $(\Omega, \mathcal{S}, P)$, where Ω is a nonempty set, $\mathcal{S}$ is a $\sigma-$field of subsets of Ω, and P is a finite measure on the measurable space $(\Omega, \mathcal{S})$ with $P(\Omega) = 1$.

Let $E \subset \Omega$, that is E is an event in state space Ω. Then $P(E)$ is the probability that E occurs and $E \in \mathcal{S}$. Let $X \in \Omega$ be a real valued random vector, then the *cumulative distribution function* (cdf) of X is

$$\text{cdf}(x) = P(X \leq x).$$

For a discrete random variable, the *probability density function* (pdf) is

$$\text{pdf}(x) = P(X = x) = \lim_{\epsilon \to 0}(\text{cdf}(x) - \text{cdf}(x - \epsilon)).$$

We denote the continuous *uniform distribution* on interval (a, b) as $U(a, b)$. Every event in a uniform distribution is as likely as any other. The density function for the uniform distribution is

$$f(x) = \begin{cases} \frac{1}{b-a}, & a \leq x \leq b \\ 0, & \text{otherwise.} \end{cases}$$

We will most often use $U(0, 1)$.

A Markov chain is a sequence of random variables $(X_t)_{t \in \mathbb{N}}$ with the Markov property. That is, the probability of moving from state X_t to X_{t+1} depends only on X_t and no prior random variables in the sequence,

$$P(X_{t+1} = x | X_t = x_t, \ldots, X_1 = x_1) = P(X_{t+1} = x | X_t = x_t).$$

We use the shorthand notation $A \sim B$ to say that random variable A has the distribution of B, where B may be either a distribution or another random variable.

6.2 MCMC methods

Markov Chain Monte Carlo methods are a method for sampling from a known probability distribution, f. The MCMC methods discussed are designed in the style of

the Metropolis algorithm [31].

Given a state space, Ω, and a distribution, f, on Ω we can create a Markov chain $(X_t)_{t>N}$ whose entries follow the distribution f for N sufficiently large.

The methods require a proposal density, g, the target density, f, and an acceptance discipline, h. The acceptance discipline, $h : \Omega \times \Omega \to (0, 1]$, is a functional whose value is the likelihood of moving from one state to another. We often use $g \sim U$, due to ease of generating random numbers from U for proposed changes to the system state. We accept proposed changes with probability h, to generate a sequence, (X_t), such that, $X_t \sim f$.

The sequence of states (X_t) is a Markov chain. For a Markov chain generated by an MCMC method to converge to the invariant distribution, f, if must be that (X_t) is (1) aperiodic and (2) irreducible [28]. For an aperiodic Markov chain, there is no integer $D > 1$ such that for the chain to return to a state it must be in αD steps, $\alpha \in \mathbb{N}$. An irreducible Markov chain can move from a given state to any other, with sufficient steps.

The Lattice model we develop below is both aperiodic and irreducible. The method is aperiodic because each step in the method is reversible, so it can return to a state in one step. We consider irreducibility of the model below.

The initial state, X_0, is likely to be an uncommon state of the distribution f. The algorithm needs to run through some number of iterations before the sequence states are drawn from f. This is referred to as a "burn-in". There is no set length of the "burn-in"; it must be determined experimentally. In practice $(X_t)_{t>N} \sim f$ only for N sufficiently large.

6.3 Ising model

In this section, we describe the Ising model, as given in [46, §3.5].

The historical target of this model is magnetic materials. Consider an $L \times L$ Cartesian lattice, where each node, $\langle i, j \rangle$, represents an iron atom. Each atom has a spin, either $+1$ or -1, that denotes the magnetic direction of that atom, see Figure 6.1.

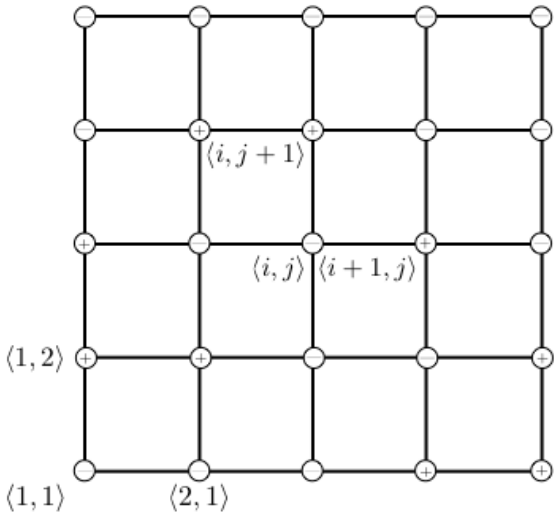

FIGURE 6.1: A 5×5 Cartesian lattice, with ± 1 spins at each node.

The Ising model finds spin configurations that follow the Boltzmann distribution,

$$f(x) = \frac{e^{-H(x)/(k_B T)}}{Z}, \tag{6.3.1}$$

where Z is the normalizing factor, $Z = \sum_{x \in \Omega} e^{E(x)/(k_B T)}$, and $H(x)$ is defined in Equation (6.3.3). Let $\beta = 1/(k_B T)$.

Let the proposal density be $g \sim U$, the target density be the Boltzmann distribution, Equation (6.3.1), and the acceptance discipline be

$$h = \min\left\{1, \frac{f(Y)}{f(X)}\right\} = \min\left\{1, \frac{\exp(-\beta H(Y))}{\exp(-\beta H(X))}\right\} = \min\{1, \exp(\beta(H(X) - H(Y)))\} \tag{6.3.2}$$

Let $X \in \Omega$ be an random variable, $X = (x_{\langle 1,1 \rangle}, \ldots, x_{\langle L,L \rangle})$, where $x_{\langle i,j \rangle} = \pm 1$, $i, j = 1, \ldots, L$, is the spin at each node. That is, our state space is $\Omega = \{-1, 1\}^{L^2}$. We will monitor the net magnetic state for each configuration, i.e. we want to know for each instance x of X, $M(x) = \sum_{\langle i,j \rangle} x_{\langle i,j \rangle}$.

Let $\Lambda_{\langle i,j \rangle}$ denote the neighbors of node $\langle i, j \rangle$. Define the Hamiltonian

$$H(x) = \frac{1}{2} \sum_{\langle i,j \rangle} \sum_{\langle r,s, \rangle \in \Lambda_{\langle i,j \rangle}} \delta\left(x_{\langle i,j \rangle} + x_{\langle r,s \rangle}\right), \tag{6.3.3}$$

where δ is the Dirac delta function. The Hamiltonian is a functional for measuring the total energy in a system. In this case, when the spin is the same between neighbors, the energy decreases. The Ising model finds low energy spin configurations.

The notion of neighbors has to account for what happens to the lattice points close to the boundary. One way to deal with this is to assume that the lattice is a torus, i.e., to implement periodic boundary conditions. Thus we include as neighbors of boundary nodes, those nodes on the opposite side of the lattice. For example,

$$\Lambda_{\langle 1,L\rangle} = \{\langle 2, L\rangle, \langle L, L\rangle, \langle 1, 1\rangle, \langle 1, L-1\rangle\}.$$

Choose X_0 randomly, update the Markov chain until the chain follows distribution f. The process for updating $X_t = x$ at each step is as follows

1. Select $\langle i, j\rangle$ uniformly from $\{1, \ldots, L\} \times \{1, \ldots, L\}$.
2. Propose new state y similar to x but with spin at $\langle i, j\rangle$ flipped
   (a) $y \leftarrow\!\shortmid x$
   (b) $y_{\langle i,j\rangle} \leftarrow\!\shortmid -y_{\langle i,j\rangle}$
3. Accept y with probability $h = \min\{1, \exp(\beta(H(x) - H(y))\}$
   (a) Select $u \sim U(0, 1)$
   (b) If $u \leq h$, then $X_{t+1} = y$
   (c) If $u > h$, then $X_{t+1} = x$

First we demonstrate how the algorithm above works. We use an example of a 2x2 lattice.

The equilibrium spin configurations depend on the temperature. If we vary the temperature in the Boltzmann distribution (6.3.1) we find different spin configurations to be most likely. Consider $\beta = 0.01$ (high temperature) and $\beta = 1$ (low temperature) to account for the variation in temperature. Observe in Figure 6.2 that the configurations favor a zero net spin when $\beta = .01$ and that when $\beta = 1$ the configurations are bimodal with extreme net spins most likely.

At higher temperatures the acceptance discipline tends to be greater than at lower temperatures. Physically, this property reflects that at higher temperatures all states

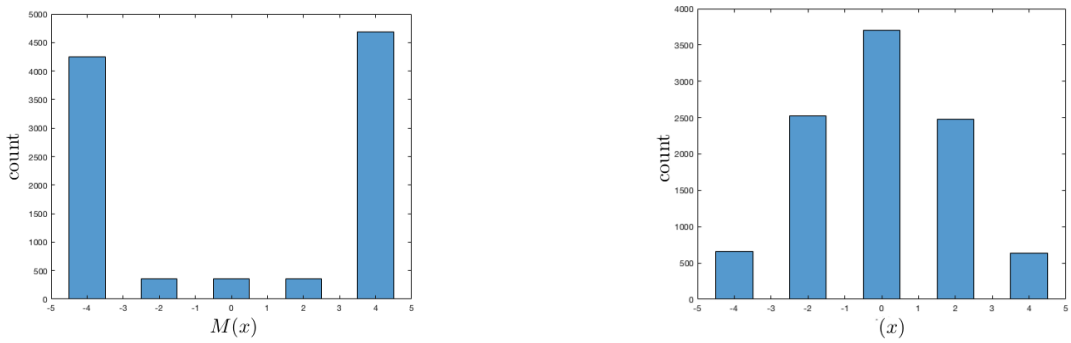

(a) $\beta = 1$ (b) $\beta = 0.01$

FIGURE 6.2: Probability density approximations of the net spin on a 2×2 lattice.

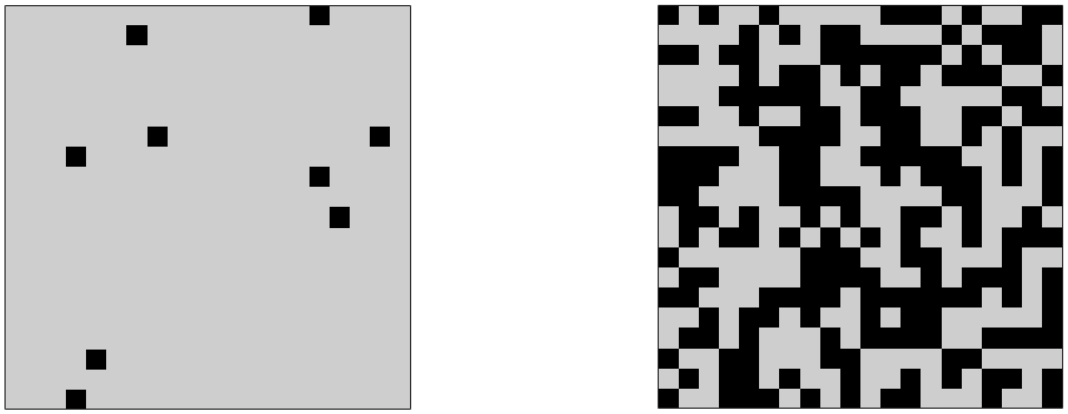

(a) $\beta = 1$ (b) $\beta = 0.01$

FIGURE 6.3: Typical spin configurations on a 20×20 lattice. Black is spin down $(-)$, gray is spin up $(+)$.

are reasonably likely to occur. At lower temperatures states that favor one charge or another are more likely. We present in Figure 6.3 typical spin configurations on lattices of $L = 20$ for different values of β. When $\beta = 1$ one can see that a likely state is in mostly spin up. When $\beta = 0.01$ one can see that the spin configuration has less order.

In Figure 6.4 we show the energy at each MCMC step of the system for a 20×20 lattice, with $\beta = 0.01$. For this system the burn in period is brief.

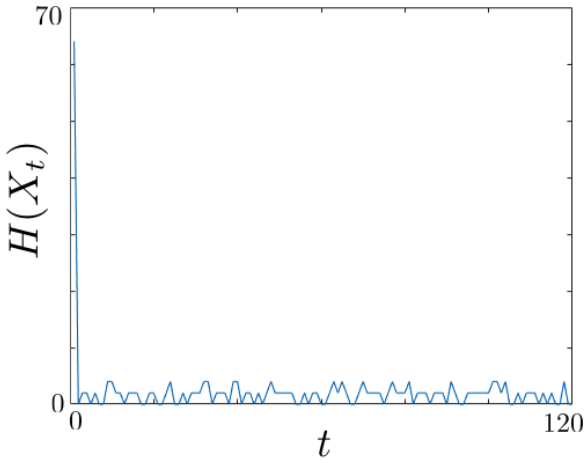

FIGURE 6.4: The Energy, $H(t)$, for each step of the Ising method on a 20×20 lattice, $\beta = 0.01$.

6.4 Lattice model to generate geometries with obstructions

In this section we introduce the Lattice model we use to generate obstructions in a pore domain D. We partition the domain into the rock matrix and the flow domain, $D = D_{r,f}$. We further partition the flow domain into void space and obstruction, $D_f = D_{v,o}$ Define the obstruction volume to be the ratio of obstruction to flow domain space,

$$V_o = \frac{|D_o|}{|D_f|} = \frac{1}{\phi}\frac{|D_o|}{|D|}. \tag{6.4.1}$$

To generate obstructions in D, we modify the Ising model in several important ways. We (1) fix the rock matrix and flow domain, D_r and D_f respectively, (2) fix the obstruction volume, V_o, (3) now have three species, void, rock, and obstruction.

By fixing the rock matrix, we are only changing the position of void and obstruction. This is because we are considering fixed solid matrices and trying to find likely obstruction configurations in the flow domain.

We will consider a range of obstruction volumes. Once V_o is fixed, the method rearranges the obstructions and void to find likely configurations. This is analogous to fixing the net magnetic spin in the Ising model.

With three species several interfaces can arise. In the design of the Hamiltonian

functional we will include weights for the interaction at each type of interface, allowing for control over the configuration of obstructions. We use this to create both obstructions that favor adjacency to the rock matrix and obstructions that aggregate away from the rock matrix.

Let a 2 dimensional porous media domain be uniformly partitioned into $L \times M$ voxels. For the Lattice method, we represent the domain as an $L \times M$ Cartesian lattice, where each lattice node denotes the material in the corresponding cell. We assign a value to each material as follows,

$$\text{void} \leftrightarrow 0, \quad \text{rock} \leftrightarrow 1, \quad \text{obstruction} \leftrightarrow 2. \tag{6.4.2}$$

Let $\Theta \in L \times M$ be nodes corresponding to cells in D_f. Then, with state space $\Omega = \{0, 2\}^{\Theta}$ the method is irreducible.

Let $\Lambda_{\langle i,j \rangle}$ denote the neighbors of node $\langle i, j \rangle$. Let $\Lambda^2_{\langle i,j \rangle}$ denote the next nearest neighbors of node $\langle i, j \rangle$,

$$\begin{aligned}\Lambda^2_{\langle i,j \rangle} =& \{\langle i+2, j \rangle, \langle i-2, j \rangle, \langle i, j+2 \rangle, \langle i, j-2 \rangle, \\ & \langle i+1, j+1 \rangle, \langle i-1, j+1 \rangle, \langle i+1, j-1 \rangle, \langle i-1, j-1 \rangle\}.\end{aligned} \tag{6.4.3}$$

Define a symmetric weighting function

$$\omega(x_{\langle i,j \rangle}, x_{\langle r,s \rangle}) = \begin{cases} 0, & \text{if } x_{\langle i,j \rangle} = x_{\langle r,s \rangle} & \text{(6.4.4a)} \\ w_{ro} & \text{if } x_{\langle i,j \rangle} = 1,\ x_{\langle r,s \rangle} = 2 & \text{(6.4.4b)} \\ w_{rv} & \text{if } x_{\langle i,j \rangle} = 1,\ x_{\langle r,s \rangle} = 0 & \text{(6.4.4c)} \\ w_{vo} & \text{if } x_{\langle i,j \rangle} = 0,\ x_{\langle r,s \rangle} = 2. & \text{(6.4.4d)} \end{cases}$$

Now, we define our nearest neighbor Hamiltonian,

$$H_1(x) = \frac{1}{2} \sum_{\langle i,j \rangle} \sum_{\langle r,s \rangle \in \Lambda_{\langle i,j \rangle}} \omega(x_{\langle i,j \rangle}, x_{\langle r,s \rangle}), \tag{6.4.5}$$

where the coefficient of $1/2$ is necessary because this notation includes each interface twice.

We also define a next-nearest neighbor Hamiltonian,

$$H_2(x) = \frac{1}{2} \sum_{\langle i,j \rangle} \left(\sum_{\langle r,s \rangle \in \Lambda_{\langle i,j \rangle}} \omega(x_{\langle i,j \rangle}, x_{\langle r,s \rangle}) + W \sum_{\langle r,s \rangle \in \Lambda^2_{\langle i,j \rangle}} \omega(x_{\langle i,j \rangle}, x_{\langle r,s \rangle}) \right), \tag{6.4.6}$$

where W is a weight for the next-nearest neighbor interactions.

We will use again the Boltzmann distribution, Equation (6.3.1), as the target distribution. The proposal density is $g \sim U$ and acceptance discipline is $h = \min\{1, \exp(\beta(H(X) - H(Y)))\}$. We again use periodic boundary conditions.

After randomly generating initial state, X_0, the process for updating $X_t = x \in \Omega$ at each step is as follows

1. Select $\langle i, j\rangle, \langle r, s\rangle$ uniformly from Θ.
2. Propose new state y, same as x but with spins at $\langle i, j\rangle$ and $\langle r, s\rangle$ swapped
   (a) $y \leftarrow\!\shortmid x$
   (b) $y_{\langle i,j\rangle} \leftarrow\!\shortmid x_{\langle r,s\rangle}$
   (c) $y_{\langle r,s\rangle} \leftarrow\!\shortmid x_{\langle i,s\rangle}$
3. Accept y with probability $h = \min\{1, \exp(\beta(H(x) - H(y)))\}$
   (a) Select $u \sim U(0, 1)$
   (b) If $u \leq h$, then $X_{t+1} = y$
   (c) If $u > h$, then $X_{t+1} = x$

We extend the Markov chain until we are satisfied we're through the burn-in process. We then save the final state of the Markov chain as our pore with an obstruction.

Example 6.4.1 (Hydrate-like obstruction in a single pore)**.** Let $L = M = 50$, $\beta = 1$, $W = 1/2$, and $V_o = 0.1$. We use the next-nearest neighbor Hamiltonian, H_2.

We first consider the generation of obstructions that avoid the rock matrix and tend towards clumping. For this, set the weights

$$w_{ro} = 100, \qquad w_{rf} = 1, \qquad w_{fo} = 50. \tag{6.4.7}$$

In Figure 6.5, we show the progression of the Lattice model process for generating the obstruction. We see that the obstruction cells quickly for conglomerates, but it takes many iterations for the process to stabilize with a single clump.

Example 6.4.2 (Biofilm-like obstruction in a single pore)**.** We next consider the generation of obstructions that favor adjacency to the rock matrix. We use the same geometry

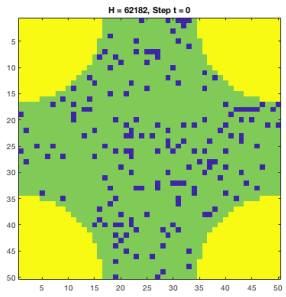

(a) Initial state, X_0

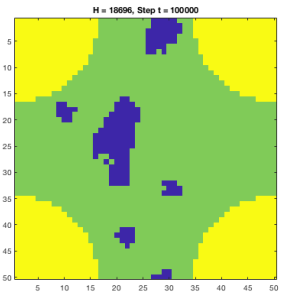

(b) X_{100000}

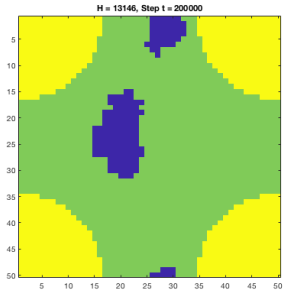

(c) X_{200000}

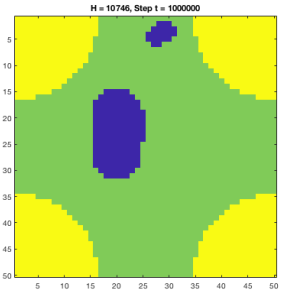

(d) $X_{1000000}$

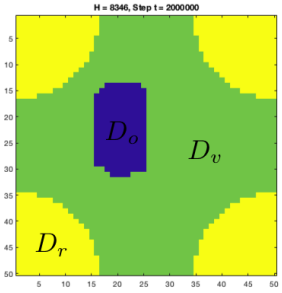

(e) $X_{2000000}$

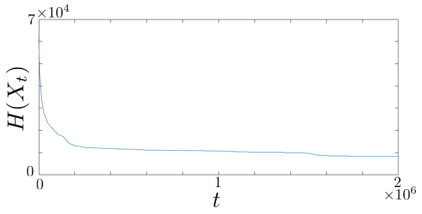

(f) Hamiltonian, $H(X_t)$.

FIGURE 6.5: States of the Lattice model process for the formation of an obstruction with weights given by Equation (6.4.7). Rock matrix, D_r, is yellow, void space, D_v, is green, and the obstruction, D_o is purple.

as in the last example, but set the weights as follows

$$w_{ro} = 1, \qquad w_{rf} = 100, \qquad w_{fo} = 50. \tag{6.4.8}$$

These weights also discourage the formation of fingers of obstruction. In Figure 6.6, we show the progression of the Lattice model process for generating the obstruction. We can see that the obstruction cells form a thin layer along the rock matrix. The burn-in time for this process is much shorter than in our previous example.

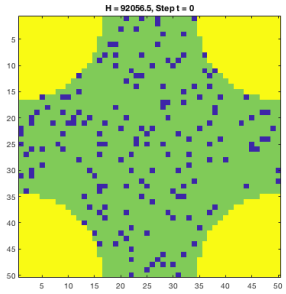

(a) Initial state, X_0

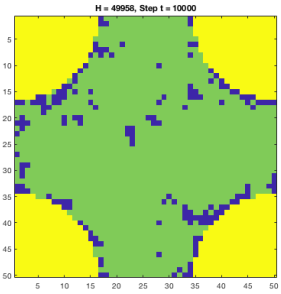

(b) X_{10000}

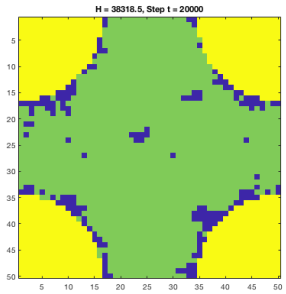

(c) X_{20000}

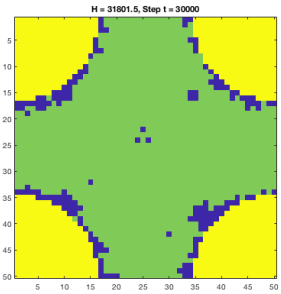

(d) X_{30000}

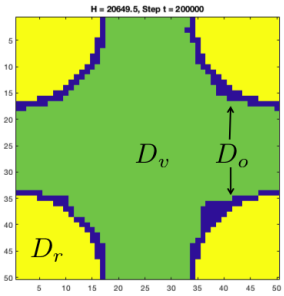

(e) X_{200000}

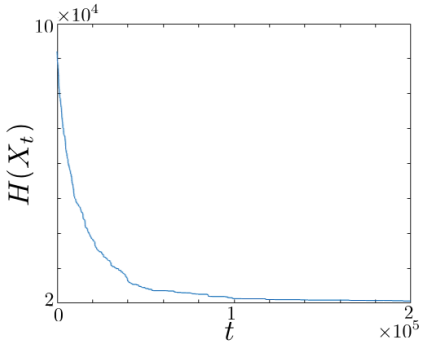

(f) Hamiltonian, $H(X_t)$.

FIGURE 6.6: States of the Lattice model process for the formation of an obstruction with weights given by Equation (6.4.8). Rock matrix, D_r, is yellow, fluid space, D_v, is green, and the obstruction, D_o is purple.

7 Results

In this chapter we present our main results. We combine the flow and transport methods of Chapter 3 with the models for generating realizations of geometries with obstructions of Chapters 5 and 6. The methods of Chapters 5 and 6 produce independent realizations of domain geometries on which we simulate flow and transport, and then upscale the results.

We complete several experiments to infer how Darcy scale results are impacted by geometry changes at the pore scale. In particular we study (1) permeability distributions as a function of obstruction volume, (2) change in permeability relative to pore scale breakthrough, (3) tortuosity distributions as a function of obstruction volume, and (4) a comparison of pore scale and Darcy scale breakthrough curves. By completing these experiments for multiple types of obstructions we see that the permeability is highly dependent on the type of obstruction growing at the pore scale. In particular, we confirm that the permeability is not merely a function of porosity, but is rather highly dependent on how the geometry is changing.

The process in our experiments is as follows.

(1) We start with a porous media domain $D = D_{f,r}$. This domain may be either a many-pore model or a smaller single-pore model. The two domains we use are shown in Figure 7.1 We fix the desired obstruction volume, V_o. For the CLPS model this means the constraint on the total phase parameter is V_o,

$$\int_D \psi = V_o.$$

(2) Then we choose the method we will use to create the obstructions. Here the choice is between either the phase separation method of Chapter 5 or the Lattice model of Chapter 6.

(3) Next we choose a type of obstruction that we are trying to emulate, i.e., we choose from either biofilm, hydrate or colloid like obstructions. The parameters of the model are set based on the obstruction type chosen.

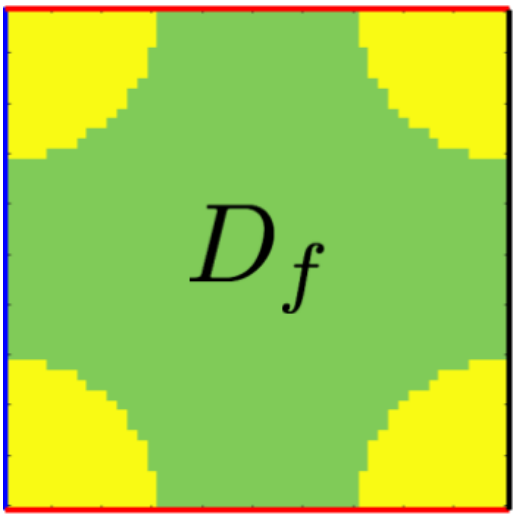

(a) Domain D for single-pore experiments. D_f is green, D_r is yellow.

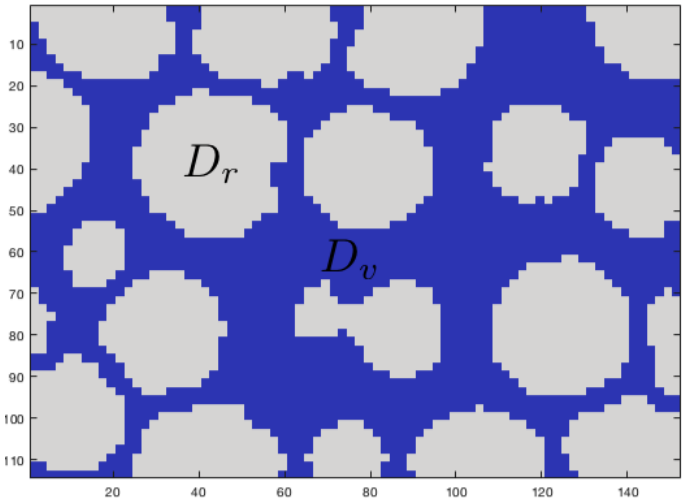

(b) Domain D for many-pore experiments. This domain is an imaged REV from [35]. D_v is blue and D_r is gray. With no obstructions $D_f = D_v$.

FIGURE 7.1: Experimental domains prior to obstruction formation.

(4) We initialize the model in random fashion and run the model to generate the first obstructed geometry. Next we repeat the simulation with new random initial conditions until we have generated some desired number of obstructed geometries.

(5) On the unobstructed geometry and each of the obstructed geometries we solve for Stokes flow in D_f with HybGe-Flow3D [14], explained in Section 3.4.4. Our focus is on illustrating our ideas and on proof-of-concept, thus we set up experiments only for the case when the flow has one primary direction.

(6) For each flow solution we simulate the transport through the pore scale domain D_f. We use both the Eulerian and Lagrangian frames of reference; see the methods described in Section 3.5. From the transport solutions we are able to calculate the breakthrough curves (3.2.7) and (3.2.5), and the tortuosity $\mathbf{T}$, as described in Section 3.6.

(7) Last, we upscale to find volumetric flow rate U, and permeability K, using the method described in Section 3.3. To calculate U we may use Dupuit's relation (3.3.2) or the Dupuit's relation modified by tortuosity (3.3.7). We state which we are using. Lastly, we calculate the Darcy scale transport and breakthrough as described in Section 3.5.

To infer from experimental results we often consider how the obstructions changed quantities of interest relative to the unobstructed pore. To distinguish the quantities associated with the unobstructed pore we denote them with a subscript 0. For example, the upscaled permeability of the unobstructed pore is K_0.

In Section 7.1 we calculate permeability distributions as functions of obstruction volumes. In Section 7.2 we compare how permeability changes relative to the changes in pore scale breakthrough. In Section 7.3 we calculate tortuosity distributions as functions of obstruction volumes. In Section 7.4 we compare the breakthrough curves of pore scale and Darcy scale transport.

7.1 Permeability distributions in single pore geometries

The first results we present are on permeability distributions as a function of obstruction volume. From this experiment we see how different types of obstructions with different obstruction volumes impact the permeability of an idealized pore. We also use this experiment to compare the upscaled permeability results derived from our two methods for generating obstructions.

For the experiments in this section we use an idealized pore for domain D, Figure 7.1a. The flow inlet is the left side of the domain, the outlet is the right side. At the top and bottom of the domain we assume the no slip condition for the velocities.

We execute this experiment with both the CLPS model and the Lattice model. With the CLPS model we consider two types of obstructions: biofilm-like and hydrate-like. With the lattice model we consider three types of obstructions: biofilm-like, hydrate-like, and colloidal. We generate obstructed geometries for each type of obstruction and for each of three different values of obstruction volume $V_o = 0.1,\ 0.2,\ 0.3$..

For a given type of obstruction and obstruction volume we generate $M = 100$ obstructed geometries. Next we analyze the results of the M independent simulations $i = 1, 2, \ldots M$ of the geometries with obstructions. For each geometry $D_f^{(i)}$ we calculate the permeability $K_{(i)}$, where the upscaling was completed using Dupuit's relation (3.3.2).

The results of this experiment are given relative to the permeability of the unobstructed pore, that is we present $K_{(i)}/K_0$. The first result presented is a histogram. We use the Matlab function `histogram` to partition and present the calculated relative permeabilities $(K_{(i)}/K_0)_i$. The second result is the mean and standard deviation of $(K_{(i)}/K_0)_i$

7.1.1 Biofilm-like obstructions

First we complete the experiment with biofilm-like obstructions. We explain the parameters used for both the CLPS and Lattice models. We then compare the results derived from the use of each model.

Example 7.1.1 (Lattice model)**.** To create the biofilm-like obstructions with the Lattice

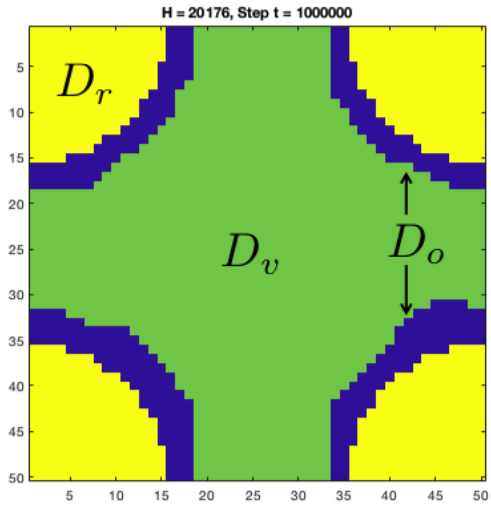

FIGURE 7.2: Biofilm-like obstruction with Lattice model. $V_o = 0.2$. For experiment in Section 7.1.1.

model for this experiment we set the parameters as follows

$$\omega = \begin{cases} w_{vr} = 100, \\ w_{ro} = 1, \\ w_{vo} = 50. \end{cases}$$

For illustration we show an example biofilm obstruction in D_f in Figure 7.2.

The permeability change as a function of the obstruction volume is shown in Figure 7.3. We see that the histograms appear somewhat like a Gaussian distribution. The change in the mean of $(K_{(i)}/K_0)_i$ is near linear, dropping consistently closer to 0 as V_o increases. The standard deviation of $(K_{(i)}/K_0)_i$ is small, but slightly increasing as V_o increases. As the biofilm grows larger it can have a slightly wider array of impact on the permeability. One can infer that biofilm formation in porous media may cause more predictable changes in permeability.

Example 7.1.2 (CLPS model)**.** To create the biofilm-like obstructions with the CLPS model for this experiment we set the parameters as follows

$$\epsilon = 0.1, \qquad \theta = 0.25, \qquad \delta = 0.1.$$

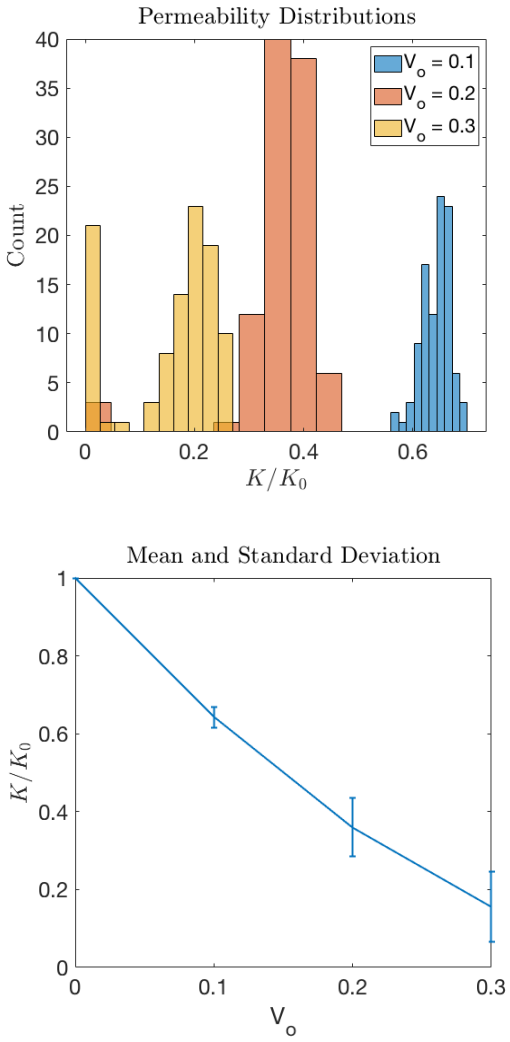

FIGURE 7.3: Relative change in permeability due to Lattice model biofilm-like obstructions, see Section 7.1.1. Top: histogram of $(K_{(i)})_i$ values for 3 values of V_o. Bottom: mean and standard deviation of $(K_{(i)})_i$ for 3 values of V_o.

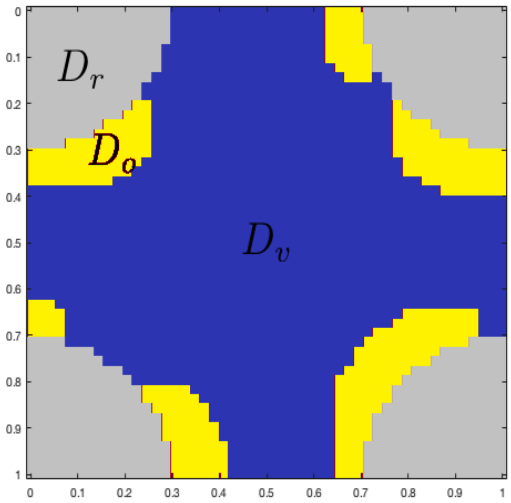

FIGURE 7.4: Biofilm-like obstruction generated with CLPS model. $V_o = 0.2$. For experiment in Section 7.1.1.

For illustration we show an example biofilm obstruction in D_f in Figure 7.4. We see that the biofilm simulation produces 6 distinct "colonies" and does not cover the entire rock-fluid interface. This is in contrast with the Lattice model, which does cover the entire rock-fluid interface.

The permeability change as a function of the obstruction volume is shown in Figure 7.5. The histogram for $V_o = 0.1$ shows a Gaussian-like distribution. For the higher values of V_o, we see that certain values are common, but there are also zero permeability events. The change in the mean of $(K_{(i)}/K_0)_i$ follows a similar trajectory to that in the case where the Lattice model is used to generate obstructions, Figure 7.3. However, the CLPS model shows a greater variance in $(K_{(i)}/K_0)_i$.

7.1.2 Hydrate-like obstructions

First we complete the experiment with biofilm-like obstructions. We explain the parameters used for both the CLPS and Lattice models. We then compare the results derived from the use of each model.

Example 7.1.3 (Lattice model)**.** To create the hydrate-like obstructions with the Lat-

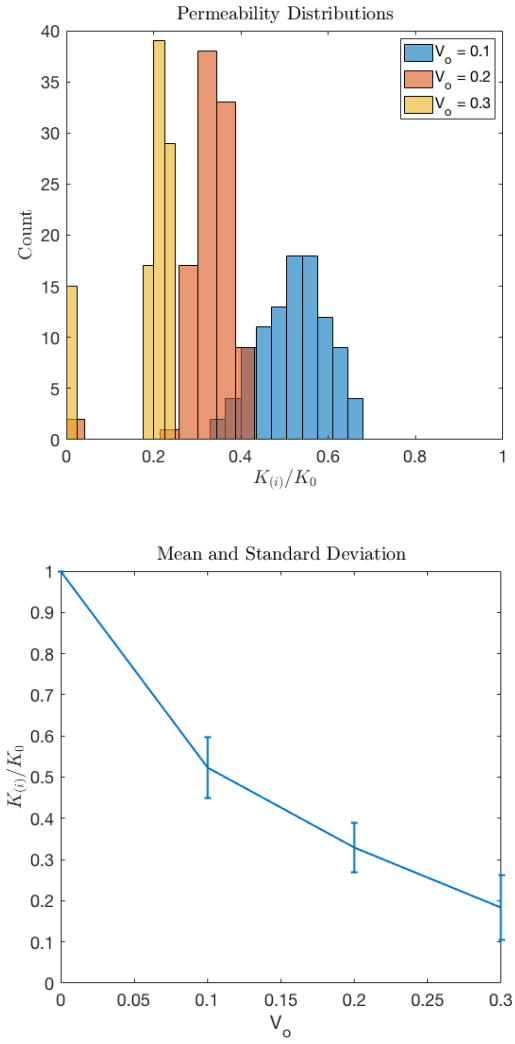

FIGURE 7.5: Relative change in permeability due to CLPS generated biofilm-like obstructions, see Section 7.1.1. Top: histogram of $(K_{(i)})_i$ values for 3 values of V_o. Bottom: mean and standard deviation of $(K_{(i)})_i$ for 3 values of V_o.

tice model for this experiment we set the parameters as follows,

$$\omega = \begin{cases} w_{vr} = 1, \\ w_{ro} = 100, \\ w_{vo} = 50. \end{cases}$$

We show an example hydrate-like obstruction in D_f in Figure 7.6. The experiments use obstruction volumes $V_o = 0.1,\ 0.2,\ 0.3$.

The permeability distribution change as a function of the obstruction volume is shown in Figure 7.7. We see that the histograms show a distribution skewed towards 0, perhaps like a Poisson distribution. The change in the mean of $(K_{(i)}/K_0)_i$ is sharp, dropping nearly 85% with $V_o = 0.1$. The decrease in the mean levels off, as V_o increases from 0.1.

The standard deviation of $(K_{(i)}/K_0)_i$ is quite large, suggesting that where the hydrate forms in the pore plays a large role in how it impacts permeability. Consider the obstruction formation in Figure 7.6 with $V_o = 0.2$. Since the flow is unidirectional, moving from left to right, the fluid needs to fit through the two small openings on the left side of the obstruction. One can imagine how an obstruction forming in either the top or bottom of the pore would be less obstructive to the flow. One can infer that hydrate formation in porous media may cause less predictable changes in permeability.

Example 7.1.4 (CLPS model)**.** To create the hydrate-like obstructions with the CLPS model for this experiment we set the parameters as follows

$$\epsilon = 0.28, \qquad \theta = -0.3, \qquad \delta = 0.1.$$

For illustration we show an example hydrate obstruction in D_f in Figure 7.8. In this case, the model reached an equilibrium point with two distinct hydrate-like formations.

Results for this experiment are shown in Figure 7.9. This experiment found a drop in relative permeability of about one order of magnitude at $V_o = 0.1$. Comparing the mean of $(K_{(i)}/K_0)_i$ with the case where obstructions are generated with the lattice model, Figure 7.7, we see good agreement. The CLPS model, however, has a smaller standard deviation in $(K_{(i)}/K_0)_i$.

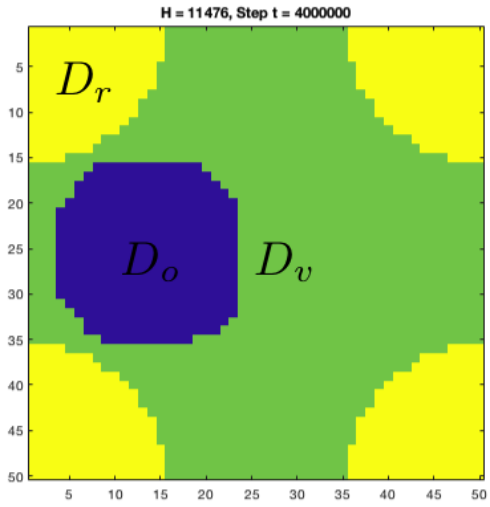

FIGURE 7.6: Hydrate-like obstruction with $V_o = 0.2$ for experiment in Section 7.1.2.

7.1.3 Colloidal obstructions

To create colloidal obstructions we use only the Lattice model. To create the colloidal obstructions for this experiment we set the parameters as follows,

$$\omega = \begin{cases} w_{vr} = -1, \\ w_{ro} = -1, \\ w_{vo} = -1. \end{cases}$$

We show an example colloidal obstruction in D_f in Figure 7.10. The experiments use obstruction volumes $V_o = 0.05,\ 0.1,\ 0.2$.

The permeability distribution change as a function of the obstruction volume is shown in Figure 7.11. The mean relative permeability change is about two orders of magnitude with $V_o = 0.05$. We suspect that the impact of the colloidal obstructions is overstated due to the experiments being in two dimensions. With flow in a three dimensional domain there are more pathways within which the flow may move around an obstructed cell.

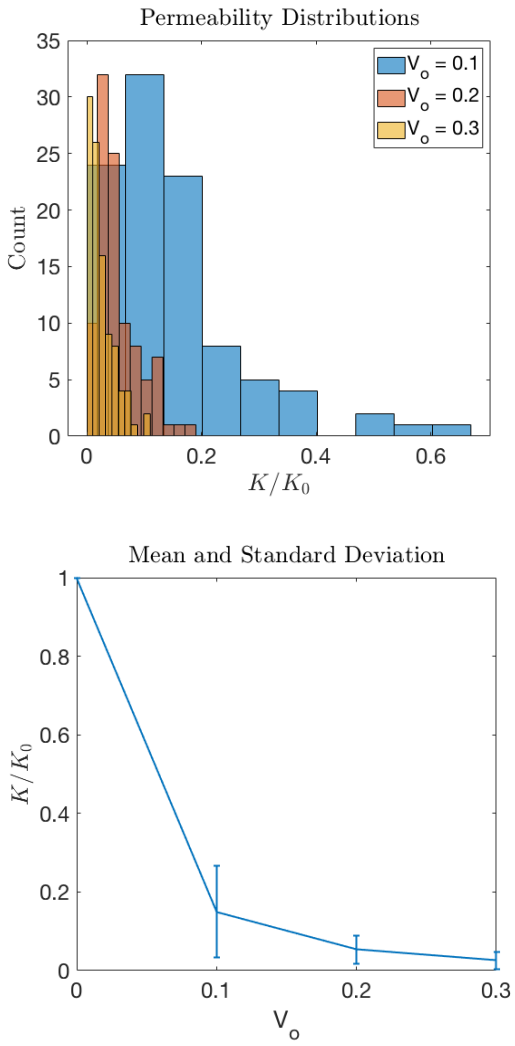

FIGURE 7.7: Relative change in permeability due to hydrate-like obstructions, see Section 7.1.2. Top: histogram of $(K_{(i)})_i$ for 3 values of V_o. Bottom: mean and standard deviation of $(K_{(i)})_i$ for 3 values of V_o.

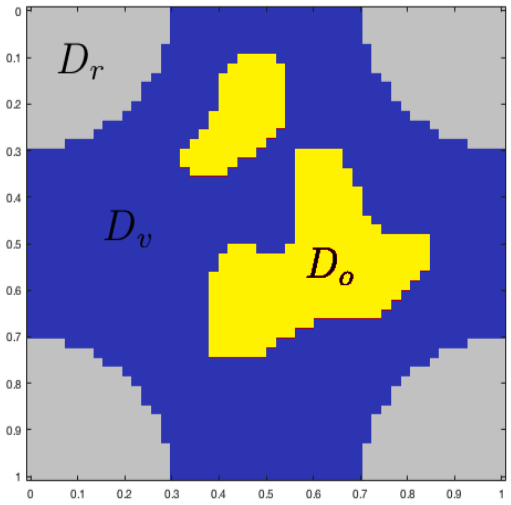

FIGURE 7.8: Hydrate-like obstruction generated with CLPS model.$V_o = 0.2$. For experiment in Section 7.1.2.

7.2 Permeability vs. pore scale breakthrough in many pore geometries

The next experiment we present compares the relative change in permeability with the pore scale break through. To characterize break through in this experiment we record the time at which the outflow reaches some fixed ratio of the inflow of the transported species. One should expect that for a less permeable porous media that amount of time should experience some correlating change. This experiment studies that correlation.

For the experiments in this section we use an REV from [35], shown in Figure 7.1b. The flow inlet is the left side of the domain, the outlet is the right side. The fluid solid interface, and the top and bottom of the domain enforce no slip conditions for the velocity.

We consider two types of obstructions, biofilm-like and hydrate-like. The obstructed geometries are generated with the Lattice model of Section 6. We generate obstructed geometries for each type of obstruction with $V_o = 0.05$.

For a given type of obstruction we generate $M = 100$ obstructed geometries. Next we analyze the results of the M independent simulations $i = 1, 2, \ldots, M$ of the

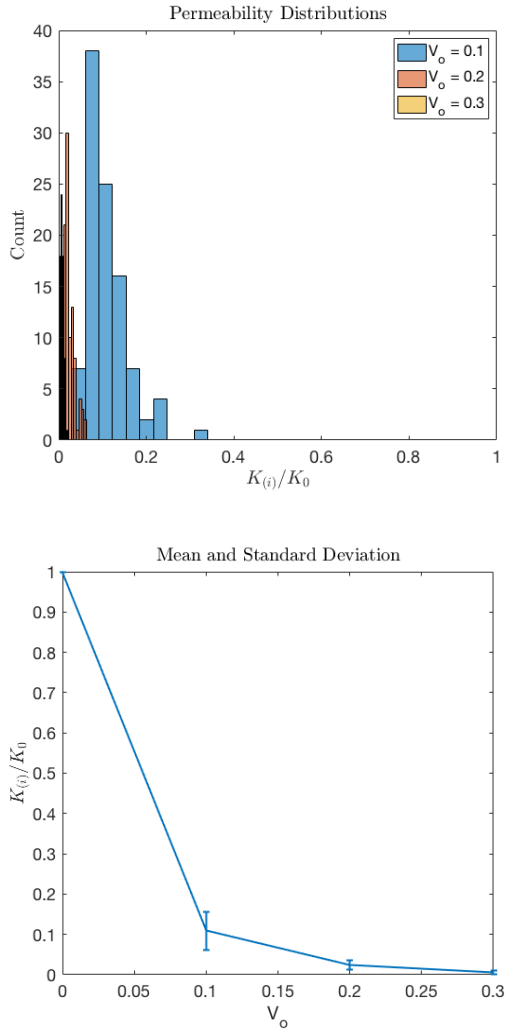

FIGURE 7.9: Relative change in permeability due to hydrate-like obstructions, see Section 7.1.2. Top: histogram of $(K_{(i)})_i$ for 3 values of V_o. Bottom: mean and standard deviation of $(K_{(i)})_i$ for 3 values of V_o.

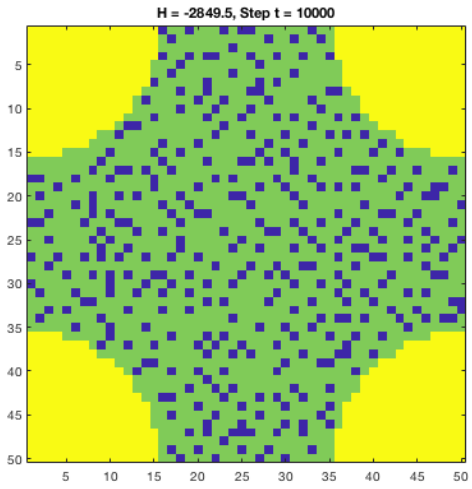

FIGURE 7.10: Biofilm-like obstruction with $V_o = 0.2$ for experiment in Section 7.1.3.

geometries with obstructions. For each geometry $D_f^{(i)}$ we calculate the permeability $K_{(i)}$, where the upscaling was completed using Dupuit's relation (3.3.2).

For each geometry we also calculate transport solutions in the Eulerian frame of reference. From the transport solutions, we calculate the breakthrough curve (3.2.5).

We characterize the breakthrough curve for each obstructed geometry as follows. Define the $\alpha-$breakthrough time $T^{(\alpha)}$ as follows

$$T^{(\alpha)} = t \text{ such that } \frac{\int_{\Gamma_{out}} (u \cdot n)c}{\int_{\Gamma_{in}} (u \cdot n)c} = \alpha, \tag{7.2.1}$$

where $0 \leq \alpha \leq 1$. $T^{(\alpha)}$ is the time where the ratio of transport of c out of the pore to transport of c into the pore is equal to α. That is, $T^{(\alpha)}$ is the time when the pore is at $\alpha * 100$ percent of the total possible outflux. We denote the $\alpha-$breakthrough time for simulation i with a subscript i, $T_i^{(\alpha)}$. Note that $B(t)$ is monotonically increasing in our experiments.

We note that for many of the results in this section that $T_{(i)}^{\alpha}/T_0^{\alpha} < 1$. This counter-intuitive result would suggest that due to obstructions the breakthrough is happening quicker. This experimental result occurs because of Lemma 3.3.1. By restricting the size of the flow domain while keeping inflow constant, the fluid in the fluid domain must move faster through the pore to maintain mass balance.

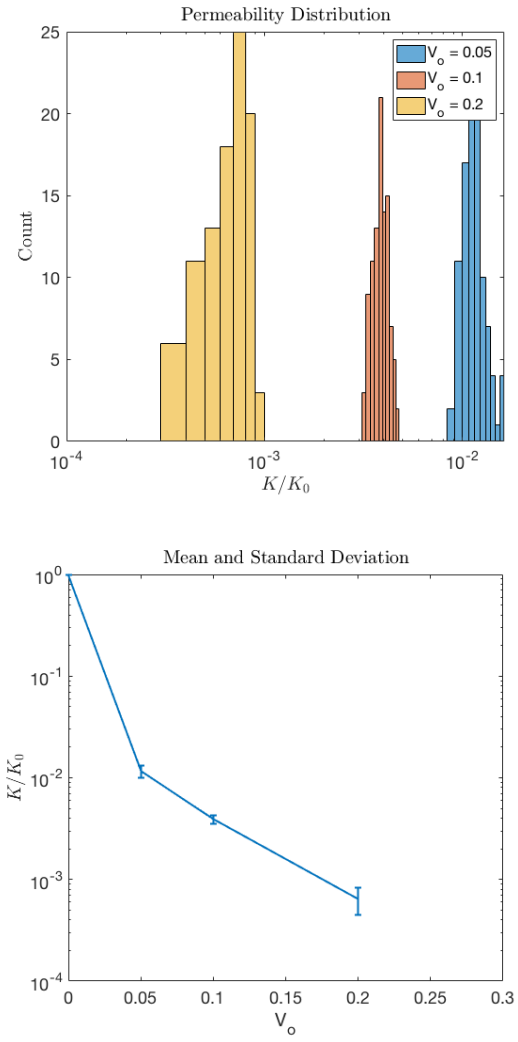

FIGURE 7.11: Relative change in permeability due to colloidal obstructions, see Section 7.1.3. Top: histogram of $(K_{(i)})_i$ for 3 values of V_o. Bottom: mean and standard deviation of $(K_{(i)})_i$ for 3 values of V_o.

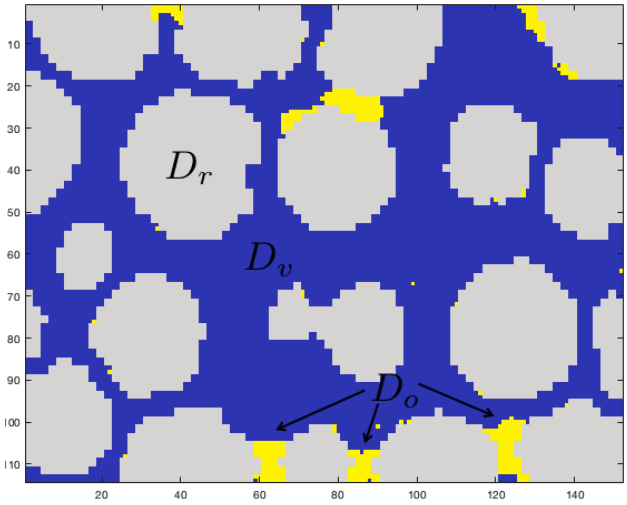

FIGURE 7.12: Biofilm-like obstruction for experiment in Section 7.2.1. The obstruction is yellow, the solid matrix is gray and the void space is blue.

The results of this experiment are calculated relative to the unobstructed pore. The results are presented as scatter plots of $K_{(i)}/K_0$ vs $T^{\alpha}_{(i)}/T^{\alpha}_0$. We include also a least squares fit to the data as a solid gray line.

7.2.1 Biofilm-like obstructions

To create the biofilm-like obstructions for this experiment we set the parameters as follows,

$$\omega = \begin{cases} w_{vr} = 1.2, \\ w_{ro} = 1, \\ w_{vo} = 1. \end{cases}$$

We show an example biofilm-like obstruction in D_f in Figure 7.12.

We present results for $\alpha = 0.8$ and $\alpha = 0.95$ in Figure 7.13. When $\alpha = 0.8$ the trend line suggests a correlation between $T^{\alpha}_{(i)}$ and $K_{(i)}$, as the slope is about 0.6. However, when $\alpha = 0.95$ this trend has started to disappear and the trend line approaches level. Note in particular the outlier where the permeability has dropped nearly 60% while the breakthrough time has dropped less than 20%; this is likely due to the clogging of certain throats in the REV.

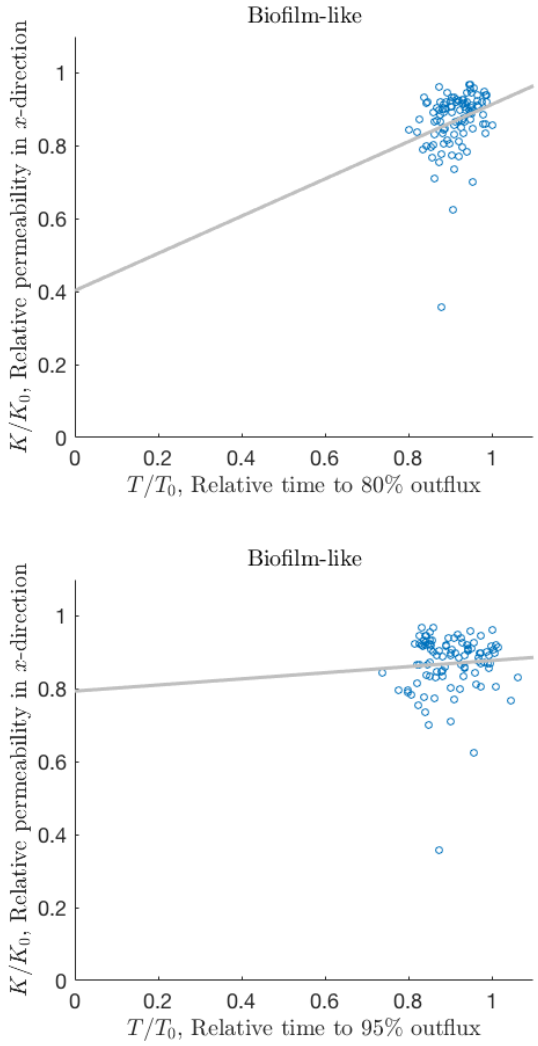

FIGURE 7.13: Relative change in K against the relative change in $T^{(\alpha)}$ due to biofilm-like obstructions. See Section 7.2.1. Top: $\alpha = 0.8$. Bottom: $\alpha = 0.95$.

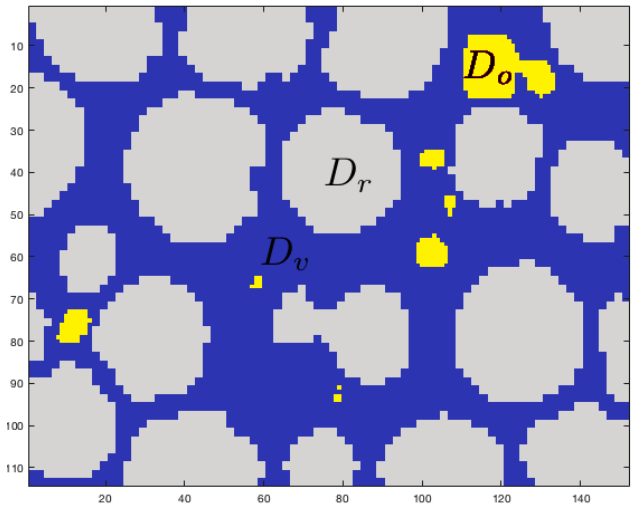

FIGURE 7.14: Hydrate-like obstruction for experiment in Section 7.2.2. The obstruction is yellow, the solid matrix is gray and the void space is blue.

7.2.2 Hydrate-like obstructions

To create the hydrate-like obstructions for this experiment we set the parameters as follows,

$$\omega = \begin{cases} w_{vr} = 1, \\ w_{ro} = 10, \\ w_{vo} = 5. \end{cases}$$

We show an example of hydrate-like obstruction in D_f in Figure 7.14.

We present results for $\alpha = 0.8$ and $\alpha = 0.95$ in Figure 7.15. For the case with hydrate-like obstructions we see the opposite of the biofilm-like obstructions, in that the trend line gets steeper the experiment progresses from $\alpha = 0.8$ to $\alpha = 0.95$. There is a dramatic vertical cloud of points around $T_{(i)}^{(0.8)}/T_0^{(0.8)} \approx 1$, showing that there can be a wide range of changes in the permeability without changing the breakthrough time much.

For both $\alpha = 0.8$ and $\alpha = 0.95$ the spread of the points on the scatter plots are quite wide. This supports the notion discussed in the experiment in Section 7.1.2 that hydrate formation in porous media may cause less predictable changes in flow and transport.

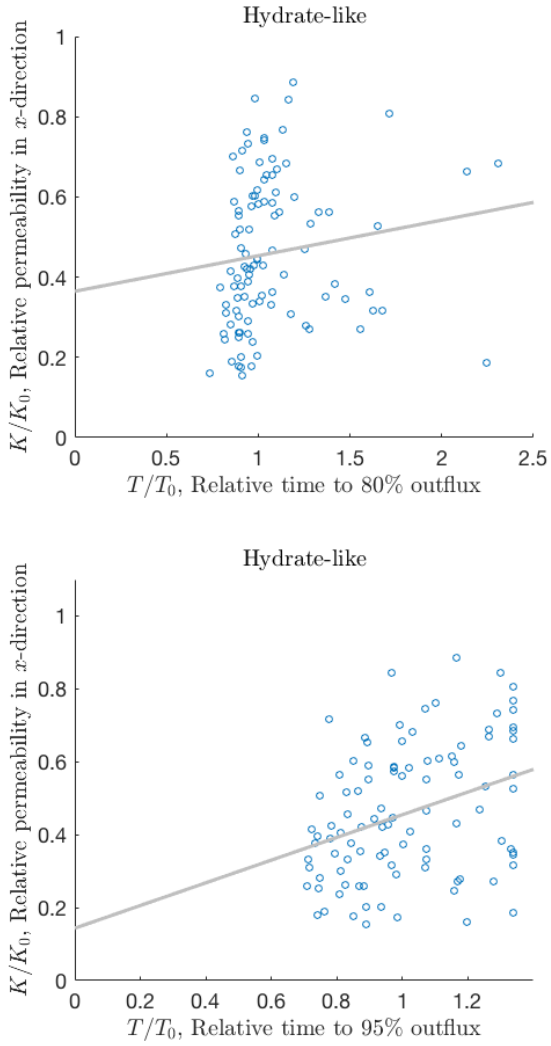

FIGURE 7.15: Relative change in K against the relative change in $T^{(\alpha)}$ due to hydrate-like obstructions. See Section 7.2.2 Top: $\alpha = 0.8$. Bottom: $\alpha = 0.95$.

7.3 Tortuosity distributions in many more geometries

The experiment presented in this section is a study on tortuosity changes in an REV. We present distributions of the relative change in tortuosity $\mathbf{T}$ as a function of obstruction volume. Tortuosity is a measure of fluid path lengths in a porous media, explained in Section 3.1.5.

For this experiment we use an REV from [35], shown in Figure 7.1b. The flow inlet is the left side of the domain, the outlet is the right side. The top and bottom of the domain impose no slip conditions.

We consider two types of obstructions, biofilm-like and hydrate-like. The obstructed geometries are generate with the phase separation model of Section 5. We use three values of obstruction volume $V_o = 0.05,\ 0.1,\ 0.15$.

For a given type of obstruction we generate $M = 100$ obstructed geometries. Next we analyze the results of the M independent simulations $i = 1, 2, \ldots, M$ of the geometries with obstructions. For each geometry $D_f^{(i)}$ we calculate the transport of a single species through the domain and derive the tortuosity, as explained in Section 3.6.

The results of this section show instances of both increasing average path lengths and decreasing average path lengths. We remind the reader that $\mathbf{T}_i/\mathbf{T}_0 > 1$ means the average hydraulic path lengths have increased for geometry i.

7.3.1 Biofilm-like obstructions

To create the biofilm-like obstructions with the CLPS model for this experiment we set the parameters as follows,

$$\epsilon = 0.2, \qquad \theta = -0.5, \qquad \delta = 0.1.$$

For illustration we show an example biofilm obstruction in D_f in Figure 7.16. We see two instances of throat clogging and many small "colonies".

Results for this experiment are shown in Figure 7.17. We see that for most geometries with obstructions $\mathbf{T}$ is greater than in the unobstructed geometry, and that with greater obstruction volume there is a greater increase in $\mathbf{T}$.

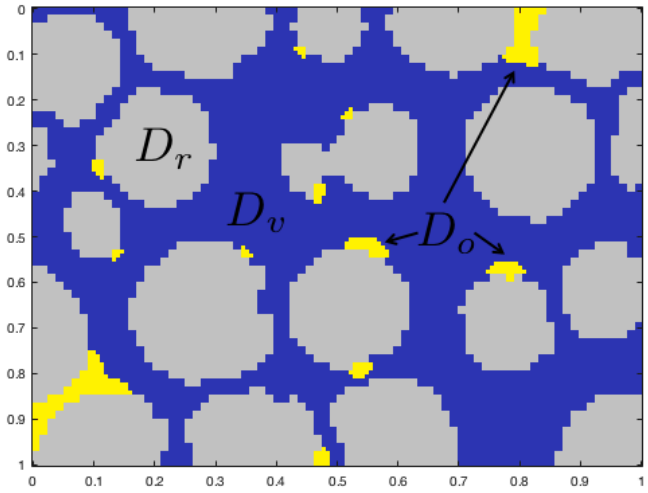

FIGURE 7.16: Biofilm-like obstruction with $V_o = 0.05$ for experiment in Section 7.3

7.3.2 Hydrate-like obstructions

To create the hydrate-like obstructions with the CLPS model for this experiment we set the parameters as follows,

$$\epsilon = 0.3, \qquad \theta = 0.5, \qquad \delta = 0.15.$$

For illustration we show an example hydrate obstruction in D_f in Figure 7.18. In this example we can see several hydrate-like "crystals" forming in the flow domain, as well as one small "crystal" attached to the solid matrix. This example is useful in showing that the CLPS model can capture the unlikely, but possibly occurring situation where the hydrate and solid matrix are adjacent.

Results for this experiment are shown in Figure 7.19. In this case, we see decreasing tortuosity $\mathbf{T}$. Because of the decrease in average path lengths we can see that while tortuosity is part of the bigger picture in understanding how porous media responds to obstruction formation it does not tell the whole story.

7.4 Breakthrough curves at multiple scales

In this section we compare breakthrough results at the pore scale with breakthrough results at the Darcy scale. For the results in this section we use the same

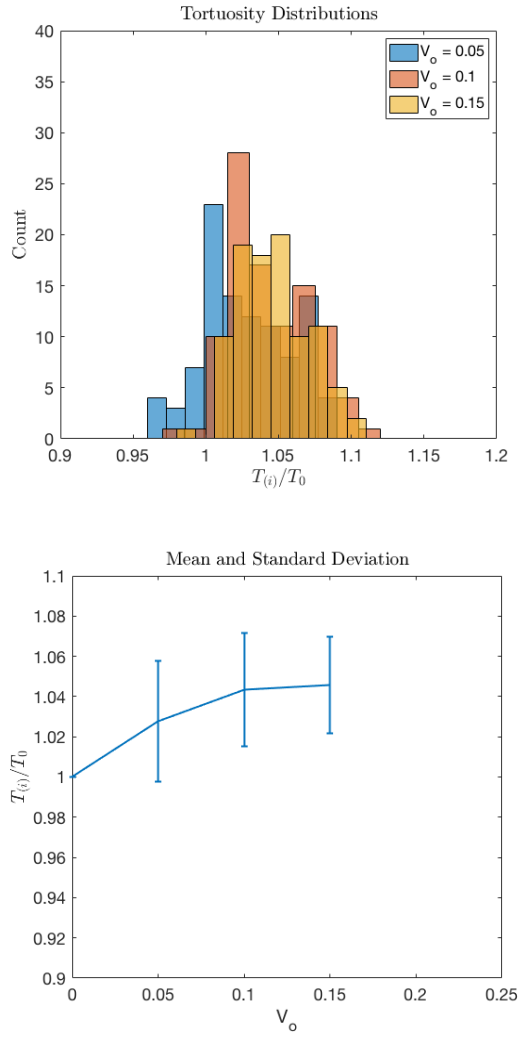

FIGURE 7.17: Relative change in tortuosity due to biofilm-like obstructions in a many pore geometry, see Section 7.3. Top: histogram of $(\mathbf{T}_{(i)}/\mathbf{T}_0)_i$ for 3 values of V_o. Bottom: mean and standard deviation of $(\mathbf{T}_{(i)}/\mathbf{T}_0)_i$ for 3 values of V_o.

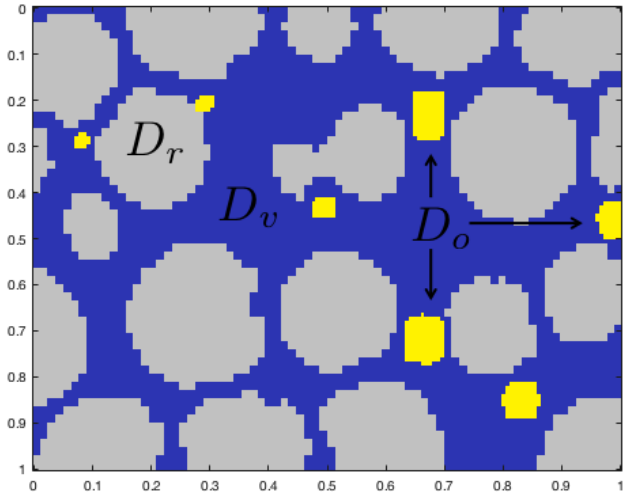

FIGURE 7.18: Hydrate-like obstruction with $V_o = 0.05$ for experiment in Section 7.3

experiments and computational results from Section 7.3. With this experiment we study the relationship between transport at multiple scales in obstructed porous media.

We report pore scale breakthrough with the quantity $T^{(0.95)}$, as defined in (7.2.1).

We model Darcy scale transport with (3.2.2). To calculate the upscaled velocity we use (3.3.7), Dupuit's relation modified to account for tortuosity. Because U is constant, the Darcy scale transport has analytical solutions. Let $D = (0, L_1) \times (0, L_2)$. We report the time T_f when quantity C has been transported across the domain,

$$T_f = \frac{L_1 \phi}{U_1}. \tag{7.4.1}$$

We present results for both pore coating and pore filling obstructions in Figure 7.20. We observe that in the case of pore filling obstructions the range of outcomes is larger than in the case of pore coating obstructions. We also see that for both types of obstructions, as V_o increases so does the Darcy scale breakthrough time, which is the behavior one would expect.

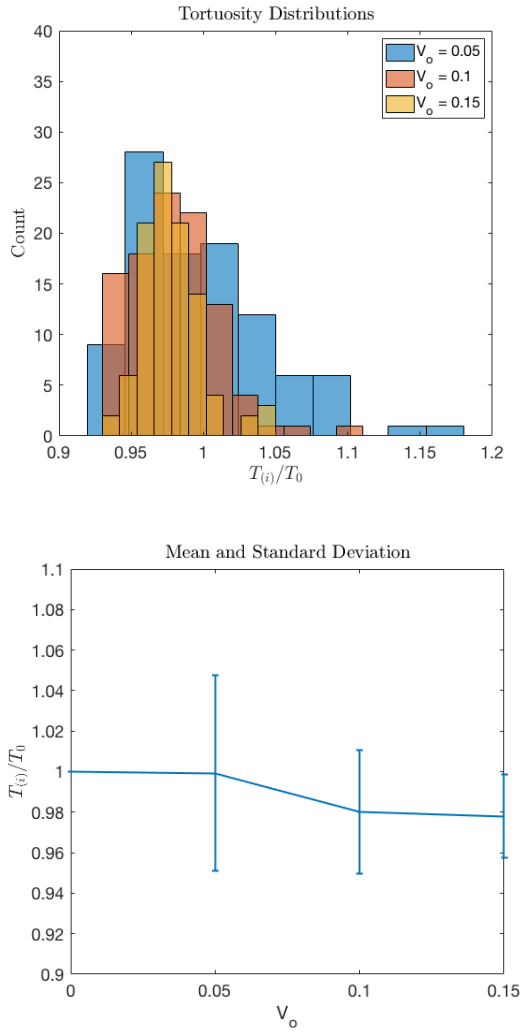

FIGURE 7.19: Relative change in tortuosity due to hydrate-like obstructions in a many pore geometry, see Section 7.3. Top: histogram of $(\mathbf{T}_{(i)}/\mathbf{T}_0)_i$ for 3 values of V_o. Bottom: mean and standard deviation of $(\mathbf{T}_{(i)}/\mathbf{T}_0)_i$ for 3 values of V_o.

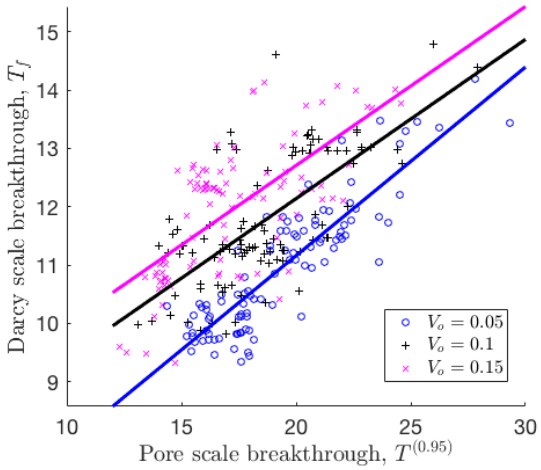

(a) Pore coating obstructions

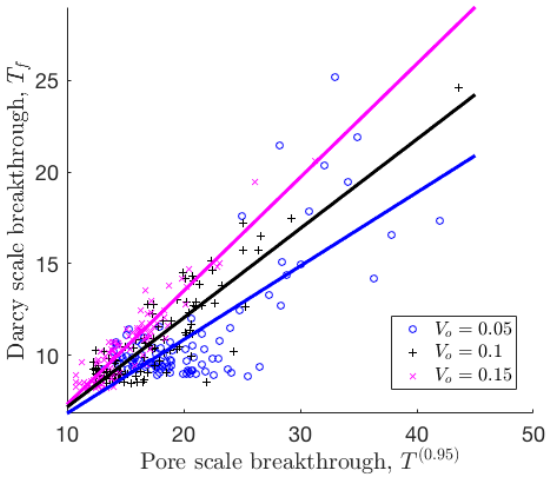

(b) Pore filling obstructions

FIGURE 7.20: Scatter plot of Darcy scale breakthrough time T_f vs pore scale breakthrough time $T^{(0.95)}$.

8 Summary

In this thesis we considered mathematical and computational models to study flow and transport phenomena in porous media. In particular, we studied how Darcy scale properties of the porous media change as the pore scale geometry changes due to the formation of obstructions. The pore scale obstructions central to our work were of pore coating and pore filling type specific to the applications involving biofilm and hydrate crystal growth. These are important for various applications, and we provided details motivating this work.

Our contributions are as follows. We proposed a new collection of methods for the generation of geometries with obstructions which allow one to avoid expensive and uncertain direct numerical simulations (DNS) of the physical processes. The first new method we present in this work is the Constrained Local Phase Separation (CLPS) model in Chapter 5. The CLPS model is an extension of the Allen-Cahn phase separation model where we have added constraints to make the model phase conserving, and added a spatial injection function so the phase separation can respond to the complex domain. The second new method we present in this work is the Lattice model in Chapter 6. The Lattice model is a Markov chain Monte Carlo method inpired by the Ising model.

We employed the two new models to complete numerical experiments, presented in Chapter 7. Both models have parameters we tune by hand so that the obstructions generated mimic the desired characteristics, either pore filling or pore coating. From the completed experiments we can infer how porous media properties are impacted by specific geometry changes. In particular, we confirm that the permeability is not solely a function of porosity, but rather is highly dependent on how the geometry is changing.

We wish to highlight some features of our experiments and models. First, we find that in general the two models produce upscaled results that are in agreement with one another. For example, in the single pore permeability experiments of Section 7.1 one can compare Figures 7.3 and 7.5 and see similar qualitative behavior in the mean

relative change in permeability due to biofilm-like obstructions.

Second, we point out that our models can capture important characteristics of obstruction formation. For pore coating obstructions, we see throat clogging in a many pore domain with the Lattic model in Figure 7.12, and with the CLPS model in Figure 7.16. For pore filling obstructions, we see that the obstructions mostly avoid the rock matrix, but as in seen in [10] under certain conditions hydrate are adjacent to the rock matrix. In Figure 7.18 we see a domain with pore filling obstructions generated by the CLPS method, but with some contact between obstruction and rock matrix from which we infer that our model can be tuned to match the behavior under such certain conditions.

8.1 Using our methods

In developing and using our CLPS and Lattice model we have learned much that we'd like to pass on to the interested reader. In particular, for both methods the choice of parameters is currently more "art" than "science." While we hope to address this in the future, here we describe various considerations of the parameters to achieve desired results.

The CLPS model. For the CLPS model the tuning parameters are ϵ, θ and δ. The coefficient ϵ controls the relative amplitude of the diffusion and sharpening injection function f. With larger ϵ there is more diffusion, which will result in fewer, but larger aggregations of phase parameter.

The coefficient θ controls the amplitude of the spatial injection function g_δ. With $\theta > 0$ the model produces pore filling obstructions. With $\theta < 0$ the model produces pore coating obstruction. With $\theta = 0$ the spatial injection function plays no role. One needs to be careful with the magnitude of θ; if the magnitude is too large then phase parameter ψ may end up outside of the expected range $[0, 1]$. One can compensate for this by decreasing ϵ, as the phase parameter will pushed back towards $[0, 1]$, but it comes at the cost of decreased diffusion.

Lastly, we note that δ should be adjusted to the scale of the pore so that obstruction formation is either discouraged for an appropriate distance from the rock matrix, or so that obstruction formation is encouraged near the rock matrix out to some distance.

With the CLPS model it is not practical to simulate colloidal obstructions. To create colloidal obstructions one needs ϵ to be small to prevent large obstructions from forming. But then the impact of diffusion is minimized, so the phase parameter doesn't change location much. The equilibrium phase solution in this case is more or less the random initial condition.

The Lattice model. For the Lattice model the tuning parameters are the weights ω assigned to interactions between nodes. A higher weight value for a given material adjacency means it's less likely for those materials to be adjacent. For example, if $w_{ro} = 1$ and $w_{rv} = 2$, then it's more likely that the material in adjacent nodes are rock matrix and obstruction, rather than rock matrix and void space.

In general, giving the weights higher magnitudes leads to finding states in the desired distribution in fewer steps. However, this comes at the cost of the method stagnating in a local energy minimum state. One of the advantages of MCMC methods is that with some probability the system energy will increase from one step to the next, which allows the method to find other local energy minima. Using Weights with high magnitudes decreases the probability of increasing the system energy from one step to the next.

Geometries generated by the Lattice model may have a single obstruction node surrounded by nodes of void space or rock matrix, or possibly a void space node surrounded by obstruction nodes. This behavior is expected from the model and is due to the inherent randomness of the model, however these spurious node materials may be physically unrealistic.

Coupling CLPS and Lattice models. To account for nodes with spurious material designations in results generated by the Lattice model we can couple the Lattice model with the CLPS model. One would first use the Lattice models, then apply the CLPS model to the result. The diffusion present in the CLPS model would smooth the

obstructions generated by the Lattice model.

This coupling could be used to optimize (in the sense of time) the process of generating the random obstructions. The Lattice model is faster to use than CLPS model by an order of magnitude. So one could use the Lattice model to first generate rough obstructed geometries, then use the CLPS model to smooth the obstructions.

Computational considerations. For an estimate of computational complexity, consider simulations on a many pore domain with $O(17,000)$ voxels. The simulations were run on a 2013 Macbook Air. The CLPS model generated obstructed geometries in around 5 minutes. The Lattice model generated obstructed geometries in around 45 seconds.

In terms of coding complexity, the CLPS method was more difficult to implement than the Lattic model, even with the simplification of using an IMEX method.

Other tools used. The CLPS and Lattice models were implemented in Matlab. This saves a tremendous amount of time in coding relative to, say, c++. For example, we can use the "backslash" operator \ to solve the saddle point system of the CLPS method with consideration of what iterative solver Matlab utilizes.

The other tool we made significant use of was HybGe-Flow3D [14]. HybGe-Flow3D was simple to use and very efficient in finding flow solutions on the obstructed geometries. Support for this tool was prompt. We contributed to this open source tool as we extended it to perform the specific experiments that we report on in Chapter 7.

HybGe-Flow3D also offers features that we have not yet taken advantage of. This includes the ability to simulate flow in the presence of permeable obstructions and varying viscosity.

8.2 Future work

We see many avenues for where to take this research, some of which have been touched on throughout the previous chapters. In particular, in Chapter 4 we discussed how this work could be used to emulate and expand on the physical experiments com-

pleted in [10]. Similarly, this work could be used in concert with the DNS method presented in [35].

A natural place for this work to extend to is three dimensions. In higher dimensions we expect to see smaller changes in the permeability due to pore scale obstructions, because the extra dimension adds another degree of freedom for the flow to move around.

We would also like to validate our model. For example, can we recreate results similar to the physical experiment and DNS in [35]?

Using the flow solver HybGe-Flow3D offers several possibilities as well. The two main things to explore here are using the Immersed Boundary Stokes Model for flow and varying viscosity. By using the IBSM we can make the obstructions permeable. This is particularly useful for studying biofilm and hydrate because those obstructions can be permeable.

One difficulty here is that it is not clear what the porosity of a porous media is in the presence of permeable obstructions. This becomes a problem in, e.g., upscaled transport, where porosity is coefficient.

Another way to improve our models would be to choose the parameters algorithmically rather than by hand. One way we see this working is to implement a machine learning algorithm for classifying images. The idea is to use synthetic geometries with specified parameter choices as a training set. Then, images from physical experiment would be classified by the algorithm. The set of parameters that the experimental images are classified as would be deemed the "best" set of parameters for that particular porous medium and obstruction formation. This process could be iterated and more training data added to improve the accuracy of the classification.

Work specific to the CLPS model includes studying the well-posedness of the model and consideration of other possible injection functions. The spatial injection function g was chosen because it would create the desired patterns in the obstruction formation. Perhaps another function could achieve the same or better functionality.

Bibliography

1. Samuel M. Allen and John W. Cahn. A microscopic theory for antiphase boundary motion and its application to antiphase domain coarsening. *Acta Metallurgica*, 27(6):1085–1095, June 1979.

2. Todd Arbogast and Heather L. Lehr. Homogenization of a Darcy–Stokes system modeling vuggy porous media. *Computational Geosciences*, 10(3):291–302, September 2006.

3. Kendall Atkinson and Weimin Han. *Theoretical Numerical Analysis: A Functional Analysis Framework*. Texts in Applied Mathematics. Springer-Verlag, New York, 3 edition, 2009.

4. Philippe Baveye and Albert Valocchi. An evaluation of mathematical models of the transport of biologically reacting solutes in saturated soils and aquifers. *Water Resources Research*, 25(6):1413–1421, 1989.

5. Deborah N. Huntzinger Beach and John E. McCray. Numerical Modeling of Unsaturated Flow in Wastewater Soil Absorption Systems. *Groundwater Monitoring & Remediation*, 23(2):64–72, 2003.

6. Jacob Bear. *Dynamics of fluids in porous media*. Dover, New York, 1972. OCLC: 760275111.

7. Jacob Bear and Alexander H.-D. Cheng. *Modeling Groundwater Flow and Contaminant Transport*. Springer, 2010.

8. Ray Boswell. Japan Completes First Offshore Methane Hydrate Production Test - Methane Successfully Produced From Deepwater Hydrate Layers. *Cent. Nat. Gas Oil*, page 412, 2013.

9. John W Cahn and John E Hilliard. Free Energy of a Nonuniform System. I. Interfacial Free Energy. *J. Chem. Phys.*, 28(2):258–267, 1958.

10. Xiongyu Chen and D. Nicolas Espinoza. Ostwald ripening changes the pore habit and spatial variability of clathrate hydrate. *Fuel*, 214:614–622, February 2018.

11. S. Chippada, C. N. Dawson, M. L. Martínez, and M. F. Wheeler. A projection method for constructing a mass conservative velocity field. *Computer Methods in Applied Mechanics and Engineering*, 157(1-2):1–10, 1998.

12. M. Ben Clennell. Tortuosity: a guide through the maze. *Geological Society, London, Special Publications*, 122(1):299–344, 1997.

13. Timothy Costa. *Hybrid Multiscale Methods with Applications to Semiconductors, Porous Media, and Materials Science*. PhD Thesis, Oregon State University, 2016.

14. Timothy Costa. *HybGe-Flow3D*. 2017.

15. Timothy B. Costa, Kenneth Kennedy, and Malgorzata Peszynska. Hybrid three-scale model for evolving pore-scale geometries. *Computational Geosciences*, 22(3):925–950, June 2018.

16. Clint Dawson. Conservative, shock-capturing transport methods with nonconservative velocity approximations. *Computational Geosciences*, 3(3):205–227, December 1999.

17. J. T. Dejong, K. Soga, Edward Kavazanjian, S. Burns, Leon van Paassen, A. Al Qabany, A. Aydilek, S. S. Bang, M. Burbank, L. F. Caslake, C. Y. Chen, X. Cheng, J. Chu, S. Ciurli, A. Esnault-Filet, S. Fauriel, N. Hamdan, T. Hata, Y. Inagaki, S. Jefferis, M. Kuo, L. Laloui, J. Larrahondo, D. a. C. Manning, B. Martinez, B. M. Montoya, D. C. Nelson, A. Palomino, P. Renforth, J. C. Santamarina, E. A. Seagren, B. Tanyu, M. Tsesarsky, and T. Weaver. Biogeochemical processes and geotechnical applications: Progress, opportunities and challenges. In *Bio- and Chemo- Mechanical Processes in Geotechnical Engineering - Geotechnique Symposium in Print 2013*, pages 143–157. ICE Publishing, 2013.

18. C. M. Elliott and A. M. Stuart. The Global Dynamics of Discrete Semilinear Parabolic Equations. *SIAM Journal on Numerical Analysis*, 30(6):1622–1663, 1993.

19. Howard C. Elman, David J. Silvester, and Andrew J. Wathen. *Finite Elements and Fast Iterative Solvers: With Applications in Incompressible Fluid Dynamics*. Oxford University Press, 2005.

20. Alexandre Ern and Jean-Luc Guermond. *Theory and Practice of Finite Elements*. Springer, 2004.

21. Ronald B. Guenther and John W. Lee. *Partial Differential Equations of Mathematical Physics and Integral Equations*. Dover Publications, 1996.

22. Duzi Huang and Shuanshi Fan. Thermal Conductivity of Methane Hydrate Formed from Sodium Dodecyl Sulfate Solution. *Journal of Chemical & Engineering Data*, 49(5):1479–1482, September 2004.

23. Morten Jakobsen, John A. Hudson, Tim A. Minshull, and Satish C. Singh. Elastic properties of hydrate-bearing sediments using effective medium theory. *Journal of Geophysical Research: Solid Earth*, 105(B1):561–577, 2000.

24. Anjani Kumar, Brij Maini, P.R. Bishnoi, Matthew Clarke, Olga Zatsepina, and Sanjay Srinivasan. Experimental determination of permeability in the presence of hydrates and its effect on the dissociation characteristics of gas hydrates in porous media. *Journal of Petroleum Science and Engineering*, 70(1):114–122, January 2010.

25. Randall LeVeque. *Finite Volumn Methods for Hyperbolic Problems*. Cambridge University Press, 2002.

26. Randall J. LeVeque. *Finite Difference Methods for Ordinary and Partial Differential Equations: Steady-State and Time-Dependent Problems*. Society for Industrial and Applied Mathematics, January 2007.

27. Peter C Lichtner, Carl I Steefel, Eric H Oelkers, and Mineralogical Society of America. *Reactive transport in porous media*. Washington, DC : Mineralogical Society of America, 1996.

28. Neal Noah Madras. *Lectures on Monte Carlo Methods*. American Mathematical Soc., 2002.

29. Akira Masui, Hironori Haneda, Yuiji Ogata, and Kazuo Aoki. Effects of Methane Hydrate Formation On Shear Strength of Synthetic Methane Hydrate Sediments. International Society of Offshore and Polar Engineers, January 2005.

30. F Patricia Medina and Malgorzata Peszynska. Hybrid modeling and analysis of multicomponent adsorption with applications to coalbed methane. In *Porous Media: Theory, Properties, and Applications*, pages 1–52. Nova Science Publishers, 2016. Editor: Doris Wolfe.

31. Nicholas Metropolis, Arianna W. Rosenbluth, Marshall N. Rosenbluth, Augusta H. Teller, and Edward Teller. Equation of State Calculations by Fast Computing Machines. *The Journal of Chemical Physics*, 21(6):1087–1092, June 1953.

32. F. J. Molz, M. A. Widdowson, and L. D. Benefield. Simulation of Microbial Growth Dynamics Coupled to Nutrient and Oxygen Transport in Porous Media. *Water Resources Research*, 22(8):1207–1216, 1986.

33. T. Okubo and J. Matsumoto. Effect of infiltration rate on biological clogging and water quality changes during artificial recharge. *Water Resources Research*, 15(6):1536–1542, 1979.

34. Suhas V. Patankar. *Numerical Heat Transfer and Fluid Flow*. Hemisphere Publishing Corporation, 1980. Google-Books-ID: N2MVAQAAIAAJ.

35. M. Peszynska, A. Trykozko, G. Iltis, S. Schlueter, and D. Wildenschild. Biofilm growth in porous media: experiments, computational modeling at the porescale, and upscaling. *Advances in Water Resources*, 95:288–301, 2016.

36. Malgorzata Peszynska and Anna Trykozko. Convergence and Stability in Upscaling of Flow with Inertia from Porescale to Mesoscale. *International Journal for Multiscale Computational Engineering*, 9(2):215–229, 2011.

37. Malgorzata Peszynska, Anna Trykozko, and K. Augustson. Computational upscaling of inertia effects from porescale to mesoscale. In G Allen, J Nabryzski, E Seidel, D van Albada, J Dongarra, and P Sloot, editors, *ICCS*. Springer-Verlag, 2009.

38. Małgorzata Peszyńska, Eleanor W. Jenkins, and Mary F. Wheeler. Boundary conditions for fully implicit two-phase flow models. In Xiaobing Feng and Tim P. Schulze, editors, *Contemporary Mathematics*, volume 306, pages 85–106. American Mathematical Society, Providence, Rhode Island, 2002.

39. Masa Prodanovic, Maria Esteva, Matthew Hanlon, Gaurav Nanda, and Prateek Agarwal. Digital Rocks Portal: a repository for porous media images, 2015.

40. R. Tyrrell Rockafellar. Lagrange Multipliers and Optimality. *SIAM Review*, 35(2):183–238, 1993.

41. Jacob Rubinstein and Peter Sternberg. Nonlocal reaction—diffusion equations and nucleation. *IMA Journal of Applied Mathematics*, 48(3):249–264, January 1992.

42. Carolyn D. Ruppel and John D. Kessler. The interaction of climate change and methane hydrates. *Reviews of Geophysics*, 55(1):126–168, March 2017.

43. Thomas Russell and Mary Wheeler. Finite Element and Finite Difference Methods for Continuous Flows in Porous Media. *Frontiers in Applied Mathematics*, 1, January 1983.

44. J. Shen. Efficient Spectral-Galerkin Method I. Direct Solvers of Second- and Fourth-Order Equations Using Legendre Polynomials. *SIAM Journal on Scientific Computing*, 15(6):1489–1505, November 1994.

45. Jie Shen and Xiaofeng Yang. Numerical approximations of Allen-Cahn and Cahn-Hilliard equations. *Discrete and Continuous Dynamical Systems*, 28(4):1669–1691, June 2010.

46. Ronald W Shonkwiler and Franklin Mendivil. *Explorations in Monte Carlo Methods*. Springer Science & Business Media, 2009.

47. R. Showalter. *Monotone Operators in Banach Space and Nonlinear Partial Differential Equations*, volume 49 of *Mathematical Surveys and Monographs*. American Mathematical Society, Providence, Rhode Island, February 2013.

48. Ralph E. Showalter. *Hilbert Space Methods in Partial Differential Equations*. Dover Publications, 2010.

49. Sahar Soleimani, Paul J. Van Geel, O. Burkan Isgor, and Mohamed B. Mostafa. Modeling of biological clogging in unsaturated porous media. *Journal of Contaminant Hydrology*, 106(1):39–50, April 2009.

50. S Solomon, D Qin, M Manning, Z Chen, M Marquis, K B Averyt, M Tignor, and H L Miller. IPCC (2007). Climate Change 2007: The Physical Science Basis. Technical report, Cambridge University Press, United Kingdom, 2007.

51. Erik Spangenberg. Modeling of the influence of gas hydrate content on the electrical properties of porous sediments. *Journal of Geophysical Research: Solid Earth*, 106(B4):6535–6548, 2001.

52. Luc Tartar. Incompressible fluid flow in a prous medium - convergence of the homogenization process. *Nonhomogeneous Media and Vibration Theory*, 127, 1980.

53. Joe Umhoefer. Interpolation Schemes for Two Dimensional Flow with Applications. Master's thesis, Oregon State University, 2016.

54. TL Van Noorden and IS Pop. A Stefan problem modelling crystal dissolution and precipitation. *IMA journal of applied mathematics*, 73(2):393–411, 2008.

55. H. K. Versteeg and W. Malalasekera. *An introduction to computational fluid dynamics: the finite volume method*. Pearson Education Ltd, Harlow, England ; New York, 2nd ed edition, 2007. OCLC: ocm76821177.

56. Lunxiang Zhang, Lei Yang, Yu Liu, and Yongchen Song. Microstructural characteristics of natural gas hydrates hosted in various sand sediments. *Physical chemistry chemical physics : PCCP*, 17, August 2015.